The dust mass in Cassiopeia A from a spatially resolved *Herschel* analysis

I. De Looze,[1]★ M. J. Barlow,[1] B. M. Swinyard,[1,2]† J. Rho,[3] H. L. Gomez,[4]
M. Matsuura[4] and R. Wesson[1]

[1]*Department of Physics and Astronomy, University College London, Gower Street, London WC1E 6BT, UK*

[2]*RAL Space, Rutherford Appleton Laboratory, Chilton, Didcot, Oxfordshire OX11 0QX, UK*

[3]*SETI Institute, 189 Bernardo Ave, Mountain View, CA 94043, USA*

[4]*School of Physics and Astronomy, Cardiff University, The Parade, Cardiff CF24 3AA, UK*

ABSTRACT

Theoretical models predict that core-collapse supernovae (CCSNe) can be efficient dust producers (0.1–1.0 $M_\odot$), potentially accounting for most of the dust production in the early Universe. Observational evidence for this dust production efficiency is however currently limited to only a few CCSN remnants (e.g. SN 1987A, Crab nebula). In this paper, we revisit the dust mass produced in Cassiopeia A (Cas A), a ~330-yr old O-rich Galactic supernova remnant (SNR) embedded in a dense interstellar foreground and background. We present the first spatially resolved analysis of Cas A based on *Spitzer* and *Herschel* infrared and submillimetre data at a common resolution of ~0.6 arcmin for this 5 arcmin diameter remnant following a careful removal of contaminating line emission and synchrotron radiation. We fit the dust continuum from 17 to 500 μm with a four-component interstellar medium and supernova (SN) dust model. We find a concentration of cold dust in the unshocked ejecta of Cas A and derive a mass of 0.3–0.5 $M_\odot$ of silicate grains freshly produced in the SNR, with a lower limit of ≥0.1–0.2 $M_\odot$. For a mixture of 50 per cent of silicate-type grains and 50 per cent of carbonaceous grains, we derive a total SN dust mass between 0.4 and 0.6 $M_\odot$. These dust mass estimates are higher than from most previous studies of Cas A and support the scenario of SN-dominated dust production at high redshifts. We furthermore derive an interstellar extinction map for the field around Cas A which towards Cas A gives average values of A_V = 6–8 mag, up to a maximum of A_V = 15 mag.

Key words: supernovae: individual: Cassiopeia A – dust, extinction – ISM: supernova remnants – infrared: ISM.

1 INTRODUCTION

The large reservoirs of dust observed in some high-redshift galaxies (e.g. Bertoldi et al. 2003; Priddey et al. 2003; Rowlands et al. 2014; Watson et al. 2015) have been hypothesized to originate from dust produced by supernovae (SNe) from massive stars. Some theoretical studies (e.g. Kozasa, Hasegawa & Nomoto 1991; Todini & Ferrara 2001) have supported a high efficiency of dust production (0.1–1.0 $M_\odot$) in core-collapse supernovae (CCSNe) which would suffice to account for the dust mass budget observed in dusty high-redshift sources (Morgan & Edmunds 2003; Dwek, Galliano & Jones 2007). However, the dust reservoirs (≤10^{-2} $M_\odot$) that were detected at mid-IR wavelengths during the first 1000 d in a number of CCSNe remained several orders of magnitude below these

theoretical predictions (Sugerman et al. 2006; Meikle et al. 2007; Kotak et al. 2009; Fabbri et al. 2011). With the recent advent of far-infrared (FIR) and submillimetre (submm) observing facilities (e.g. *Herschel* and ALMA), the ability to also detect the emission from colder dust in CCSN remnants opened up and resulted in the detection of dust masses of the order of 0.1–1.0 $M_\odot$ (Barlow et al. 2010; Matsuura et al. 2011; Gomez et al. 2012; Indebetouw et al. 2014; Matsuura et al. 2015) in some nearby supernova remnants (SNRs; SN 1987A, Crab nebula, Cassiopeia A). Some SNRs show evidence for dust formation in the SN ejecta once the ejecta material has sufficiently cooled after expansion to allow grain growth to take place (e.g. Andrews et al. 2016). Recent work by Gall et al. (2014), Wesson et al. (2015) and Bevan & Barlow (2016) suggests that the dust mass in CCSN ejecta grows in time possibly due to accretion of material on to and coagulation of grain species. Of particular interest for studies of the mechanisms responsible for dust formation is the Galactic SNR Cassiopeia A (hereafter, Cas A), which shows evidence for dust in the shocked outer SN ejecta as well as in the

★ E-mail: ideloose@star.ucl.ac.uk
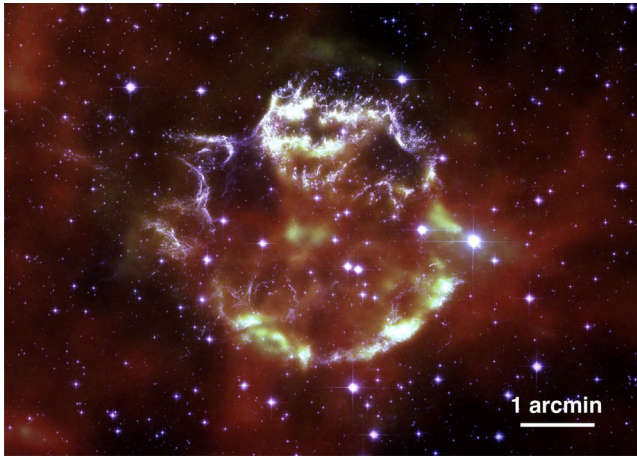
† Deceased 2015 May 22.

Figure 1. Cas A as viewed by the *Herschel* PACS instrument at 70 µm (red to green colours) and the *Hubble Space Telescope* in the *F625W*, *F775W* and *F850LP* bands (white to purple colours).

inner, unshocked regions of the remnant (Rho et al. 2008; Barlow et al. 2010; Arendt et al. 2014).

In this paper, we study *Spitzer* and *Herschel* infrared and submm maps of the SNR Cas A on spatially resolved scales of 0.6 pc to constrain the mass and position of formed dust species. Cas A (Fig. 1) is the remnant of an SN explosion of a massive progenitor about 330-yr ago (Fesen et al. 2006). Based on spectra of optical light echoes, Cas A was, more specifically, characterized as a hydrogen-poor type IIb CCSN (Krause et al. 2008). Due to the relatively young age of the remnant, the mass of swept-up material is small compared to the mass in the SN ejecta, which makes it still possible to separate SN dust from any swept-up circumstellar material. Early *IRAS/ISO* studies detected 10^{-4}–10^{-2} M$_\odot$ of warm ($T_d \sim$ 50–100 K) dust (e.g. Braun 1987; Dwek et al. 1987; Arendt 1989; Arendt, Dwek & Moseley 1999; Douvion, Lagage & Pantin 2001). Based on SCUBA observations at submm wavelengths, the presence of a cold ($T_d \sim$ 15–20 K) dust reservoir of 2–4 M$_\odot$ was inferred from the level of excess emission after subtraction of the non-thermal synchrotron emission component (Dunne et al. 2003). This large dust mass was, however, questioned and much of the excess submm emission was attributed to foreground interstellar dust (Krause et al. 2004). Dunne et al. (2009) interpreted the high level of polarization at 850 µm as due to the alignment of 1 M$_\odot$ of dust with the magnetic field in the SNR. Several analyses of 3.6–160 µm *Spitzer* data of Cas A found warm dust masses (3 × 10^{-3} M$_\odot$, Hines et al. 2004; 0.02–0.054 M$_\odot$, Rho et al. 2008; ∼ 0.04 M$_\odot$, Arendt et al. 2014) significantly lower compared to the submm-derived cold dust masses. By including the *Spitzer* Infrared Spectrograph (IRS) spectra in the dust spectral energy distribution (SED) modelling, Rho et al. (2008) and Arendt et al. (2014) showed that the composition of warm dust grains in Cas A could be studied in more detail. While the spectral characteristics of most of the dust in the bright ejecta knots and X-ray emitting shocked ejecta (associated with bright [Ar II] and [Ar III] line features) were found to be consistent with a magnesium silicate composition (with varying relative abundance ratios of Mg and Si), a smooth spectral component associated with [Ne II] emitting regions does not show any silicate features and was best reproduced by a Al$_2$O$_3$ (or carbonaceous) dust composition. The largest dust mass component was associated with an inner cold dust reservoir $\lesssim$0.1 M$_\odot$ with unidentified dust composition (Arendt et al. 2014). Sibthorpe et al. (2010) inferred a

dust mass of 0.06 M$_\odot$, with an average $T_d \sim$ 33 K, from *AKARI* and *BLAST* observations covering the 50–500 µm wavelength range, but their large beam size (1.3, 1.6, 1.9 arcmin at 250, 350 and 500 µm, respectively) hampered a clear separation of the interstellar and SN dust material. The higher angular resolution of *Herschel* (18.2, 24.9 and 36.3 arcsec at 250, 350 and 500 µm, respectively) enabled Barlow et al. (2010) to carry out a global fit to the interstellar and SN FIR dust emission. They derived an SN dust mass of 0.075 M$_\odot$, emitting at $T \sim$ 35 K, but were unable to determine whether any cooler dust was present in Cas A due to the difficulty to distinguish between interstellar medium (ISM) and SN dust emission at longer wavelengths (160–350 µm). The above results based on *Spitzer*, *BLAST* and *Herschel* data were consistent with the dust evolution models of Nozawa et al. (2010) who predicted 0.08 M$_\odot$ of new grain material in Cas A at a temperature of ∼40 K, of which 0.072 M$_\odot$ was predicted to reside in the inner remnant regions unaffected by the reverse shock.

In this paper, we combine *Spitzer*, *Herschel*, *Wide-field Infrared Survey Explorer* (*WISE*) and *Planck* photometric data from mid-infrared (MIR) to millimetre (mm) wavelengths and *Spitzer* and *Herschel* spectroscopic observations. We make a detailed study of the SN dust emission on spatially resolved scales, which allows us to more accurately separate the intrinsic SN dust emission from the non-thermal emission component and from the continuum emission by cold interstellar dust material. In Section 2, we present an overview of the observational data sets used for this analysis. Section 3 outlines the modelling technique for the various emission components (synchrotron radiation, ISM and SN dust emission). In Section 4, the multiwavelength SED is modelled on resolved scales in order to derive the distribution of temperatures and masses of newly formed dust grains in Cas A. Section 5 presents the SN dust masses and their uncertainties resulting from the SED modelling and discusses them in light of previous results. Our main conclusions are presented in Section 6.

In the appendix, we provide an overview of various methods used for the analysis presented in this paper. Appendix A compares the different *Planck* measurements for Cas A. Appendix B explains how we modelled the contribution of line emission to the different broad-band images. Appendix C discusses the photodissociation region (PDR) modelling technique that was used to constrain the interstellar radiation field (ISRF) along the sightline of Cas A. In Appendix D, we present the results of a global SED fitting analysis. Appendix E verifies the applicability of our models by directly comparing the models to observations (E1) and discusses the effect of small variations in the ISRF on the SN dust masses (E2). In Appendix F, we apply the model results to predict the relative contribution of line emission, synchrotron radiation, ISM and SN dust emission at IR–submm wavelengths (F1), to present a model image at 850 µm (F2), to estimate the interstellar and SN visual extinction (F3).

2 OBSERVATIONAL DATA

2.1 *Herschel*

Herschel (Pilbratt et al. 2010) observations of Cas A were obtained using Guaranteed Time (GT) contributed by the Spectral and Photometric Imaging Receiver (SPIRE) Consortium Specialist Astronomy Group 6 and the German Photodetector Array Camera and Spectrometer (PACS) consortium, as part of the MESS GT programme (PI: M. Groenewegen, Groenewegen et al. 2011). Table 1 gives an overview of the different *Herschel* data sets, observation

Table 1. Overview of the observation identification numbers (ObsIDs), observing dates, central coordinate positions and total observing times for the *Herschel* PACS and SPIRE photometric, and PACS IFU and SPIRE FTS spectroscopic observations of Cas A.

Object	ObsID	Date (yyyy-mm-dd)	RA (J2000) (^{hms})	Dec. (J2000) ($^{\circ\,\prime\,\prime\prime}$)	Obs time (s)
			PACS photometry		
Cas A	1342188204	2009-12-17	23:23:22.72	58:48:53.38	1889
Cas A	1342188205	2009-12-17	23:23:23.11	58:48:53.01	1889
Cas A	1342188206	2009-12-17	23:23:19.01	58:48:51.25	1889
Cas A	1342188207	2009-12-17	23:23:20.23	58:48:56.86	1889
			SPIRE photometry		
Cas A	1342183681	2009-09-12	23:23:19.48	58:49:23.66	5005
Cas A	1342188182	2009-12-17	23:23:21.94	58:49:59.49	5010
			PACS IFU spectroscopy		
Cas A–SP1	1342212249	2011-01-01	23:23:28.61	58:48:59.17	2267
Cas A–SP1	1342212250	2011-01-01	23:23:28.20	58:49:05.10	1139
Cas A–SP2	1342212253	2011-01-01	23:23:24.94	58:51:26.98	2267
Cas A–SP2	1342212254	2011-01-01	23:23:24.50	58:51:33.31	1139
Cas A–SP3	1342212257	2011-01-01	23:23:12.76	58:49:12.26	2267
Cas A–SP3	1342212258	2011-01-01	23:23:13.19	58:49:18.37	1139
Cas A–SP4	1342212245	2011-01-01	23:23:32.82	58:47:48.39	2267
Cas A–SP4	1342212246	2011-01-01	23:23:32.41	58:47:54.44	1139
Cas A–SP5	1342212251	2011-01-01	23:23:27.40	58:47:23.04	2267
Cas A–SP5	1342212252	2011-01-01	23:23:26.99	58:47:28.89	1139
Cas A–SP6	1342212243	2011-01-01	23:23:40.49	58:48:52.93	2267
Cas A–SP6	1342212244	2011-01-01	23:23:39.61	58:49:05.82	1139
Cas A–SP7	1342212247	2011-01-01	23:23:30.45	58:50:10.21	2267
Cas A–SP7	1342212248	2011-01-01	23:23:30.03	58:50:16.42	1139
Cas A–SP8	1342212255	2011-01-01	23:23:16.84	58:47:41.01	2267
Cas A–SP8	1342212256	2011-01-01	23:23:16.43	58:47:46.89	1139
Cas A–SP9	1342212259	2011-01-01	23:23:12.87	58:48:15.45	2267
Cas A–SP9	1342212260	2011-01-01	23:23:12.46	58:48:21.36	1139
			SPIRE FTS spectroscopy		
Cas A-centre	1342202265	2010-08-08	23:23:29	58:48:54	3476
Cas A-north	1342204034	2010-08-23	23:23:25	58:50:55	3476
Cas A-north-west	1342204033	2010-08-23	23:23:14	58:49:08	3476

identification numbers (ObsIDs), observing dates and integration times for the various *Herschel* instruments.

2.1.1 PACS photometry

PACS (Poglitsch et al. 2010) observed Cas A on 2009 December 17 and 2011 January 1, respectively. The PACS photometry data were obtained in parallel scan-map mode with two orthogonal scans of length 22 arcmin observed at the nominal scan speed of 20 arcsec s^{-1} in the blue+red and green+red filters. The total on-source integration in the blue (70 µm) and green (100 µm) filters was 2376 s, while the integration time in the red filter (160 µm) was 4752 s. The full width at half-maximum (FWHM) of the PACS beam corresponded to 5.6, 6.8 and 11.4 arcsec at 70, 100 and 160 µm, respectively (see PACS Observers' manual).

The PACS photometry data have been reduced with the latest HIPE v14.0.0 (Ott 2010) using the standard script which allows us to combine the scan and cross scans for a single field into one map. The script takes the level 1 data from the *Herschel* Science Archive, masks glitches, subtracts the baselines for separate scan legs, applies a drift correction and finally merges all scan and cross scan pairs to a final output map with default pixel sizes of 1.6 arcsec for the blue and green filters, and 3.2 arcsec for the red filter.

To correct for the shape of the spectrum, we apply colour corrections to the PACS maps (see the PACS calibration document

PICC-ME-TN-038). With a dominant contribution of warm ($T_d \sim$ 80 K) SN dust emission at PACS 70 µm (see Table 2), we apply a colour correction factor of 0.989. The PACS 160 µm emission is shown later to be dominated by emission from ISM dust irradiated by a radiation field $G \sim 0.6\,G_0$.[1] The colour correction for a blackbody with temperature $T = 17.6$ K is 0.967 at 160 µm. For the PACS 100 µm band, we find an equal contribution by dust emission from ISM and SN dust. The colour correction factor for the PACS 100 µm image is, therefore, calculated as the average (1.038) of the colour correction factors for blackbodies with temperatures of $T = 17.6$ K (1.069) and $T = 100$ K (1.007). The latter correction factors, and any factors mentioned in the remainder of this paper are multiplicative factors. The PACS maps are assumed to have a calibration uncertainty of 5 per cent (Balog et al. 2014).

2.1.2 PACS IFU spectroscopy

PACS spectroscopy data in PACS integral field unit (IFU) mode (FoV ∼ 47 arcsec) were obtained at nine different positions in Cas A,

---

[1] G corresponds to the average far-ultraviolet interstellar radiation normalized to the units of the Habing (1968) field, i.e. $G_0 = 1.6 \times 10^{-3}$ erg s^{-1} cm^{-2} (Tielens 2005). A normalization to the Draine (1978) field (indicated as χ_0) is frequently used and is related to the Habing (1968) field as $G_0 = 1.7\,\chi_0$.

Table 2. Overview of the aperture photometry results for Cas A in the IRAC 8 μm, *WISE* 12 and 22 μm, IRS 17 and 32 μm continuum, MIPS 24 μm, PACS 70, 100 and 160 μm, SPIRE 250, 350 and 500 μm and SCUBA 850 μm wavebands. Flux densities, F_ν, in units of Jy have been measured within an aperture with radius $R = 165$ arcsec centred on the position (RA, Dec.) = $(350°86311, 58°813292)$. The second column lists the total flux measured within this aperture, while the third and fourth column list the flux attributed to line and synchrotron emission, respectively. Columns 5 to 10 list the ISM and SN dust emission in every waveband for an ISM dust model with ISRF scaling factors $G = 0.3\ G_0$, $0.6\ G_0$ and $1.0\ G_0$, respectively, based on the best-fitting four-component SED model (one interstellar and three SN dust components). The values in parentheses represent the contributions of the different emission components relative to the total flux.

| Waveband	Total F_ν (Jy)	Line F_ν (Jy)	Synchrotron F_ν (Jy)	ISM dust ($G = 0.3\ G_0$)	SN dust ($G = 0.3\ G_0$)	ISM dust ($G = 0.6\ G_0$)	SN dust ($G = 0.6\ G_0$)	ISM dust ($G = 1.0\ G_0$)	SN dust ($G = 1.0\ G_0$)
IRAC 8 μm	11.3 ± 1.1	4.7 ± 0.5 [41.6 per cent]	1.6 ± 0.6 [14.2 per cent]	3.8 ± 0.4 [33.6 per cent]	0.2 ± 0.0 [1.8 per cent]	6.5 ± 0.4 [57.5 per cent]	**0.2 ± 0.0** **[1.8 per cent]**	9.1 ± 0.4 [80.5 per cent]	0.1 ± 0.0 [0.9 per cent]
WISE 12 μm	20.0 ± 0.8	3.4 ± 0.4 [17.0 per cent]	2.1 ± 0.7 [10.5 per cent]	2.4 ± 0.2 [12.0 per cent]	3.5 ± 0.3 [17.5 per cent]	4.0 ± 0.3 [20.0 per cent]	**3.4 ± 0.3** **[17.0 per cent]**	5.7 ± 0.3 [28.5 per cent]	2.9 ± 0.3 [14.5 per cent]
IRS 17	68.6 ± 8.0	–	2.4 ± 0.9 [3.5 per cent]	1.5 ± 0.1 [2.2 per cent]	63.5 ± 5.4 [92.6 per cent]	2.6 ± 0.2 [3.8 per cent]	**63.3 ± 6.0** **[92.3 per cent]**	3.6 ± 0.2 [5.2 per cent]	60.1 ± 6.0 [87.6 per cent]
WISE 22	208.1 ± 11.6	2.8 ± 0.3 [1.3 per cent]	3.0 ± 1.1 [1.4 per cent]	2.0 ± 0.2 [1.0 per cent]	204.1 ± 17.6 [98.1 per cent]	3.4 ± 0.2 [1.6 per cent]	**202.0 ± 19.3** **[97.1 per cent]**	4.8 ± 0.2 [2.3 per cent]	202.5 ± 20.8 [97.3 per cent]
MIPS 24	205.6 ± 6.3	45.5 ± 5.5 [22.1 per cent]	3.1 ± 1.1 [1.5 per cent]	2.2 ± 0.2 [1.1 per cent]	155.2 ± 13.6 [75.5 per cent]	3.8 ± 0.2 [1.8 per cent]	**153.4 ± 15.0** **[74.6 per cent]**	5.3 ± 0.2 [2.6 per cent]	151.6 ± 16.7 [73.7 per cent]
IRS 32	179.2 ± 21.1	–	3.6 ± 1.2 [2.0 per cent]	2.9 ± 0.3 [1.6 per cent]	174.2 ± 15.7 [97.2 per cent]	5.0 ± 0.3 [2.8 per cent]	**168.5 ± 17.3** **[94.0 per cent]**	7.0 ± 0.3 [3.9 per cent]	166.2 ± 21.3 [92.7 per cent]
PACS 70	178.8 ± 10.7	–	6.5 ± 2.0 [3.6 per cent]	8.9 ± 0.9 [5.0 per cent]	160.9 ± 16.6 [90.0 per cent]	21.8 ± 1.4 [12.2 per cent]	**149.5 ± 20.1** **[83.6 per cent]**	40.5 ± 1.9 [22.7 per cent]	130.4 ± 26.3 [72.9 per cent]
PACS 100	233.4 ± 15.3	16.0 [6.9 per cent]	8.1 ± 2.5 [3.5 per cent]	36.0 ± 3.6 [15.4 per cent]	173.4 ± 19.9 [74.3 per cent]	80.2 ± 5.3 [34.4 per cent]	**125.8 ± 19.9** **[53.9 per cent]**	130.7 ± 6.2 [56.0 per cent]	73.5 ± 17.6 [31.5 per cent]
PACS 160	236.2 ± 19.2	–	11.0 ± 3.3 [4.7 per cent]	99.9 ± 9.9 [42.3 per cent]	132.4 ± 15.9 [56.1 per cent]	165.9 ± 10.9 [70.2 per cent]	**69.9 ± 12.0** **[29.6 per cent]**	219.6 ± 10.4 [93.0 per cent]	25.2 ± 6.9 [10.7 per cent]
SPIRE 250	183.2 ± 10.0	–	14.5 ± 4.2 [7.9 per cent]	102.2 ± 10.1 [55.8 per cent]	61.5 ± 7.5 [33.6 per cent]	139.9 ± 9.2 [76.4 per cent]	**27.3 ± 4.8** **[14.9 per cent]**	162.8 ± 7.7 [89.0 per cent]	7.5 ± 2.1 [4.1 per cent]
SPIRE 350	111.9 ± 5.4	–	18.2 ± 5.0 [16.3 per cent]	69.6 ± 6.9 [62.2 per cent]	26.6 ± 3.3 [23.8 per cent]	86.8 ± 5.7 [77.6 per cent]	**10.9 ± 1.9** **[9.7 per cent]**	94.9 ± 4.5 [84.8 per cent]	2.6 ± 0.8 [2.3 per cent]
SPIRE 500	59.2 ± 2.2	–	23.5 ± 2.3 [39.7 per cent]	31.1 ± 3.1 [52.5 per cent]	6.9 ± 0.8 [11.7 per cent]	35.1 ± 2.3 [59.3 per cent]	**2.6 ± 0.5** **[4.4 per cent]**	36.0 ± 1.7 [60.8 per cent]	0.5 ± 0.2 [0.8 per cent]
SCUBA 850	50.8 ± 5.6	–	32.3 ± 8.1 [63.6 per cent]	8.1 ± 0.8 [15.9 per cent]	1.1 ± 0.1 [2.2 per cent]	8.6 ± 5.7 [16.9 per cent]	**0.4 ± 0.1** **[0.8 per cent]**	8.5 ± 0.4 [16.7 per cent]	0.1 ± 0.0 [0.2 per cent]
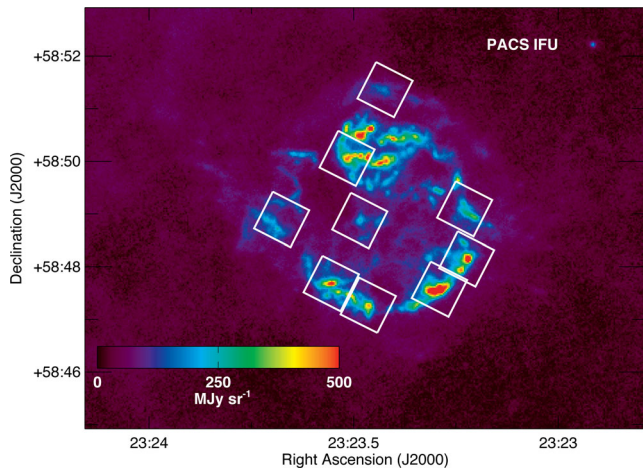
Figure 2. PACS 70 μm image of Cas A, overlaid with the on-source regions targeted with the PACS IFU spectrometer in the chopping mode. The off-source chopped positions were offset by 6 arcmin at a PA of ∼240 deg.

mainly targeting the shocked and the central regions of the remnant (see Fig. 2). Each position was observed in the wavelength ranges 51–72 μm and 102–146 μm (Range Mode SED B2A + Short R1) and in the ranges 70–105 μm and 140–220 μm (Range Mode SED B2B + Long R1). The PACS spectra were reduced to level 2 using the standard PACS chopped large-range scan and SED pipeline in HIPE v14.0.0 using the PACS_CAL_32_0 calibration file. The PACS IFU line measurements are assumed to have a calibration uncertainty of 13 per cent and 16 per cent shortwards and longwards of 150 μm, respectively, based on a combination of the absolute calibration uncertainty of 12 per cent and the relative uncertainty due to spaxel variations of 5 per cent (≤150 μm) and 10 per cent (>150μm).

2.1.3 SPIRE photometry

SPIRE (Griffin et al. 2010) observed Cas A on 2010 August 8 and 23, and on 2009 September 12 and December 17, respectively. The SPIRE observations consisted of two orthogonal scans observed at the nominal scan speed of 20 arcsec s^{-1} simultaneously at each wavelength (250, 350 and 500 μm) covering a 32 arcmin × 32 arcmin region centred on Cas A with an integration time of 2876 s for each field. The FWHM of the SPIRE beam corresponded to 18.2, 24.9 and 36.3 arcsec at 250, 350 and 500 μm, respectively (see SPIRE Observers' manual). The data were processed using HIPE version v14.0.0 using the standard pipeline for the SPIRE Large Map Mode with extended source calibration. From level 0.5 to level 1, an electrical crosstalk, temperature drift and bolometer time response correction is applied and a wavelet deglitching algorithm is run for all building blocks. To process the level 1 building blocks, we use a script to combine data from different scans. On the combined data set, we ran the destriper (instead of the baseline subtraction) to obtain an optimum fit between all timelines. The *Planck* High Frequency Instrument (HFI) maps at 857 and 545 GHz (350 and 550 μm) were, furthermore, used to determine the absolute scaling of the SPIRE maps with extended emission.[2] We applied colour

[2] Global fluxes for Cas A are 7.6 per cent and 0.9 per cent lower at 250 and 350 μm and 0.5 per cent higher at 500 μm compared to the original SPIRE flux calibration (without including the *Planck* maps to determine the absolute calibration of SPIRE images).
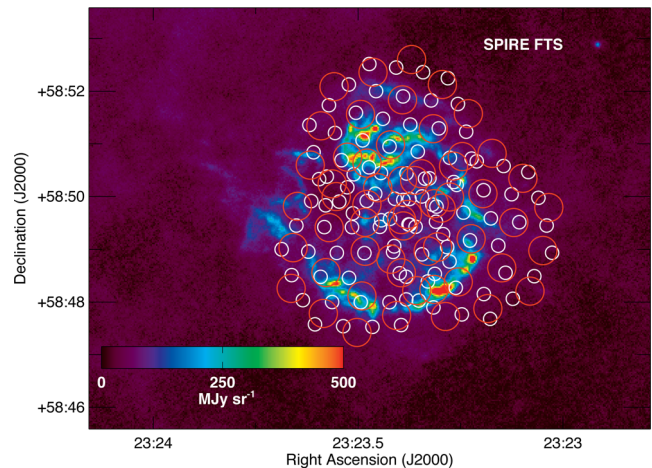

Figure 3. PACS 70 μm image of Cas A, overlaid with the three SPIRE FTS pointings with individual positions for the SSW and SLW detectors indicated as white and orange circles, respectively.

correction factors to the SPIRE 250 μm (0.9875), 350 μm (0.9873) and 500 μm (0.9675) maps, appropriate for a spectrum with $F_\nu \propto \nu^{-2}$. The calibration uncertainties for the SPIRE images are assumed to be 4 per cent, resulting from the quadratic sum of the 4 per cent absolute calibration error from the assumed models used for Neptune (SPIRE Observers' manual[3]) and the random uncertainty of 1.5 per cent on the repetitive measurements of Neptune (Bendo et al. 2013).

2.1.4 SPIRE FTS spectroscopy

The SPIRE Fourier Transform Spectrometer (FTS) spectra were obtained in sparse spatial sampling and high-spectral resolution mode, covering the 194–671 μm wavelength range. Three different regions (centre, north and north-west) were targeted (see Fig. 3) with the two arrays of the bolometer detectors, each with 24 repetitions. The 35 detectors of the SPIRE Short Wavelength (SSW) array covered the 194–313 μm range, while the SPIRE Long Wavelength (SLW) array of 19 detectors covered the 303–671 μm wavelength range. The SSW and SLW detectors have an average FWHM of 19 and 34 arcsec, respectively (Makiwa et al. 2013).

The SPIRE FTS data were reduced in HIPE v14.0.0, with version SPIRE_CAL_14_3 of the calibration files including the latest corrections that match the FTS extended calibration with the SPIRE photometer. We used the standard pipeline in HIPE for the reduction of single pointing SPIRE spectrometer observations, with extended source calibration and without apodization. The standard pipeline included a first- and second-order deglitching procedure, non-linearity and phase corrections, baseline subtraction and corrections for the telescope and instrument emission. The spectral lines in the SPIRE FTS data were fitted with the SPIRE Spectrometer Line Fitting algorithm in HIPE using a sinc function to model the instrumental line shape (Naylor et al. 2014). In addition to the formal uncertainties from line fitting, we add a 10 per cent calibration uncertainty (Swinyard et al. 2014) to the line flux uncertainties.

[3] http://herschel.esac.esa.int/Docs/SPIRE/html/spire_om.html

2.2 Ancillary data

2.2.1 Spitzer

The Infrared Array Camera (IRAC; Fazio et al. 2004), Multi-band Imaging Photometer (MIPS; Rieke et al. 2004) and IRS (Houck et al. 2004) on board the *Spitzer Space Telescope* (Werner et al. 2004) have all targeted Cas A. The MIPS data at 24, 70 and 160 µm were observed as part of the *Spitzer* Early Release Observation program (ID 718, PI: G. Rieke) on 2003 November 30. Cas A was mapped with MIPS at medium scan speed over a total area of 12.7 arcmin × 30 arcmin. More details about the observing strategy and a detailed analysis of the MIPS data for Cas A are presented in Hines et al. (2004). We used the IRAC data for Cas A observed as part of the *Spitzer* program *The Evolution of Dust in Cassiopeia A* (ID 3310, PI: L. Rudnick) on 2005 January 18 (see Ennis et al. 2006 for a description of the observations). We retrieved the IRAC 3.6 and 8 µm and MIPS 24 µm final data products (with 10.4, 10.4 and 3.67 s integration time per pixel, respectively) from the *Spitzer* Heritage archive.[4] Extended source correction factors of 0.91 and 0.74 have been applied to the IRAC 3.6 µm and IRAC 8 µm images, respectively, following the recommendations of the IRAC Instrument Handbook.[5]

The IRAC 3.6 µm map (dominated by synchrotron emission from Cas A) did not require a correction for the shape of the spectrum (assumed to be a power-law spectrum $F_\nu \propto \nu_\alpha$ with α anywhere between -1 and 0, see Section 3.1). We did correct the IRAC 8 µm emission (arising primarily from hot SN dust in Cas A) with a colour correction factor of 0.9818 assuming a blackbody spectrum with a temperature of 400 K. The IRAC 3.6 µm is contaminated by many field stars, which prevents the determination of the fainter synchrotron emission at those wavelengths. We therefore manually selected 64 bright targets in the field of Cas A and replaced the emission within an aperture with radius R (selected to encompass the star's emission) with random background noise. The mean value of the background and background variation has been measured within an annulus with inner radius R and outer radius $2^\star R$.[6] The flux calibration uncertainties in the IRAC 3.6 and 8 µm, and MIPS 24 µm maps are assumed to be 10 per cent (recommended by the IRAC Instrument Handbook) and 4 per cent (Engelbracht et al. 2007), respectively.

We also used the *Spitzer* IRS spectra processed by Rho et al. (2008). More details about the observations and analysis can be retrieved from their paper. The *Spitzer* IRS observations were taken as part of the same *Spitzer* program on 2005 January 13 during a total observing time of 11.5 h. Nearly the entire remnant was mapped with the IRS Short-Low (SL: 5–15 µm) and Long-Low (LL: 15–40 µm) filters using 16 × 360 and 4 × 91 pointings with spectra obtained every 5 and 10 arcsec, respectively. The spectra were reduced using the CUBISM package (Kennicutt et al. 2003; Smith et al. 2007) with the standard IRS pipeline (version S12), including background subtraction and corrections for extended source emission.

We derived a global IRS spectrum for Cas A by extracting the emission within an aperture with radius $R = 165$ arcsec. The SL and LL spectra were scaled to have similar emission in overlapping wavebands. The global spectrum was multiplied by a scaling factor of 1.12 to match the global photometry of the continuum emission in the IRAC 8 µm, *WISE* 12 and 22 µm and MIPS 24 µm wavebands. Based on this global spectrum, we derived the continuum emission for Cas A at 17 and 32 µm to constrain the SED fitting procedure in Section 4. The total flux uncertainties (about 12 per cent) for the IRS spectra and the continuum fluxes were derived by combining the uncertainties in the scaling factors to match the emission in the broad-band filters (11 per cent) and the absolute calibration uncertainty (5 per cent).

2.2.2 WISE

WISE (Wright et al. 2010) observed Cas A in four photometric bands at 3.4, 4.6, 11.6 and 22.0 µm with a resolution of FWHM = 6.1, 6.4, 6.5 and 12 arcsec, respectively. We retrieved the *WISE* 11.6 and 22.0 µm maps for Cas A from the NASA/IPAC Infrared Science Archive.[7] The *WISE* images (in units of DN) were converted to Vega magnitudes using the photometric zero-point magnitudes indicated in the image headers (with the MAGZP keyword). To convert the *WISE* images to flux densities, we applied the zero magnitude flux densities reported in the Explanatory Supplement to the NEOWISE Data Release Products.[8] Three different types of correction factors needed to be applied to extended sources (Jarrett et al. 2013). The first aperture correction factor corrected for the point spread function (PSF) profile fitting that was used for the *WISE* absolute photometric calibration, which required corrections of -0.030 and 0.029 mag for the *WISE* 11.6 and 22.0 µm bands. A second correction factor is the colour correction, which accounts for the shape of the spectrum of Cas A. Since the emission at MIR wavelengths is mostly dominated by warm SN dust, we applied the correction factors applicable for blackbodies with temperatures of 200 and 100 K to the *WISE* 11.6 µm (1.0006) and 22 µm (1.0032) bands. The dust temperatures that dominate the emission at those wavelengths have been inferred from MIR studies of Cas A (Hines et al. 2004; Rho et al. 2008; Arendt et al. 2014). The last correction factor (0.92), which accounts for the calibration discrepancy between *WISE* photometric standard blue stars and red galaxies, only needed to be applied to the *WISE* 22 µm band. We assume calibration uncertainties of 4.5 per cent and 5.7 per cent (Jarrett et al. 2013) for the *WISE* 12 and 22 µm filters.

2.2.3 Planck

Planck (Planck Collaboration I 2011) observed the entire sky in nine submm and mm wavebands during the mission lifetime (2009-2013). The *Planck* satellite had two instruments, with the HFI (Lamarre et al. 2010) operating at 857, 545, 353, 217, 143 and 100 GHz (or wavelengths of 350, 550 and 850 µm and 1.38, 2.1 and 3 mm, respectively) and the Low Frequency Instrument (LFI; Bersanelli et al. 2010) covering the 70, 40 and 33 GHz frequencies (or wavelengths of 4.3, 6.8 and 10 mm). For this analysis, we have used the customized *Planck* flux measurements from Planck Collaboration XXXI (2016) derived from aperture photometry within an aperture optimized for the angular size of Cas A and the beam size at every *Planck* frequency (see Table A1, last row). In Appendix A, we give an overview of the various *Planck* measurements available for Cas A and discuss our choice for these flux measurements.

---

[4] http://sha.ipac.caltech.edu/applications/Spitzer/SHA/

[5] http://irsa.ipac.caltech.edu/data/SPITZER/docs/irac/iracinstrumenthandbook/

[6] This radius was chosen to encompass all of the star's emission and ranges from values of 2 to 7 arcsec across all stars.

[7] http://irsa.ipac.caltech.edu/frontpage/

[8] http://wise2.ipac.caltech.edu/docs/release/neowise/

2.3 Image preparation

The background in each of the maps has been determined by measuring the backgrounds in a sufficiently large number of apertures with radius = 4×FWHM at each waveband. The number of background apertures depended on the size of the background region available, and was typically about 20. The IRAC and MIPS images have a small field of view, while the *Herschel* images are dominated by emission from interstellar material in the Perseus arm which makes it hard to find emission-free regions. We selected regions off the remnant with the final background level chosen to be the mean value from all background apertures. We have chosen to subtract these backgrounds from the images before convolution of all images to the 500 μm resolution.

To compare the emission of Cas A across all wavebands in an unbiased way, we convolved all IR/submm images to the same resolution, which was chosen to be the resolution of the SPIRE 500 μm image (FWHM = 36.3 arcsec). We used the convolution kernels from Aniano et al. (2011) for the convolution of these images to the SPIRE 500 μm resolution. All convolved images were rebinned to the pixel grid of the SPIRE 500 μm map with pixel size of 14 arcsec (or 0.23 pc at the adopted distance of 3.4 kpc for Cas A, Reed et al. 1995). We have furthermore verified that a convolution with kernels produced based on the more recent *Herschel* PACS and SPIRE PSF models derived from dedicated Vesta and Mars observations and published by Bocchio, Bianchi & Abergel (2016b) would not affect the results published in this work. We produced such convolution kernels for the specific *Herschel* observations of Cas A that account for the position angle (PA) of the *Z*-axis of the telescope during the observations of the source and target image, respectively, using the PYPHER (PYTHON-based PSF Homogenization kERnels production[9]) software package. With variations in the global fluxes of Cas A of less than 1 per cent (except at 250 μm with a 2 per cent offset) between the two sets of convolved images, we conclude that the type of kernels used for the convolution of the *Herschel* maps of Cas A will not affect the determination of SN dust masses in Cas A.

For the SED modelling procedure described in Section 4, we need to know the uncertainty on the flux in every pixel. These uncertainties determine how well the model fits the observations, and play an important role in setting the uncertainties on the contributions from different emission components. The main uncertainties are due to errors on the determination of the background levels, calibration uncertainties and uncertainties in the synchrotron subtraction. The background uncertainties are driven by both large-scale background variations and pixel-by-pixel noise. The two independent background errors are computed as the standard deviation of the mean background values derived for different background regions and the mean of the standard deviation of the pixel-by-pixel variation in different background regions, respectively. The uncertainty associated with the subtraction of the synchrotron emission is calculated based on the uncertainties associated with the spectral index and normalization factor determined from the *Planck* data (see Section 3.1).

2.4 Flux comparisons

Table 2 (first column) provides an overview of the global photometric measurements for Cas A. Several other works have studied the

infrared emission from Cas A, which makes it possible to compare our global photometry to other published fluxes. Barlow et al. (2010) used the same set of *Herschel* observations, but their data were reduced with an earlier version of the HIPE data reduction pipeline. It is, therefore, of interest to compare the flux measurements reported by Barlow et al. (2010) to this work for the same aperture. While the PACS 70 μm photometry is consistent within the error bars ($F_{70\,\mu m} = 179 \pm 11$ Jy here and $F_{70\,\mu m} = 169 \pm 17$ Jy from Barlow et al. 2010), the other PACS photometric measurements published by Barlow et al. (2010) ($F_{100\,\mu m} = 192 \pm 19$ Jy, $F_{160\,\mu m} = 166 \pm 17$ Jy) are 17.7 per cent and 29.7 per cent lower compared to the values derived here. In the 160 μm channel we might expect an opposite trend due to the optical field distortion that was not applied in HIPE 12 and all earlier versions (which caused an overestimate of the flux by 6–7 per cent). We believe the flux difference can mainly be attributed to the different data reduction techniques that were used to process the data. While the first HIPE versions only allowed one to reduce data with the standard map making tool `PhotProject`, the latest version of the data reduction was performed with `Scanamorphos`. While `PhotProject` applied a high-pass filtering technique to remove the 1/f noise (mainly due to data with low spatial frequencies or large-scale emission features in the maps), `Scanamorphos` does not make any specific assumptions to model the low-frequency noise and takes into account the redundancy of observations. `Scanamorphos` has been shown to give a better estimate of the background level in PACS maps compared to the `PhotProject` map-making algorithm which can remove or underestimate the emission of extended structures. Given that the field around Cas A is populated with extended emission originating from ISM dust, we believe that the discrepancy between fluxes is largely due to different estimates of the background levels.

In the SPIRE wavebands, our integrated fluxes are also higher by 8.3 per cent, 17.8 per cent and 12.2 per cent compared to the values published by Barlow et al. (2010, $F_{250} = 168 \pm 17$ Jy, $F_{350} = 92 \pm 10$ Jy and $F_{500} = 52 \pm 7$ Jy), but close to being consistent within the error bars. Based on the SPIRE beam areas that were assumed during the early days of *Herschel* observations (501, 944 and 1924 arcsec^2 at 250, 350 and 500 μm, respectively, Swinyard et al. 2010) compared to the more recent estimates (464, 822 and 1768 arcsec^2), we would expect the latest flux densities to be lower. The opposite trend suggests that variations in the background level determination play a prominent role in explaining the different photometric measurements.

Other than by *Herschel*, Cas A has been observed by several other space- and ground-based facilities at similar wavelengths. Based on *Spitzer* MIPS data, Hines et al. (2004) reported a flux density $F_{70} = 107 \pm 22$ Jy. Observations by *AKARI* yielded flux densities of $F_{\nu} = 71 \pm 20$, 105 ± 21 and 92 ± 18 Jy at 65, 90 and 140 μm (Sibthorpe et al. 2010), respectively. Sibthorpe et al. (2010) also remeasured the *ISO* 170 μm flux ($F_{170} = 101 \pm 20$ Jy), and reported *BLAST* 250, 350 and 500 μm photometry ($F_{250} = 76 \pm 16$ Jy, $F_{350} = 49 \pm 10$ Jy and $F_{500} = 42 \pm 8$ Jy). With SCUBA, Dunne et al. (2003) measured flux densities of $F_{450} = 69.8 \pm 16.1$ Jy and $F_{850} = 50.8 \pm 5.6$ Jy. While the SCUBA 450 μm flux is consistent with the SPIRE 500 μm photometry (see Table 2), the MIPS, *AKARI*, *ISO* and *BLAST* measurements are all significantly lower (up to a factor of 2.5) compared to the *Herschel* PACS and SPIRE fluxes derived in this paper. Barlow et al. (2010) came to a similar conclusion and attributed the flux discrepancies to the better resolution in the *Herschel* maps which allows a more accurate background subtraction. Due to the highly structured emission of the ISM material in the surroundings of Cas A, it can become difficult

to determine the background level in an image with poor spatial resolution, due to ISM dust confusion. While the high resolution of *Herschel* images allows us to better resolve the ISM emission from the true background in the IR/submm images, resulting in the recovery of higher flux densities for Cas A, the main difference of our work compared to previous studies, analysing the same set of *Herschel* observations, is the detailed modelling on spatially resolved scales of the different emission components contributing along the sightline towards Cas A. In support of this claim, we repeated the modelling based on the *Herschel* fluxes published by Barlow et al. (2010) and retrieved a total SN dust mass higher by a factor of 3 compared to the global analysis of the *Herschel* data of Cas A by Barlow et al. (2010, see Section 5.2).

3 MODELLING THE VARIOUS EMISSION COMPONENTS

3.1 Modelling the synchrotron component

Based on the latest *Planck* measurements (see Section 2.2.3), we determined the best-fitting spectral index and normalization factor that reproduces the synchrotron emission from Cas A detected by *Planck* from 143 to 44 GHz (or 2 to 7 mm). We refrained from using bands at higher frequencies ($\nu \geq 217$ GHz) due to a possible contribution of the emission and polarization from SN dust (Dunne et al. 2003, 2009) or emission from ISM dust (Krause et al. 2004). We also neglect the 30 GHz flux measurement since the 30 GHz flux for Cas A and for other SNRs reported by Planck Collaboration XXXI (2016) shows an offset from the other *Planck* measurements. In addition to the four *Planck* measurements, we include the IRAC 3.6 μm flux measured within an aperture of radius $R = 165$ arcsec (after masking the stars in the IRAC 3.6 μm image) to constrain the synchrotron spectrum at shorter wavelengths.

Using the Planck Collaboration XXXI (2016) aperture flux measurements at 44, 70, 100 and 143 GHz, a spectral index α and normalization factor C were derived by fitting a function $F(C,\alpha) = C \times \nu^{\alpha}$ (ν in GHz) with spectral index α and scaling factor C to these *Planck* and IRAC 3.6 μm fluxes. Relying on the Levenberg–Marquardt least-squares fitting minimization routine MPFIT in IDL, we derived a best-fitting spectral index $\alpha = -0.644 \pm 0.020$ and normalization factor $C = 1706.7 \pm 199.2$ Jy. Fig. 4 shows the *Planck* fluxes reported by Planck Collaboration XXXI (2016) indicated as black squares, with the red diamonds corresponding to flux measurements for Cas A from other facilities. The best-fitting power-law is indicated as a solid black line. The data point at the highest *Planck* frequency is significantly higher compared to the extrapolation of this power law, due to an increasing contribution of thermal dust emission towards higher frequencies. The dashed red lines correspond to the lower and upper limits of this synchrotron spectrum calculated based on the uncertainties of the spectral index fitting results. These uncertainties on the synchrotron spectrum are considered in the synchrotron models at every photometric wavelength.

Although a spectral index of $\alpha = -0.644$ provides a good fit to the global synchrotron power spectrum in Cas A, local variations in spectral index between different knots have been observed (Anderson & Rudnick 1996; Wright et al. 1999; DeLaney et al. 2014). The shocked ejecta with the brightest synchrotron emission are mostly consistent with this spectral index derived on global scales, while α variations are observed in some knots outside of the reverse shock (DeLaney et al. 2014). A spectral index of $\alpha = -0.644$ is also somewhat shallower compared to
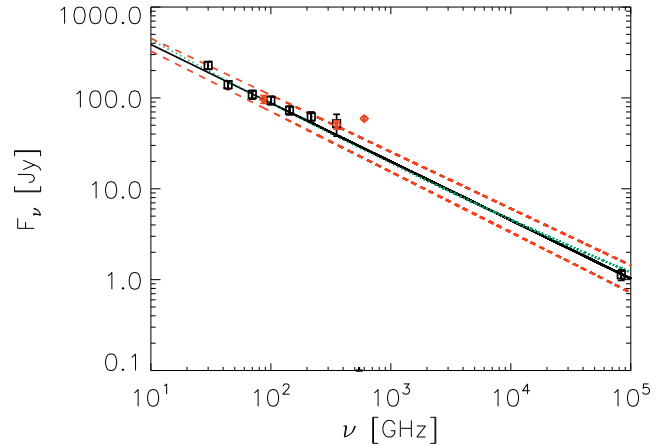

Figure 4. Global flux measurements for Cas A based on *Planck* data (Planck Collaboration XXXI 2016) and *Spitzer* IRAC 3.6 μm observations (black squares). *Planck* fluxes at frequencies 44 GHz $\leq \nu \leq$ 143 GHz and the IRAC 3.6 μm flux are used to constrain the spectral index and normalization of the synchrotron spectrum, while the *Planck* measurements at $\nu \gtrsim$ 217 GHz already have a non-negligible contribution of interstellar and/or SN dust emission. Previous observations of Cas A have been indicated as red diamonds for comparison (see Appendix A). The power law that best describes the synchrotron power spectrum at lower frequencies is indicated as a solid black line. The red dashed lines indicate the upper and lower limits to the synchrotron spectrum, determined from the uncertainties on the spectral index fitting. The green dashed curve shows an extrapolation of the synchrotron spectrum with spectral curvature from Onić & Urošević (2015) which greatly overestimates the IRAC 3.6 μm flux.

the values used in several other studies of Cas A: $\alpha = -0.69$ (Hines et al. 2004), $\alpha = -0.70$ (Barlow et al. 2010) and $\alpha = -0.71$ (Arendt et al. 1999; Rho et al. 2003, 2008), which were based on spectral index measurements at lower frequencies. A flattening of the synchrotron spectrum was suggested by Onić & Urošević (2015) and attributed to non-linear particle acceleration. The best-fitting synchrotron spectrum including spectral curvature ($S_\nu = S_{1GHz} \nu^{-\alpha + a\log \nu} e^{-\tau_0 \nu^{-2.1}}$ with $\alpha = 0.760$, $a = 0.020$, $\tau_0 = 8.559 \times 10^{-5}$, see green dotted curve in Fig. 4) reported by Onić & Urošević (2015, where the scaling relations of Vinyaikin 2014 were used to account for secular fading) is however consistent with the best-fitting synchrotron spectrum derived for Cas A based on *Planck* data in this work.

The BIMA array map of Cas A at 3.7 mm from Wright et al. (1999) was used to determine the spatial distribution of synchrotron emission on subarcsec scales at IR/submm wavelengths by extrapolation (see Fig. 5). The 3.7 mm BIMA map is a multifrequency synthesis mosaic obtained by combining 16 frequency bands between 77 and 85 GHz data to obtain a single map with mean frequency of 83.1 GHz and final resolution of 6.5 arcsec × 6.2 arcsec. The original flux in the BIMA 3.7 mm map was determined by summing the emission within a 165 arcsec radius aperture and a background annulus between 165 and 320 arcsec. The flux calibration of the original 3.7 mm data was updated to $F_{83.1GHz} = 100.5^{+21.9}_{-19.1}$ Jy[10] (or $F_\nu = C \times 83.1^\alpha$) using the scaling factor C (1706.68 $\pm$ 199.20 Jy) and spectral index α (-0.644 ± 0.020) that best reproduces the spectrum of the synchrotron emission in Cas A as determined based on *Planck* and IRAC 3.6 μm data.

---

[10] The flux uncertainty accounts for the errors on the best-fitting parameters, i.e. the spectral index α and normalization factor C.
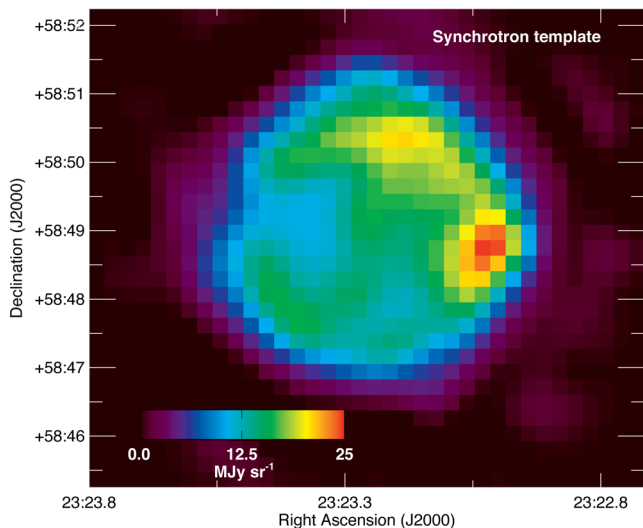
Figure 5. The synchrotron image for the SPIRE 500 μm waveband based on an extrapolation of the 3.7 mm map of Wright et al. (1999) using the best-fitting spectral index and normalization to the *Planck* fluxes (see Section 3.1).

While a power-law slope of -0.644 is assumed for the current synchrotron model based on fits to the 44–143 GHz *Planck* and IRAC 3.6 μm data (see Section 3.1), the synchrotron spectrum slope may not remain constant across the mm to near-infrared frequency range. A power-law fit restricted to the *Planck* data would result in a power-law index of -0.54. If we extrapolate this synchrotron spectrum to submm wavelengths, we find synchrotron contribution which are higher by 3 per cent, 5 per cent and 9 per cent of the total flux at SPIRE 250, 350 and 500 μm wavelengths compared to the synchrotron model presented here. Rerunning the same sets of SED models as presented in Section 4 using the updated synchrotron model resulted in minor changes to the SN dust masses and remained within the limits of uncertainty. The effect of variations in the spectral index on the synchrotron contribution at longer wavelengths is thus negligible compared to the model and observational uncertainties, and small variations in the spectral index will not affect the results presented in this paper.

3.2 The interstellar dust model

To model the emission of interstellar dust towards Cas A, we apply The Heterogeneous dust Evolution Model for Interstellar Solids (THEMIS) dust model (Jones et al. 2013; Köhler, Jones & Ysard 2014) which includes a set of amorphous hydrocarbon grains (a-C(:H)) and silicates with iron nano-particle inclusions (a-Sil$_{Fe}$), for which the optical properties were derived from laboratory studies, and the size distribution and abundances of grain species were calibrated to reproduce the extinction and emission observed in the diffuse interstellar regions in the Milky Way. The shape of the ISM dust emission spectrum depends on the temperature of the emitting dust grains (and thus the strength of the ISRF that is heating these grains) and will determine the peak wavelength of the ISM dust emission (see Fig. 6). To normalize the spectrum, we use the SPIRE 500 μm map (after subtraction of the synchrotron emission, see Fig. 7) as a tracer of the ISM dust mass.

To determine the average temperature of ISM dust along the line of sight to Cas A, we need to derive the scaling factor of the ISRF that is heating the dust. To derive this ISRF scaling factor, we fit the PACS 100 and 160 μm, and SPIRE 250, 350 and 500 μm emission
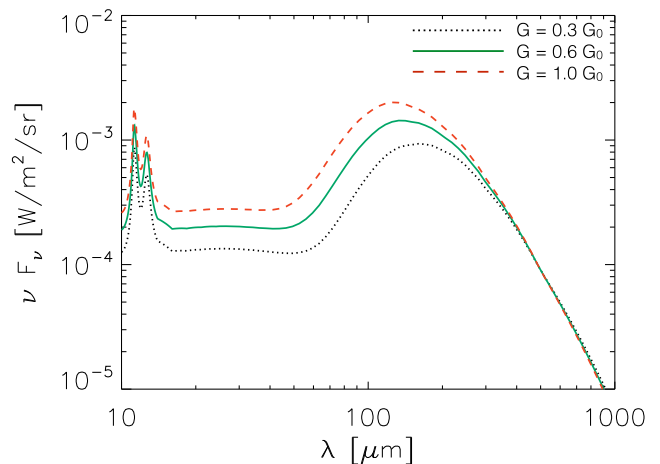

Figure 6. The SED models from the Jones et al. (2013) dust model with ISRF scaling factors $G = 0.3\ G_0$ (dotted black curve), 0.6 G_0 (solid green curve) and 1.0 G_0 (dashed red curve), all normalized to the same SPIRE 500 μm flux.
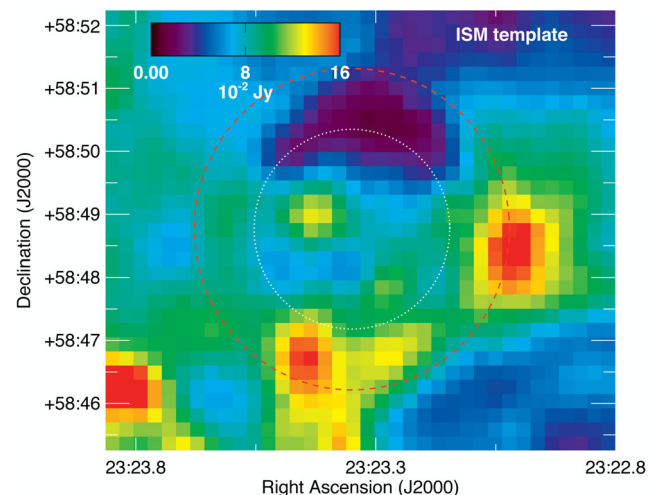

Figure 7. The SPIRE 500 μm map, after subtraction of the synchrotron radiation component, which was used to model the spatial distribution of ISM dust along the line of sight of Cas A. For reference, the position of the forward and reverse shock are indicated as dashed red and dotted white circles, respectively.

in the ISM dust-dominated regions surrounding Cas A with a physically motivated SED model. We exclude a circular patch with radius of 165 arcsec centred on the SNR and retain a sample of 5912 'interstellar dust' pixels (of size 14×14 arcsec^2) with $\geq 5\sigma$ detections in the PACS 160 μm and SPIRE 250, 350 and 500 μm wavebands. We use the SED fitting tool DustEm (Compiègne et al. 2011) to model the dust emission for a prefixed composition of dust grains with a given size distribution, optical properties and dust emissivity. By deriving the dust emissivity for every single grain species of a given size and composition (based on a dust temperature distribution), the non-local thermal equilibrium emission for grain species of all sizes has been taken into account. We create a library of SED models with $G \in [0.1, 2.5]\ G_0$ (with steps of 0.1) and $N_H \in [2.5, 76] \times 10^{21}$ cm^{-2} (with stepwise increase by a factor of 1.05) to find the SED model that best fits the observations. The shape of the ISRF is chosen to be similar to the radiation field in the solar neighbourhood (Mathis, Mezger & Panagia 1983). The best-fitting
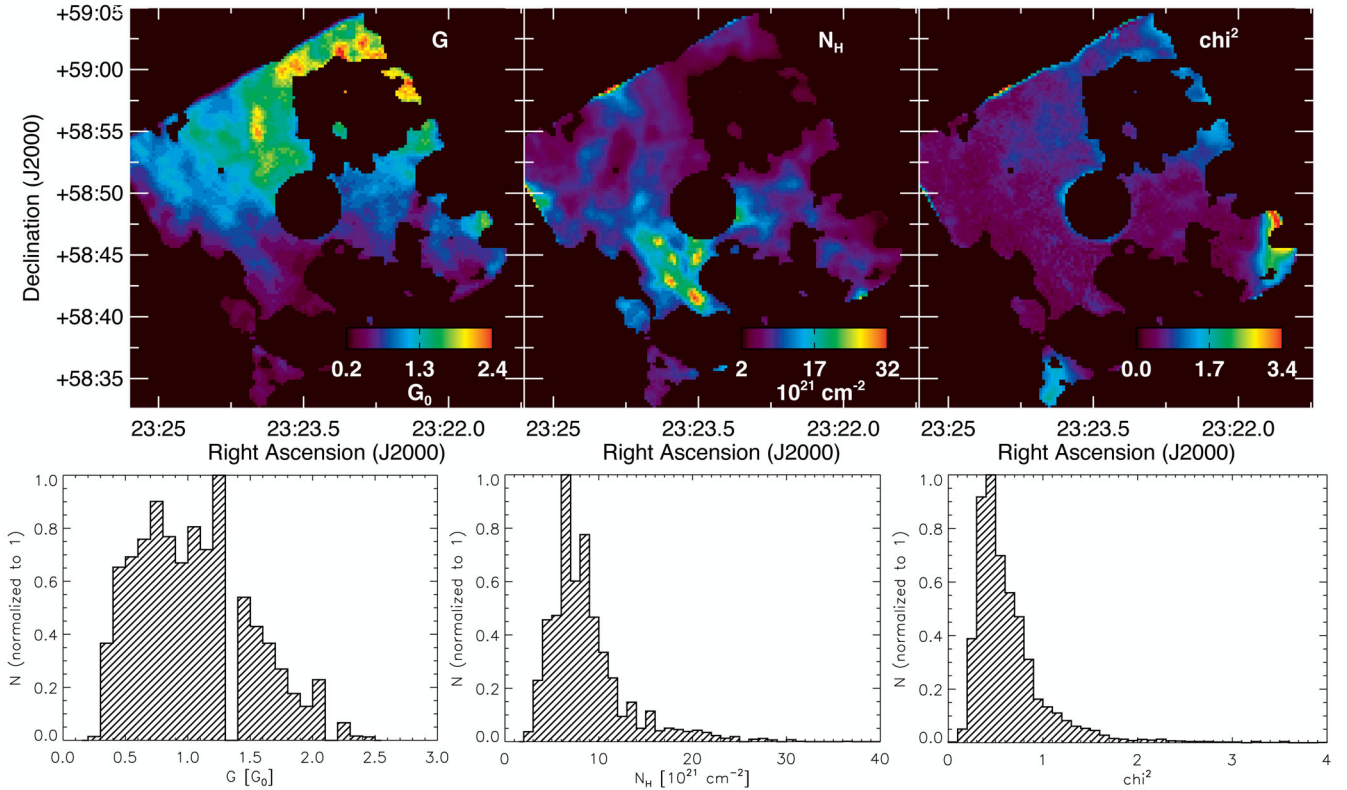
Figure 8. Top row: maps of the best-fitting G and N_H model parameters, and reduced χ^2 values. Bottom row: normalized histograms displaying the distribution of G, N_H and χ^2 values for all 5912 ISM dust pixels.

SED model is determined from a least-squares fitting procedure to the PACS and SPIRE data points. We performed the fitting on the PACS and SPIRE images without applying colour corrections since the model SED was convolved with the filter response curves.

Fig. 8 (top panel) shows the resulting maps of the best-fitting G and N_H parameters and corresponding χ^2 values for the best-fitting model in every pixel, while the bottom panels shows the distribution of G and N_H parameter values, and the reduced χ^2 values for all ISM dust pixels. With a reduced χ^2 peaking below 1 for most pixels, we are confident that the Jones et al. (2013) dust model is adequate to fit the ISM dust component surrounding Cas A. The scaling factor ranges between values of $G = 0.2\,G_0$ and $G = 2.4\,G_0$ corresponding to dust temperatures between $T_d = 13.7$ and 20.6 K.[11] In the immediate surroundings of Cas A (see Fig. 8), the G values range between $0.3\,G_0$ and $1.5\,G_0$.

To constrain the variations in the radiation field G, we require a method to derive the ISRF scaling factor along the sightline of Cas A. Due to the contribution of SN dust emission at infrared wavelengths, we cannot derive the ISRF scaling factor G based on SED modelling.[12] In Appendix C, we present a PDR modelling

technique to derive the ISRF scaling factor based on PDR model parameters derived from [CI] $1-0$, $2-1$ and CO(4−3) line intensities originating from ISM material along the line of sight to Cas A. For most of the sightlines towards Cas A, we retrieve an ISRF scaling factor of $0.6\,G_0$ with some exceptions where ISRF scaling factors of $0.3\,G_0$ and $1.0\,G_0$ seem to fit better. We have, therefore, performed the SED fitting procedure described in Section 4 assuming an ISM dust model with scaling factor of $G = 0.6\,G_0$. The difference between assuming ISRF scaling factors of $G = 0.3\,G_0$ and $G = 1.0\,G_0$ can result in a factor of 2 variation in the ISM dust emission at PACS 100 and 160 μm wavelengths (see Fig. 6), and will thus be an important constraint in accurately recovering the dust mass within Cas A. In Appendix E2, we compare the SN dust masses and temperatures retrieved from SED modelling using three different ISM dust models with scaling factors $G = 0.3\,G_0$, $0.6\,G_0$ and $1.0\,G_0$, or ISM dust temperatures of $T_d = 14.6$, 16.4 and 17.9 K, respectively.

Other than the strength of the radiation field illuminating the ISM dust, we need to estimate the column density of ISM material along the sightline of Cas A. We assume that the SPIRE 500 μm band is mostly dominated by ISM dust emission (after subtraction of the synchrotron component) and thus is a good tracer of the ISM material. Fig. 9 (left-hand panel) shows the relation between the SPIRE 500 μm and the ISM dust mass derived from SED fits for the 5912 ISM pixels in the regions surrounding Cas A. The dashed red line shows the best-fitting trend, with a slope of 0.692, while the solid green line shows a linear correlation with slope of 1 for comparison. The relatively small dispersion (0.074 dex or an

---

[11] These dust temperatures were calculated by taking the average of the mean equilibrium temperatures for amorphous silicate grains with a forsterite-type and enstatite-type chemical composition based on the temperatures derived by DustEm for each grain species of a given size. To determine the mean equilibrium temperature for forsterite and enstatite grains, we have weighted the individual grain temperatures with the density for grains in a given size bin.

[12] We have experimented with using the SPIRE 250 μm-to-SPIRE 350 μm colour to constrain the scaling factor of the ISRF, but this technique proved

unsuccessful due to the contribution from SN dust to the SPIRE wavebands and the dispersion in the correlation between the colour ratio and G.
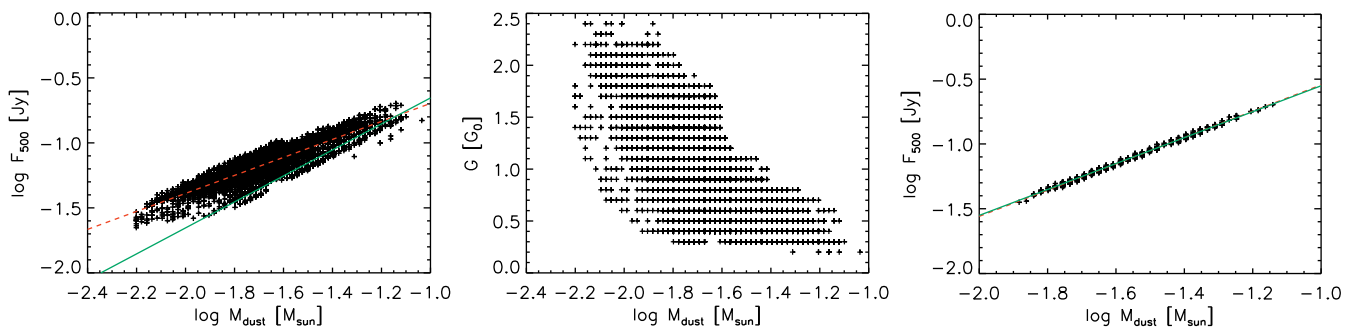
Figure 9. Left: correlation between the SPIRE 500 μm flux density and the ISM dust mass derived by fitting the dust SED with `DustEm`. The dashed red line corresponds to the best-fitting relation $y = ax + b$ with slope $a = 0.692$, while a linear correlation is indicated as a solid green curve for comparison. The dashed red line is the best-fitting trend while the solid green curve represents a linear correlation. Middle: correlation between the ISM dust mass and scaling factor of the radiation field. Right: correlation between the SPIRE 500 μm flux density and the ISM dust mass for pixels with $G = 0.6\,G_0$.

uncertainty of 19 per cent) around the best-fitting trend makes us confident that the SPIRE 500 μm flux density is a good tracer of the ISM dust mass. The main uncertainty on the ISM dust model, thus, arises from the ISRF scaling factor ($G = 0.3$, 0.6 or 1.0 G_0) that illuminates the dust.

While we might expect a relation between the SPIRE 500 μm flux density and ISM dust mass that is closer to linear, the trend in Fig. 9 shows a clear deviation from linearity. Moving to larger dust masses, the SPIRE 500 μm flux shows a smaller increase and does not increase proportionally to the dust mass. We believe that this trend is driven by the anticorrelation between the dust mass and the scaling factor of the radiation field, i.e. regions with higher dust mass are exposed to softer radiation fields (see Fig. 9, middle panel). The latter trend is not surprising given that less UV photons will be able to penetrate regions of higher density, which results in lower G values in regions of high density. Since the same dust mass illuminated by a radiation field with $G = 2.4\,G_0$ (which is the maximum G found among the 5912 interstellar dust regions) will be 2.5 times more luminous at 500 μm compared to the same dust content irradiated by a $G_0 = 0.2$ radiation field (which corresponds to the minimum G), the deviation from non-linearity (which corresponds to more or less a factor of ~2.5 across the covered range in F_{500}) seems driven by the variation in radiation field that is heating the dust. Although the dust emission might become optically thick at higher dust column densities, this does not seem to play a major role in the flattening of the trend here.

To take into account the dependence on G in the relation between the SPIRE 500 μm flux and dust mass, we fit individual relations of the form $\log F_{500} = a \times \log M_d + b$ for pixels with best-fitting scaling factors a and b for $G = 0.3\,G_0$, 0.6 G_0, and 1.0 G_0 (i.e. the radiation fields that are explored in our SED fitting analysis). The best-fitting relations (depending on the assumed value for G) were found to be

$$\begin{aligned} F_{500}\,(Jy) &= 2.093 \times M_d^{1.008}\,(M_\odot) \text{ for } G = 0.3\,G_0 \\ &= 2.943 \times M_d^{1.014}\,(M_\odot) \text{ for } G = 0.6\,G_0 \\ &= 3.204 \times M_d^{0.979}\,(M_\odot) \text{ for } G = 1.0\,G_0. \end{aligned} \quad (1)$$

These relations for a given value of G show a trend that is very close to linear, and have significantly smaller dispersions (0.002, 0.003 and 0.002 dex, respectively) corresponding to uncertainties smaller than 1 per cent (see Fig. 9, right-hand panel for the trend for $G = 0.6\,G_0$). To model the interstellar dust emission, the ISM dust models with $G = 0.3\,G_0$, 0.6 G_0, and 1.0 G_0 are scaled to the dust mass derived based on the SPIRE 500 μm flux density and

the above relations. More specifically, the ISM scaling factor is allowed to vary between $[0.75, 1.0] \times F_{500}$(thermal) $\pm\,\sigma_{500}$, where F_{500}(thermal) corresponds to the SPIRE 500 μm flux density after subtraction of the synchrotron radiation. The maximum contribution of 25 per cent from SN dust emission at 500 μm is an arbitrary upper limit, and is never reached during the SED fitting procedures with typical values of a few per cent up to a maximum of 19 per cent.

3.3 The SN dust model

We use a three component SN dust model for Cas A with hot, warm and cold SN dust components with dust temperatures T_d in the ranges [100 K, 200 K], [40 K, 100 K] and [10 K, 40 K], respectively.[13] The dust composition for the hot SN dust component ($Mg_{0.7}SiO_{2.7}$) was derived based on studies of the *Spitzer* IRS spectra by Rho et al. (2008) and Arendt et al. (2014). The unusual peaks in Cas A's dust emission spectrum at 9 and 21 μm suggest that most of the hotter dust in the ejecta is not composed of the silicates present in the general ISM, but instead corresponds to magnesium silicate grains with low Mg-to-Si ratios ($Mg_{0.7}SiO_{2.7}$, Arendt et al. 1999; Rho et al. 2008; Arendt et al. 2014).

The composition of the warm and cold dust in Cas A is less well constrained due to the absence of obvious dust features. We therefore explore the effect on the dust SED modelling and mass determinations of using different dust species to model the warm and cold dust component in Cas A. In order to identify the particular type of silicates and/or other grain compositions that produce each of the characteristic SEDs, we assembled a set of grain absorption efficiencies from published optical constants (see Table 3). The selected dust composition is consistent with grain species that result from the spectral fitting to the IRS spectra and *Herschel* PACS data by Arendt et al. (2014). In addition to the amorphous carbon grains from Rouleau & Martin (1991), we explore the results of SED fitting with H-poor carbonaceous solids with a band gap of 0.1 eV (Jones 2012a,b,c),[14] which allows us to show the effect of variations in optical grain properties on the carbonaceous dust mass. The optical properties of these a-C grains with a narrow-band gap

---

[13] While the temperature distribution of the dust in Cas A might be better approximated by a continuous distribution, the three different dust components give an idea of the average temperatures to which the different dust components in Cas A are heated.

[14] The latter aromatic carbonaceous grains are also used in the THEMIS dust model to reproduce the ISM dust emission in our Galaxy.

Table 3. Overview of the different dust grain species that are explored in this paper to model the composition of the warm and cold SN dust components in Cas A. For each dust composition, the wavelength range and reference for the optical properties are given. To compare the dust emissivity of different grain species, we also include the dust mass absorption coefficients at 160 μm, $\kappa_{abs, 160}$, which were calculated for spherical grains of radius a = 1 μm using Mie theory. The last two columns give the maximum dust masses for the different dust species that can be formed in Cas A, based on predicted elemental yields from nucleosynthesis models for an SN type II (Woosley & Weaver 1995) and type IIb event (Nozawa et al. 2010). We rely on the elemental abundances predicted by Woosley & Weaver (1995) for a 30 $M_\odot$ progenitor star, while Nozawa et al. (2010) calculates the elemental abundances for a progenitor with initial mass of 18 $M_\odot$.

Dust species	λ (μm)	Ref	$\kappa_{abs, 160}$ (cm^2 g^{-1})	Type II $M_{d, max}$ ($M_\odot$)	Type IIb $M_{d, max}$ ($M_\odot$)
$MgSiO_3$	0.2–500	1	12.7	1.37	0.38
$Mg_{0.7}SiO_{2.7}$	0.2–470	2	1.3	1.21	0.34
$Mg_{2.4}SiO_{4.4}$	0.2–8200	2	16.4	0.93	0.29
Al_2O_3-porous	7.8–500	3	45.3	0.10	0.02
Al_2O_3-compact	7.8–200	3	36.1	0.10	0.02
$CaAl_{12}O_{19}$	2–10 000	4	5.7	0.11	0.02
Am. carbon 'AC1'	0.01–9400	5	33.0	0.29	0.11
Am. carbon 'BE1'	0.01–9400	5	39.7	0.29	0.11
a-C (E_g = 0.1 eV)	0.022–1000 000	6	25.4	0.29	0.11

References: 1: Dorschner et al. (1995); 2: Jäger et al. (2003); 3: Begemann et al. (1997); 4: Mutschke et al. (2002); 5: Rouleau & Martin (1991); 6: Jones (2012a,b,c).

have been calibrated on laboratory data. Dust mass absorption coefficients have been calculated from the complex refractive index for each dust species using Mie theory (Mie 1908) assuming spherical grains of size a = 1 μm.[15] For dust species which lacked dust optical properties up to 1000 μm, we extrapolated the available dust mass absorption coefficients to mm wavelengths. For silicate-type grains, we assumed a λ^{-2} power-law behaviour, while for Al_2O_3 the variation of κ_{abs} with wavelength was fit with a power law between 50 and 200 μm in order to extrapolate the dust mass absorption coefficients to longer wavelengths. We adopted mass densities of 1.6 g cm^{-3} for amorphous carbon grains and 2.5 g cm^{-3} for all the silicate and oxygen-rich grains (Jones et al. 2013). The last two columns in Table 3 present the maximum dust masses derived based on nucleosynthesis models for type II and type IIb events for progenitors with masses similar to Cas A, assuming that all produced metals are locked into dust grains.

The progenitor of Cas A has been suggested to have been a Wolf–Rayet star with a high nitrogen abundance (Fesen et al. 2001) and an initial mass between 15 and 30 $M_\odot$ (Kifonidis, Müller & Plewa 2001; Young et al. 2006). A higher progenitor mass (∼30 $M_\odot$) is favoured based on chemical abundance studies (Pérez-Rendón, García-Segura & Langer 2002, 2009), while other analyses have suggested a lower initial progenitor mass of 23 $M_\odot$ (Pérez-Rendón et al. 2009). For a solar metallicity star with an initial mass of 30 $M_\odot$,[16] the CCSN models of Woosley & Weaver (1995) predict elemental yields for hydrogen (10.5 $M_\odot$), carbon (0.29 $M_\odot$), nitrogen (0.10 $M_\odot$), oxygen (3.65–4.88 $M_\odot$), neon (0.44–0.49 $M_\odot$), magnesium (0.27–0.35 $M_\odot$), aluminium (0.04–0.05 $M_\odot$) and silicon (0.14–0.38 $M_\odot$). For each of the grain species listed in

Table 3, we have calculated the maximum dust mass that is possible to condense in the ejecta of Cas A based on the elemental abundances predicted by the above SN models for a 30 $M_\odot$ progenitor star. Given that Cas A resulted from an SN type IIb explosion (rather than type II), we have also listed the maximum dust masses derived from the nucleosynthesis models of Nozawa et al. (2010) for a type IIb SN with a progenitor mass of 18 $M_\odot$, based on their total elemental abundances predicted for carbon (0.114 $M_\odot$), oxygen (0.686 $M_\odot$), magnesium (0.107 $M_\odot$), aluminium (9.31 × 10^{-3} $M_\odot$), silicon (0.107 $M_\odot$), sulphur (3.33 × 10^{-2} $M_\odot$) and other heavy elements (7.92 × 10^{-2} $M_\odot$). The maximum dust masses derived from the SN type IIb model are factors of 3–5 lower compared to the Woosley & Weaver (1995) model predictions. Since we only have the elemental yields predicted for a type IIb event for 18 $M_\odot$ progenitor, the latter maximum dust masses might be uncertain by factors of a few due to the uncertainties on the initial mass of Cas A's progenitor.

Fig. 10 presents the dust mass absorption coefficients for different grain species as a function of wavelength. We restrict our SED fitting analysis to large grains of radius a = 1 μm, which has been shown to be a representative size for grains in nearby SNRs (e.g. Gall et al. 2014; Owen & Barlow 2015; Wesson et al. 2015; Bevan & Barlow 2016). The assumed size of the grains does not however strongly affect the dust emissivity at IR/submm wavelengths.[17] The large variations in dust mass absorption coefficients at longer wavelengths imply that the dust mass derived from SED fitting will depend strongly on the assumed dust composition. The dust mass absorption coefficients for the different grain species explored in this work are also compared to the absorption efficiencies of typical ISM dust grains. For reference, we overlay the κ_λ values for the large a-C(:H) grains and large carbon-coated, amorphous silicate grains with metallic iron nano-particle inclusions (a-Sil$_{Fe}$) and with a forsterite-type or enstatite-type chemical composition composing the THEMIS dust model that is representative for Galactic ISM dust at high Galactic latitude.

---

[15] Because the dust mass absorption coefficients are very similar for the porous and compact Al_2O_3 dust species and amorphous carbon 'AC1' and 'BE1' type grains, we have only done the SED modelling for porous Al_2O_3 and amorphous carbon 'AC1' grains.

[16] We take an average of the 30A and 30B models of Woosley & Weaver (1995) which have initial expansion velocities of v = 12 700 km s^{-1} and v = 18 000 km s^{-1}, and ^{56}Ni masses of 0 and 0.44 $M_\odot$. The observed v_{max} (14 000 km s^{-1}, Fesen et al. 2006) and ^{56}Ni mass (0.058–0.16 $M_\odot$, Eriksen et al. 2009) for Cas A seem to lie in between these two models.

[17] Assuming a grain size of a = 0.1 μm would only change the SN dust masses within the model uncertainties.

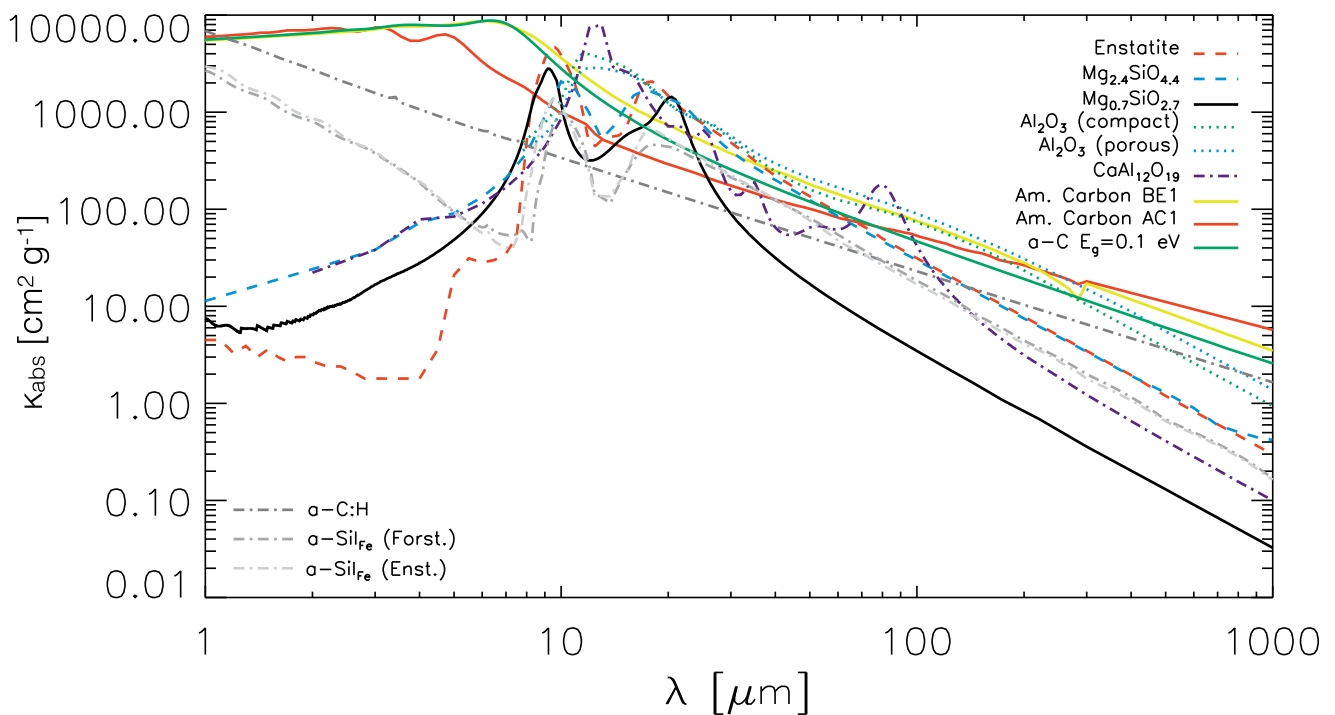**Figure 10.** The variation as a function of wavelength in dust mass absorption coefficients, κ_{abs}, calculated based on Mie theory for spherical grains of size $a = 1\,\mu$m, for different dust species. The legend in the top right corner clarifies the composition of the different dust species, whose sources are listed in Table 3. For reference, the dust mass absorption coefficients for the grain species [large a-C(:H) grains and large carbon-coated, amorphous silicate grains with metallic iron nano-particle inclusions (a-Sil$_{Fe}$) and with a forsterite-type or enstatite-type chemical composition] constituting the THEMIS dust model typical of ISM dust in our Galaxy are indicated as dark, intermediate and light grey dash–dotted lines (cf. legend on the bottom left).

The SN dust emission is modelled by multiplying the dust mass absorption coefficient, κ_λ, with the emission spectrum of a modified blackbody of a given temperature. We assume optically thin dust emission. The dust mass is then derived from

$$F_\nu = \frac{M_d}{D^2}\,\kappa_\nu\,B_\nu(T) \qquad (2)$$

for a single temperature SN dust model with F_ν, the observed flux density at frequency ν in W m^{-2} Hz^{-1}; M_d, the dust mass in g; κ_ν, the dust mass absorption coefficient at frequency ν in cm^2 g^{-1}; D, the distance to Cas A in cm and $B_\nu(T)$, the Planck function describing the emission of a blackbody with temperature T. To model the IR–submm emission across the entire spectrum, we sum the three SN dust model components with different dust temperatures.

4 DUST SED MODELLING AND RESULTS

We aim to derive the contribution of dust emission intrinsic to Cas A, and its mass. To do this, we fit a multicomponent SED model to the *Spitzer* IRS continuum at 17 and 32 μm,[18] and to the *WISE* 22 μm, MIPS 24 μm, PACS 70, 100 and 160 μm and SPIRE 250, 350 and 500 μm data points, which were corrected for line contamination (see Appendix B) and synchrotron emission (see Section 3.1). We omit the IRAC 8 μm and *WISE* 12 μm data points from the SED

fitting procedure to avoid biases introduced by the fitting of the MIR emission features, which have been attributed to aromatic-rich nano-particles. At the same time, the dust emission originating from the reverse shock regions that dominates in those MIR wavebands comes from a hot (~500 K) SN dust component. To avoid the addition of another SN dust component in the SED model, we restrict the SED fitting procedure to the wavelength domain from 17 to 500 μm.

To reproduce the multiwavelength spectrum, we construct a four-component SED model with an ISM dust component and hot, warm and cold SN dust components. For the ISM dust model, we adopt the ISM dust model from Jones et al. (2013) for a radiation field of $G = 0.6\,G_0$ (see Section 3.2). We have modelled the SN dust emission in Cas A with a fixed dust composition of silicates with a low Mg/Si ratio of 0.7 (i.e. Mg$_{0.7}$SiO$_{2.7}$) for the hot dust component, and different dust compositions for the warm and cold dust in Cas A (see Section 3.3). For every SED fit, we assume a single dust composition for the warm and cold SN dust components since the relative abundances of different dust species could not be constrained in our SED modelling procedure due to model degeneracies. The SED fits for a single dust composition provide the SN dust masses assuming the cold+warm SN dust component is entirely made up of these dust species. It is however likely that the warm+cold SN dust is composed of a combination of these various dust species[19] with an

---

[18] We included the continuum emission from the *Spitzer* IRS spectra at 17 and 32 μm to constrain the continuum spectrum at wavelengths shortwards and longwards of the 21 μm peak. Without these constraints, it was impossible to constrain the dust temperature and the exact contribution from the hot and warm SN dust components, which would affect the fitting of the colder SN dust.

[19] Several studies have indicated that the SN explosion that produced Cas A was highly asymmetric and turbulent (Fesen 2001; Fesen et al. 2006; DeLaney et al. 2010; Milisavljevic & Fesen 2015; Orlando et al. 2016). The stratification of ejecta and mixing of heavy elements (Hammer, Janka & Müller 2010) will determine the composition and amount of dust formed in different parts of the remnant.

SN dust mass in between the values retrieved for the various dust compositions.

We require a total of seven parameters to fit the IR/submm SN dust emission from Cas A and the surrounding ISM dust. The seven free parameters include the dust mass and temperature for the hot, warm and cold SN dust components, and the scaling of the ISM dust model in the range $[F_{500} - \sigma_{500} - (0.25 \times F_{500}), F_{500} + \sigma_{500}]$.[20] With 10 different data points to fit the shape and intensity level of the SED in every pixel, we are able to constrain each of these parameters. The best-fitting parameters are determined from a Levenberg–Marquardt least-squares fitting procedure in IDL using the function MPFIT.

To locate the position of dust grains that were formed in Cas A, we performed a spatially resolved fit to the IR/submm images. We did a similar global SED fitting analysis for which the results are presented in Appendix D.[21] To test that pixels were independent, we rebinned the pixels to a size of 36 arcsec which corresponds to the FWHM of the SPIRE 500 µm beam. For aesthetic purposes, we present the output maps from the SED fitting using the nominal pixel size of 14 arcsec for the SPIRE 500 µm waveband and verified that the results are similar to the lower resolution maps. We only fitted pixels within an aperture radius of 165 arcsec centred on Cas A and with detections above 3σ in both the PACS 100 and 160 µm wavebands. For maps with pixel sizes of 14 and 36 arcsec, this resulted in the determination of best-fitting parameters for 438 and 79 pixels, respectively. We omitted some pixels with unrealistically low cold dust temperatures (≤ 14 K) at the edge of the map.

Fig. 11 shows representative SEDs for three individual pixels in different regions of Cas A (Fig. 12 shows the location of these pixels). The first position coincides with a position inside the reverse shock region with an SN dust contribution representative for the unshocked ejecta. The second SED originates from a peak in the cold dust mass in the unshocked ejecta. Although the ISM contribution is dominant in the SPIRE wavebands, the SN dust contribution dominates at PACS 70 and 100 µm. The third SED shows a representative SED of a reverse shock region in the north. The hot and warm SN dust components clearly dominate in this region, with a smaller contribution from ISM dust emission (which is consistent with the lower SPIRE 500 µm flux in this region). While the IRAC 8 µm and *WISE* 12 µm fluxes were not used to constrain the SED model parameters, the ISM+SN dust model reproduces these two MIR constraints of the SED in the middle panel. The SEDs in the top and bottom panels show an excess of 8 and 12 µm emission relative to our best-fitting model, which likely can be attributed to the presence of a hotter SN dust component in Cas A (aromatic-rich nano-particle variations in the ISM might play a role as well). Arendt et al. (2014) show that part of the SN dust in Cas A reaches dust temperatures of $T_d \sim 400$–500 K which would emit at these near-infrared wavelengths.

Table 4 presents the best-fitting dust masses and temperatures derived from the spatially resolved SED fitting procedure. Dust masses are derived by summing the contributions from individual pixels. The dust temperatures and their uncertainties are determined

as the median and standard deviation of the dust temperatures for individual pixels. Depending on the dust composition, the modelled mass of the cold SN dust component in Cas A can vary by more than two orders of magnitude. We derive dust masses of 0.3 $M_\odot$ ($Mg_{2.4}SiO_{4.4}$) and 0.5 $M_\odot$ ($MgSiO_3$) for silicate-type grains, while SN dust masses of 0.5–0.6 and 0.3 $M_\odot$ are derived for carbonaceous and Al_2O_3 grains, respectively. The highest dust masses (several tens of $M_\odot$) are retrieved for $Mg_{0.7}SiO_{2.7}$ and hibonite ($CaAl_{12}O_{19}$) dust compositions. However, based on the elemental abundances predicted from nucleosynthesis models (see Table 3), some of these high dust masses can already be ruled out due to the expected lack of material to form such grains. With unrealistically high dust masses needed to reproduce the IR–submm dust SED, we can exclude $Mg_{0.7}SiO_{2.7}$, $CaAl_{12}O_{19}$ and Al_2O_3 grains as the dominant dust species in Cas A. Also amorphous carbon grains might not be a plausible major dust component in Cas A due to the overwhelmingly oxygen-rich composition of the remnant (Chevalier & Kirshner 1979; Docenko & Sunyaev 2010). Due to the presence of a variety of metals in different parts of the SN ejecta (e.g. Rho et al. 2008; Arendt et al. 2014), the condensation of SN dust with a range of different dust compositions throughout the remnant might be more realistic.[22] Assuming the condensation of SN dust composed for 50 per cent of silicate-type grains and for 50 per cent of carbonaceous grains (a similar relative dust fraction is favoured in Bevan, Barlow & Milisavljevic 2016 to reproduce the Cas A line profiles), we would require a total SN dust mass between 0.4 and 0.6 $M_\odot$ (which combine the lower and upper bounds of the results for carbonaceous and silicate-type grains) to reproduce the observations.

To derive a lower limit to the dust mass present in Cas A, we restrict the scaling factor of the ISM dust model so that it reproduces all of the SPIRE 500 µm flux (after subtraction of the synchrotron emission), equivalent to no SN dust contribution at 500 µm. While this scenario is unlikely, given that the SCUBA 850 µm polarization data imply a contribution from dust (Dunne et al. 2009), we interpret the resulting SN dust masses as strict lower limits. For $MgSiO_3$ and $Mg_{2.4}SiO_{4.4}$ grain compositions, we derive lower limits of >0.2 and >0.1 $M_\odot$ based on spatially resolved SED fitting, respectively. A lower limit of >0.03 $M_\odot$ of Al_2O_3 or >0.03–0.05 $M_\odot$ of amorphous carbon grains would be sufficient to reproduce the IR/submm SEDs on spatially resolved scales, and not violate the predictions of nucleosynthesis models for metal production.

Fig. 12 presents the SN dust mass and temperature maps that were derived from SED modelling assuming an $Mg_{0.7}SiO_{2.7}$ composition for the hot component and an $MgSiO_3$ composition for the warm and cold SN dust components, respectively, for an ISM model with ISRF $G = 0.6\ G_0$. The last row shows the total dust mass map and the reduced χ^2 values representative for the goodness of the fit in every pixel. The positions of the forward and reverse shock as determined by Gotthelf et al. (2001) based on *Chandra* X-ray data (at radii of 153 and 95 arcsec, respectively) have been overlaid on the total dust mass map (bottom left) as dashed red and dotted white lines, respectively.

The temperature maps in Fig. 12 make it clear that the dust mass components in Cas A are heated to different temperatures. The

---

[20] We do not consider the scaling factor of the radiation field G, that illuminates the ISM dust, as a free parameter, since we assume a fixed value (0.3, 0.6 or 1.0 G_0) for the different SED fitting procedures.

[21] Due to strong variations in ISM contributions and SN dust temperatures across the field of Cas A, we believe that the average global spectrum does not capture the local variations within Cas A very well. We therefore prefer to rely on the SN dust masses and temperatures derived from the resolved SED fitting analysis.

[22] The formation of carbonaceous grains is dependent on predictions of nucleosynthesis models. While Nozawa et al. (2010) predict that around 40 per cent of the 0.2 $M_\odot$ newly formed dust grains in their models have a carbonaceous composition, Bocchio et al. (2016a) predict the formation of predominantly silicate-type grains with 0.1 $M_\odot$ of carbon grains out of the 0.8 $M_\odot$ modelled dust mass for Cas A.
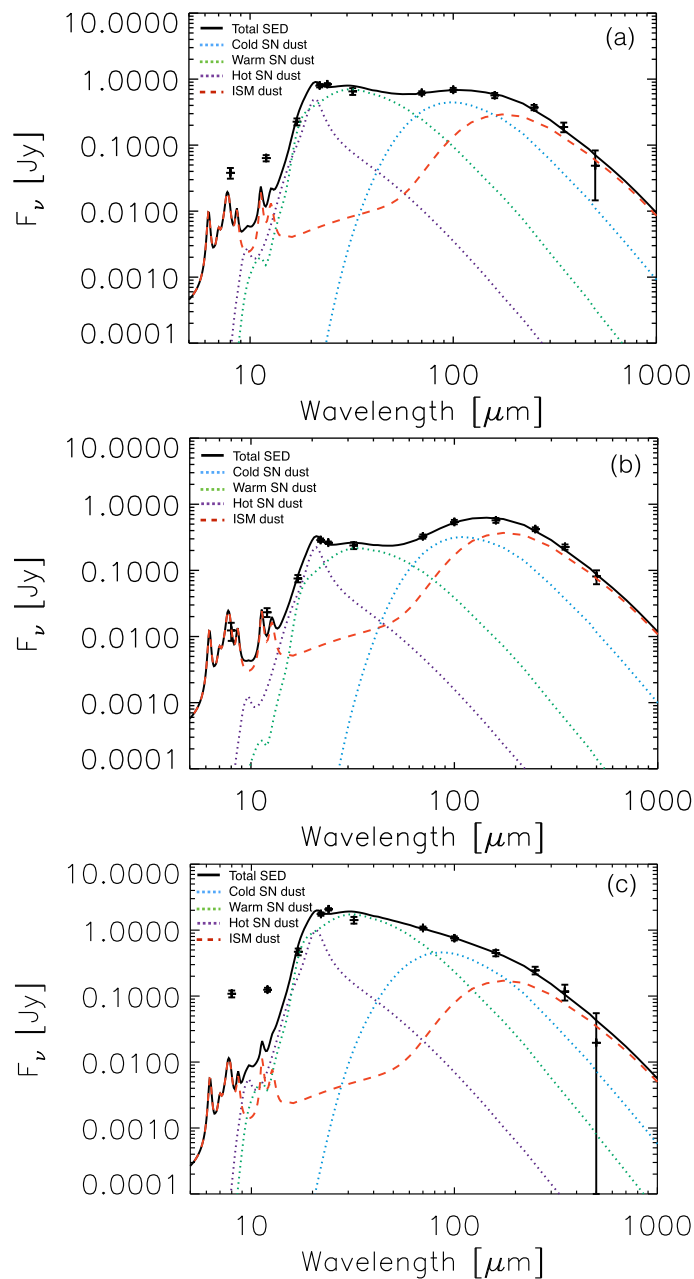
Figure 11. Spatially resolved SED fits constrained by the 17–500 μm photometry for three pixels (whose locations are shown in Fig. 12) targeting different regions of the SNR. The different SED components are outlined in the legend on the top left of every panel.

temperature of the 'cold' dust component in Cas A varies from ~25 to ~30 K interior to the reverse shock, and reaches temperatures of ~30 to ~35 K in the outer ejecta. The warm dust component has temperatures of around 80 K (similar to the temperature $T_d = 82$ K derived by Hines et al. 2004 to fit the *Spitzer* IRAC and MIPS fluxes), and is distributed over the reverse shock regions. An additional hotter dust component (with T_d around 100 K) and an $Mg_{0.7}SiO_{2.7}$ dust component are required to fit the spectral peak at 21 μm in the observed SED of Cas A.

The sum of all these dust components yields a total dust mass map (bottom left panel in Fig. 12). This total dust mass map shows a relatively smooth distribution in the unshocked inner regions, with a peak south-east of the centre of the remnant, which seems to suggest that dust formed more or less uniformly in the inner ejecta of

Cas A. The average dust column density of the inner ejecta is about 0.0025 $M_{\odot}$ pixel^{-1} with a peak of 0.004 $M_{\odot}$ pixel^{-1} while the cold SN dust column density quickly drops to about 0.001 $M_{\odot}$ pixel^{-1} (and lower) in the outer ejecta. Since the ISM dust contribution varies widely along the sightlines to Cas A (see Fig. 7), the confinement of the cold SN dust component to the unshocked ejecta suggests that the ISM dust emission has been modelled accurately and supports the inference that the residual emission can be attributed to cold dust formed in Cas A. The drop in SN dust mass outside the reverse shock regions may be consistent with the destruction of part of the freshly formed dust in Cas A by the reverse shock (e.g. Nozawa et al. 2010). Comparing the average dust column densities inside and outside the reverse shock, we estimate the dust destruction efficiency of the reverse shock in Cas A to be
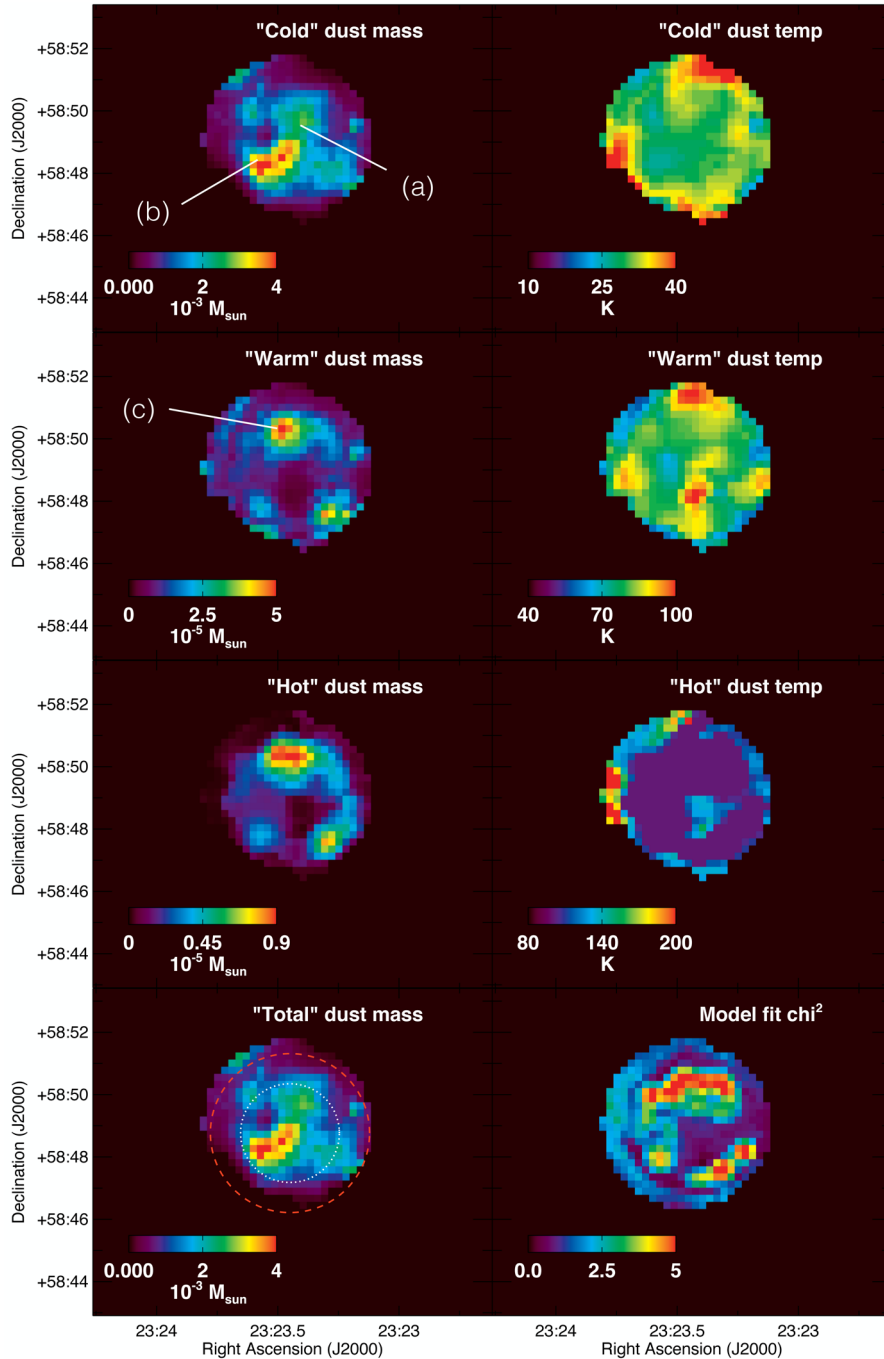
Figure 12. Dust mass maps (left) and temperature maps (right) for the hot, warm and cold SN dust components in Cas A. The bottom row shows the summed 'Total' dust mast map (left) and χ^2 map (right). The individual SEDs of the pixels indicated as (a), (b) and (c) in the dust mass maps are presented in Fig. 11. In the bottom left panel, the position of the forward and reverse shock are indicated as dashed red and dotted white circles, respectively.

$\sim$70 per cent.[23] The latter value is lower compared to the 80 per cent, 99 per cent and 88 per cent dust destruction efficien-

cies estimated for small silicate-type grains by Silvia, Smith & Shull (2010), Bocchio et al. (2016a) and Micelotta, Dwek & Slavin (2016), respectively.[24] Given the expected strong increase in heavy element abundances towards the inner regions of the SN ejecta and the consequent uncertainties on the geometrical distribution of SN

---

[23] To estimate the fraction of dust destroyed by the reverse shock, we assume that the ejecta are distributed homogeneously within a sphere confined by the forward shock. Based on this simple geometrical model, we can estimate the length of a column through the sphere's centre (306 arcsec = 2*R) and the extent of a sightline at the position of the reverse shock (240 arcsec), which is taken into account when comparing the dust column density inside and outside the reverse shock.

[24] The dust destruction efficiency based on the models presented in Bocchio et al. (2016a) was estimated by comparing their best-fitting dust mass (0.83 $M_{\odot}$) for the current epoch to the final dust mass that will be ejected into the ISM (1.07×10^{-2}) according to their models.

Table 4. The results of the spatially resolved SED fitting procedure for a variety of dust species. We present dust masses and temperatures for the hot (columns 2 and 3), warm (columns 4 and 5) and cold SN dust components (columns 6 and 7) for three different runs with ISRF scaling factors $G = 0.3$, 0.6 and 1.0 $G_\odot$, respectively. Columns 8 and 9 list the total dust mass (i.e. the sum of the hot, warm and cold dust masses) and the reduced χ^2 value that corresponds to the best-fitting SED model. The uncertainties on the SN dust masses correspond to the 1σ errors computed from the covariance matrix during the SED fitting based on the observational uncertainties of the flux in every waveband. Columns 10 and 11 present the lower limits on the SN dust temperature and mass. The lower limit on the total SN dust mass was calculated by scaling the ISM dust model to the extreme value of the SPIRE 500 μm flux density (i.e. $F_{500} + \sigma_{500}$) to maximize the contribution from ISM dust emission to the global SED in every pixel (i.e. leaving no room for an SN dust contribution at 500 μm). The dust temperature corresponds to the dust temperature of the coldest SN dust component obtained from this lower limit fit. The numbers in boldface correspond to the results from SED fitting for an ISM model with $G = 0.6\,G_0$ and an SN dust model with silicate-type grains ($MgSiO_3$, $Mg_{2.4}SiO_{4.4}$), and are believed to be representative of the SN dust conditions in Cas A.

Dust species	Hot dust Best fit		Warm dust Best fit		Cold dust Best fit		Total dust Best fit		Total dust Lower limit	
	T_d (K)	M_d ($10^{-3}\,M_\odot$)	T_d (K)	M_d ($10^{-2}\,M_\odot$)	T_d (K)	M_d ($M_\odot$)	M_d ($M_\odot$)	χ^2	T_d (K)	M_d (lower) ($M_\odot$)
$G = 0.3\,G_0$										
$MgSiO_3$	100 ± 23	0.9 ± 0.2	79 ± 9	0.6 ± 0.1	27 ± 3	1.4 ± 0.2	1.4 ± 0.2	1.40	31 ± 3	0.6 ± 0.1
$Mg_{0.7}SiO_{2.7}$	200 ± 0	0.03 ± 0.01	55 ± 2	35.4 ± 1.9	20 ± 1	49.3 ± 9.6	49.7 ± 9.6	3.90	26 ± 2	8.0 ± 1.2
$Mg_{2.4}SiO_{4.4}$	130 ± 41	0.4 ± 0.2	78 ± 10	0.8 ± 0.1	28 ± 4	0.9 ± 0.1	0.9 ± 0.1	1.71	33 ± 4	0.5 ± 0.1
Al_2O_3 (porous)	100 ± 11	1.3 ± 0.2	80 ± 8	0.5 ± 0.1	27 ± 4	0.5 ± 0.1	0.5 ± 0.1	1.56	34 ± 4	0.11 ± 0.02
$CaAl_{12}O_{19}$	100 ± 12	1.1 ± 0.1	78 ± 6	1.0 ± 0.1	16 ± 1	41.7 ± 5.0	41.7 ± 5.0	4.08	19 ± 2	5.6 ± 0.9
Am. carbon 'AC1'	100 ± 19	1.1 ± 0.2	94 ± 7	0.6 ± 0.1	28 ± 3	0.6 ± 0.1	0.6 ± 0.1	1.98	39 ± 2	0.08 ± 0.02
a-C ($E_g = 0.1$ eV)	100 ± 15	1.1 ± 0.2	87 ± 8	0.6 ± 0.1	27 ± 3	0.9 ± 0.1	0.9 ± 0.2	1.66	36 ± 3	0.2 ± 0.1
$G = 0.6\,G_0$										
$MgSiO_3$	**100 ± 17**	**0.9 ± 0.2**	**79 ± 10**	**0.6 ± 0.1**	**30 ± 4**	**0.5 ± 0.1**	**0.5 ± 0.1**	**1.76**	**38 ± 3**	**0.17 ± 0.02**
$Mg_{0.7}SiO_{2.7}$	200 ± 0	0.03 ± 0.01	56 ± 3	34.4 ± 1.9	21 ± 2	21.1 ± 9.2	21.4 ± 9.2	3.82	30 ± 7	1.9 ± 0.5
$Mg_{2.4}SiO_{4.4}$	**120 ± 40**	**0.4 ± 0.2**	**79 ± 11**	**0.9 ± 0.1**	**32 ± 5**	**0.3 ± 0.1**	**0.3 ± 0.1**	**1.74**	**39 ± 2**	**0.13 ± 0.02**
Al_2O_3 (porous)	100 ± 8	1.3 ± 0.2	80 ± 8	0.5 ± 0.1	30 ± 8	0.3 ± 0.2	0.3 ± 0.2	1.81	38 ± 3	0.03 ± 0.01
$CaAl_{12}O_{19}$	100 ± 7	1.1 ± 0.2	78 ± 6	0.9 ± 0.1	16 ± 2	30.6 ± 6.5	30.6 ± 6.5	4.02	22 ± 5	1.6 ± 0.5
Am. carbon 'AC1'	100 ± 17	1.1 ± 0.2	93 ± 8	0.6 ± 0.1	28 ± 6	0.5 ± 0.2	0.5 ± 0.2	1.82	38 ± 4	0.03 ± 0.01
a-C ($E_g = 0.1$ eV)	100 ± 12	1.2 ± 0.2	86 ± 9	0.7 ± 0.1	28 ± 7	0.6 ± 0.1	0.6 ± 0.2	1.82	39 ± 2	0.05 ± 0.01
$G = 1.0\,G_0$										
$MgSiO_3$	100 ± 16	1.0 ± 0.2	79 ± 11	0.7 ± 0.1	32 ± 13	0.20 ± 0.03	0.20 ± 0.03	2.05	39 ± 2	0.06 ± 0.01
$Mg_{0.7}SiO_{2.7}$	200 ± 0	0.03 ± 0.01	56 ± 2	32.0 ± 1.7	13 ± 8	5.6 ± 9.2	5.8 ± 6.5	3.78	35 ± 7	0.4 ± 0.1
$Mg_{2.4}SiO_{4.4}$	120 ± 38	0.4 ± 0.2	76 ± 10	1.0 ± 0.1	35 ± 18	0.11 ± 0.02	0.11 ± 0.02	1.80	39 ± 2	0.05 ± 0.01
Al_2O_3 (porous)	100 ± 10	1.3 ± 0.2	78 ± 7	0.5 ± 0.1	20 ± 12	0.4 ± 0.3	0.4 ± 0.3	1.92	37 ± 6	0.010 ± 0.002
$CaAl_{12}O_{19}$	100 ± 5	1.1 ± 0.2	78 ± 5	0.9 ± 0.1	15 ± 3	22.9 ± 6.1	22.9 ± 6.1	4.06	32 ± 9	0.3 ± 0.2
Am. carbon 'AC1'	100 ± 16	1.1 ± 0.2	92 ± 8	0.7 ± 0.1	23 ± 10	0.6 ± 0.3	0.6 ± 0.3	1.78	35 ± 7	0.010 ± 0.002
a-C ($E_g = 0.1$ eV)	100 ± 13	1.2 ± 0.2	84 ± 9	0.7 ± 0.1	23 ± 11	0.7 ± 0.2	0.7 ± 0.2	1.90	37 ± 6	0.02 ± 0.01

dust and dust mass surface densities interior/exterior to the reverse shock, we do not rule out that dust destruction efficiencies maybe higher or lower than 70 per cent. Based on a dust destruction efficiency of 70 per cent, and comparing the volumes of ejecta that have been affected by the reverse shock (76 per cent) and the ∼0.4–0.5 $M_\odot$ of dust interior to the reverse shock (24 per cent), we would estimate an initial dust mass up to 1.6–2.0 $M_\odot$, under the debatable assumption that the dust condensation occurred homogeneously throughout the entire sphere of ejecta.

While most of the cold SN dust is confined to the unshocked ejecta, there are concentrations of cold SN dust that extend beyond the reverse shock on opposite sides of the remnant. Even though not perfectly aligned with the relativistic jets, which have been shown to drive the outflow of fast moving knots (DeLaney et al. 2010), their location suggests that cold SN dust grains have been ejected along the north-east and south-west jets of Cas A. If so, it is interesting to note that the dust in the outflow along the jets is not destroyed with the same efficiency as elsewhere in the remnant. Either the grain composition might be different and less easily destroyed by the reverse shock, or the faster moving material along the jet is less prone to dust sputtering. The latter argument is supported by models of grain destruction in reverse shocks which show that the sputtering yield decreases with increasing energy for He atom/ion

inertial sputtering at velocities >200 km s^{-1} or equivalently $T_{gas} > 10^7$ K (e.g. Barlow 1978; Draine & Salpeter 1979a,b; Tielens et al. 1994; Nozawa, Kozasa & Habe 2006; Bocchio et al. 2016a).

5 DUST MASSES AND UNCERTAINTIES

5.1 SN dust masses and uncertainties

We derive SN dust masses of 0.5 $M_\odot$ for $MgSiO_3$ dust or 0.3 $M_\odot$ for $Mg_{2.4}SiO_{4.4}$ grains with a silicate-type dust composition. We can obtain similarly good SED fits with 0.5–0.6 $M_\odot$ of carbonaceous grains. Based on elemental yield predictions from nucleosynthesis models for type II and type IIb CCSN, we can rule out that Al_2O_3, $Mg_{0.7}SiO_{2.7}$ or $CaAl_{12}O_{19}$ grain species dominate the cold dust reservoir in Cas A. Although some carbon dust might form in specific ejecta layers (e.g. Sarangi & Cherchneff 2013), a dominant amorphous carbon dust component seems unlikely for this very oxygen-rich SNR. For the latter results, we have assumed an ISM model with $G = 0.6\,G_0$ which was independently constrained based on SED modelling of the ISM dust surrounding Cas A and PDR modelling of the interstellar [C I] and CO emission along the sightline of Cas A. In Appendix E2, we investigated what effect this assumption has on the modelled SN dust masses. We find

that a lower ISRF (or $G = 0.3\,G_0$) results in higher residual SN dust emission at IR–submm wavelengths and thus higher SN silicate dust masses (0.9–$1.4\,M_\odot$). In the same way, we derive lower SN dust fluxes and thus lower SN dust masses (0.1–$0.2\,M_\odot$) for silicate-type grains for a higher ISRF ($G = 1.0\,G_0$). Based on the estimated metal production by nucleosynthesis models up to $1.4\,M_\odot$ ($MgSiO_3$) or $0.9\,M_\odot$ ($Mg_{2.4}SiO_{4.4}$) for silicate-type grains,[25] the ISM models with $G = 0.3\,G_0$ would require all metals to be locked up into dust grains to fit the SED which is incompatible with the detection of metals in Cas A in the gas phase (e.g. Rho et al. 2008; Arendt et al. 2014). While our two independent methods favour the ISM model with $G = 0.6\,G_\odot$, we cannot rule out that the local ISRF near Cas A resembles the conditions in the solar neighbourhood ($G = 1.0\,G_\odot$) and $G = 0.6\,G_\odot$ merely represents the average ISRF along the line of sight to Cas A. In that case, the SN dust mass that is able to reproduce the SED would be lower and our models suggest the condensation of 0.2 or $0.1\,M_\odot$ of $MgSiO_3$ or $Mg_{2.4}SiO_{4.4}$ dust, respectively. In both cases, those values would be sufficient to account for the production of dust at high redshifts by SNe (if Cas A can be considered to be representative for the dust condensation efficiency in other SNRs).

5.2 Comparison with previous results for Cas A

Our preferred SN dust masses derived here for silicate-type grains (0.3–$0.5\,M_\odot$ with a lower limit of $M_d \geq 0.1$–$0.2\,M_0$) are larger than the dust masses previously derived from observational SED studies of Cas A ($<0.1\,M_\odot$, Rho et al. 2008; Barlow et al. 2010; Sibthorpe et al. 2010; Arendt et al. 2014), but consistent with the SN dust mass derived based on SCUBA $850\,\mu m$ polarimetric observations (Dunne et al. 2009; but see Section F2). The extension of our study to wavelengths longwards of $200\,\mu m$, where the cold dust component's emission peaks and the careful removal of the emission of other components have allowed us to measure cold dust emitting at temperatures of $T_d \sim 30\,K$ within Cas A. The mass of SN dust derived from our resolved study of *Spitzer* and *Herschel* observations is, furthermore, in agreement with the dust mass derived by fitting the nebular line profile asymmetries in the integrated spectra of Cas A using a Monte Carlo dust radiative transfer model ($\sim 1.1\,M_\odot$, Bevan et al. 2016). These values are also consistent with the dust condensation models of Bianchi & Schneider (2007) who predicted $\sim 0.6\,M_\odot$ of dust to form in the ejecta of SNe having progenitor masses between 22 and $30\,M_\odot$, but significantly higher compared to the dust evolution models in Nozawa et al. (2010), who predicted $0.08\,M_\odot$ of new grain material of which $0.072\,M_\odot$ was predicted to reside in the inner remnant regions unaffected by the reverse shock.

To understand the difference in the derived SN dust masses based on the newly reduced *Herschel* data set presented here and the analysis of Barlow et al. (2010, who find $0.075\,M_\odot$ of $T_d = 35\,K$ dust), we apply the same fitting technique to their PACS and SPIRE flux densities (after subtraction of their non-thermal emission model) using our multicomponent SN+ISM model. For an ISM model with ISRF of $G = 0.6\,G_0$ and an $Mg_{0.7}SiO_{2.7}$ and $MgSiO_3$ grain composition for the hot and warm+cold SN dust components, we derive a global SN dust mass of $0.23 \pm 0.06\,M_\odot$ with a dust temperature

of $T_d = 33\,K$ for the most massive, cold SN dust component. This newly derived dust mass is a factor of 3 higher compared to the dust mass at a similar temperature of $T_d \sim 35\,K$ derived by Barlow et al. (2010) based on the same set of photometry measurements. The dust mass absorption coefficient $\kappa_{160} = 12.7\,cm^2\,g^{-1}$ used in this paper is only a factor of 1.3 larger than $\kappa_{160} = 9.8\,cm^2\,g^{-1}$ in Barlow et al. (2010) and cannot explain the difference in SN dust masses. We therefore argue that the difference between the two studies can be attributed to the assumed model for the ISM emission, which dominates at wavelengths $\geq 160\,\mu m$ and strongly depends on the radiation field that illuminates the ISM dust (see Appendix E2).

5.3 Shock destruction of SN dust

Since most of the cold dust mass in Cas A appear to be located in the unshocked ejecta, the mass of dust that eventually will mix with the surrounding ISM material may decrease after the passage of the reserve shock. Based on a comparison of the dust mass surface density inside and outside the reverse shock and a simple geometrical model, we would estimate a dust destruction efficiency of ~ 70 per cent (see Section 4). Several theoretical models have also estimated the current dust mass content in Cas A and have modelled the dust evolution after the reverse shock has reached the centre of the remnant. In general, the sputtering rate for a grain depends on the pre-shock gas density, the magnetic field strength, shock velocity and the grain radius. For the reverse shock sputtering models of Nozawa et al. (2010), the largest grain radii considered were $<10^{-2}\,\mu m$, which were found to have lifetimes of 500–1000 yr. Grains of radius $a = 1\,\mu m$ would have lifetimes more than 100 times greater, longer than the time to cross the reverse shock. Using a set of hydrodynamical simulations, Silvia et al. (2010) calculated the grain sputtering efficiency for a variety of grain species and size distributions. Their simulations of planar reverse shocks impacting clumps of newly formed ejecta indicated that grains with radii $<0.1\,\mu m$ would be sputtered to smaller grain sizes and often completely destroyed, while larger grains would be able to survive the reverse shock due to less efficient coupling to the shocked gas which might leave them undisturbed after the passage of the reverse shock (e.g. Slavin, Jones & Tielens 2004). The destruction efficiency, furthermore, seems to depend on grain composition, with average destroyed fractions of 20, 38, 80 and 100 per cent grains for Fe, C, SiO_2 and Al_2O_3 grains (Silvia et al. 2010), respectively. Biscaro & Cherchneff (2016) found that non-thermal sputtering in dust clumps in Cas A plays an important role in dust destruction and predicted that it would reduce the current SN dust mass by 40–80 per cent. The largest grain radii that they considered for the Cas A case were $<0.02\,\mu m$. Micelotta et al. (2016) adopted an interstellar MRN (Mathis, Rumpl & Nordsieck 1977) power-law grain size distribution $n(a) \propto a^{-3.5}$ with $a_{min} = 0.005\,\mu m$ and $a_{max} = 0.25\,\mu m$ for Cas A, found that only the largest grains survived, with ~ 12 per cent and ~ 16 per cent of silicate and carbon grain mass surviving the passage of the reverse shock. Based on hydrodynamical simulations of the evolution of the remnant, Bocchio et al. (2016a) predict a current dust mass of $0.83\,M_\odot$ of Cas A, in good agreement with the dust masses derived from our observational study presented in this paper. Most of their modelled SN dust was made up of Mg_2SiO_4 grains ($0.4\,M_\odot$) with smaller contributions from SiO_2 ($0.16\,M_\odot$), Fe_3O_4 ($0.13\,M_\odot$), amorphous carbon ($0.12\,M_\odot$), Al_2O_3 ($2.14 \times 10^{-2}\,M_\odot$) and $MgSiO_3$ ($2.4 \times 10^{-5}\,M_\odot$) grains. According to their simulations, only $1.07 \times 10^{-2}\,M_\odot$ of dust (1.30 per cent of the current dust mass) would subsequently be able to survive the reverse shock. Their models treated

---

[25] These maximum dust masses correspond to an SN type II event with a $30\,M_\odot$ progenitor. Although dust masses are lower for a type IIb event with a $18\,M_\odot$ progenitor, we lack constraints on the element production in a type IIb event for a more massive progenitor.
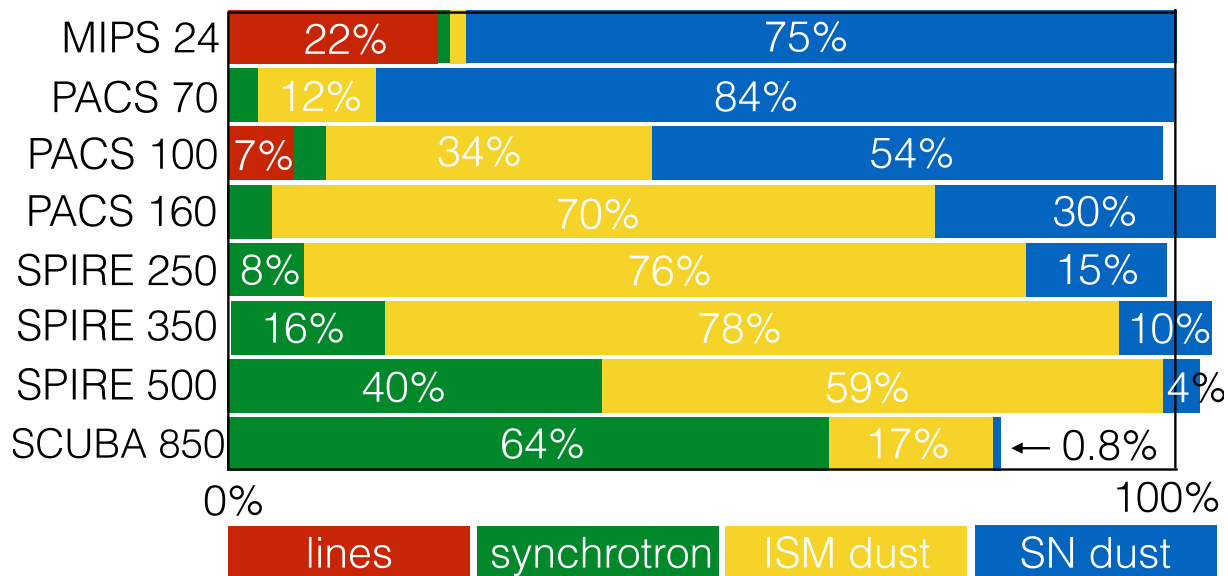
Figure 13. Schematic overview of the relative flux contributions of line, synchrotron, ISM and SN dust emission for Cas A in the MIPS 24 μm, PACS 70, 100 and 160 μm, and SPIRE 250, 350 and 500 μm and SCUBA 850 μm wavebands. The vertical black line on the right indicates the 100 per cent level. The emission of various components does not always perfectly add up to 100 per cent due to the flux uncertainties that have been taken into account in the SED fitting. The model deficit at 850 μm is discussed in Appendix F2.

grain size distributions with radii less than 0.01 μm, but they did find that grains of radius 0.1 μm would survive the passage of the reverse shock. While the above theoretical models predict different dust survival fraction, and adopted small grain radii typical of the ISM (while larger grains might be expected in SNRs), the conclusion from these studies is that somewhere between 1 and 80 per cent of the current dust mass in Cas A will be able to survive and be mixed with the ISM. In order to explain the high dust mass content in the early Universe, it would require that >20–30 per cent of the current SN-formed dust mass (0.3–0.5 M$_\odot$) survives passage through the SN reverse shock.

5.4 IR–submm emission components

By carefully determining the temperature and emission levels of the Galactic ISM foreground material, we have been able to model the ISM and SN dust emission at every wavelength based on a multicomponent SED fitting approach. In Appendix E1, we present a detailed comparison of our best-fitting model with observations, and conclude that our multicomponent ISM+SN model is adequate to reproduce the observed IR–submm emission towards Cas A within the uncertainties. While our model is consistent with the observational IR–submm constraints up to 500 μm, our best-fitting combined model of all emission components has a flux deficit of 9.5 Jy at 850 μm (although within the limits of the 850 μm uncertainties). In Appendix F2, we present a detailed comparison between the predicted 850 μm model flux of various components (synchrotron, ISM and SN dust emission) and observations presented by Dunne et al. (2003) and Dunne et al. (2009). We show that the 850 μm deficit can be accounted for using a more shallow synchrotron spectrum ($\alpha = -0.54$) without significantly affecting the synchrotron contribution at wavelengths $\lambda \leq 500$ μm and thus the resulting SN dust masses determined from SED fitting. We, furthermore, show that the emission of ISM dust (8.6 Jy) and SN dust (0.4 Jy) in our model at 850 μm is difficult to reconcile with the high degree of polarization

attributed to SN dust by Dunne et al. (2009), which would require an SN dust flux at 850 μm of at least 6 Jy.

Fig. 13 provides a schematic overview of the contributions of the different components to the total IR/submm emission for Cas A based on models constructed for each of these components. With SN dust contributions of only 15 per cent, 10 per cent and 4 per cent to the SPIRE 250, 350 and 500 μm wavebands, respectively, an accurate determination of the SN dust mass in Cas A requires reliable models for the emission of other components contributing at those wavelengths. The contribution of various emission components at IR–submm wavelengths is discussed in more detail in Appendix F1.

The ISM and SN dust mass maps derived from the multicomponent SED modelling can furthermore be used to derive interstellar and SN visual extinction maps (see Appendix F3). The high column densities of interstellar material significantly attenuate the lines of sight towards Cas A with an average A_V of 6–8 mag and peaks up to 15 mag. The condensation of elements in the central regions of Cas A provides an additional visual extinction of up to $A_V = 1.5$. The combined attenuation by ISM and SN dust makes it very difficult to detect the SNR and a possible binary companion at optical wavelengths but near-IR imaging could be more effective.

6 CONCLUSIONS

We have combined *Spitzer* IRAC, MIPS and IRS, *WISE*, *Planck*, and *Herschel* PACS and SPIRE data sets to study the spatial distribution of SN dust produced in Cas A at a resolution of 0.6 pc in order to determine the overall mass of freshly formed dust in Cas A. By extending our analysis to submm wavelengths, we are able to probe the coldest dust grains that have condensed in the ejecta of Cas A. Due to the high degree of ISM contamination at longer wavelengths, we require a careful removal of the emission of foreground and background interstellar material and other contaminants (line emission and synchrotron radiation). We have constructed physically motivated models to subtract the line

emission and synchrotron radiation from these IR/submm images. More specifically, we

(i) used *Spitzer* IRS, *Herschel* PACS IFU and SPIRE FTS spectra to carefully estimate and remove contaminating emission from bright lines (mainly [Ar III] 8.99 μm and [O III] 88 μm) from the broad-band images,

(ii) updated the spectral index of the synchrotron spectrum based on exquisitely calibrated *Planck* mm-wave data, and extrapolated the synchrotron radiation to IR/submm wavelengths by normalizing the integrated *Planck* fluxes to a 3.7 mm Very Large Array (VLA) image,

(iii) applied the THEMIS dust model (Jones et al. 2013; Köhler et al. 2014) that has been calibrated based on observations of dust extinction and emission in the Milky Way, to model the emission of foreground and background interstellar dust. This ISM dust model was scaled relative to the SPIRE 500 μm flux after subtraction of the synchrotron component. The scaling of the radiation field ($G = 0.6\, G_0$) that illuminates the ISM dust was constrained through the modelling of the ISM dust SEDs in the surroundings of Cas A. A similar scaling factor, $G = 0.6^{+0.4}_{-0.3}\, G_0$, was retrieved through PDR modelling based on the [C I] $1-0$, $2-1$ and CO $4-3$ line emission originating from ISM material in the line of sight to Cas A (Appendix C).

After subtraction of line emission and synchrotron radiation components, we fitted the $17-500$ μm SED with a multicomponent ISM+SN dust model. We required three SN dust components (hot, warm and cold) to reproduce the multiwaveband emission. The hot dust component was assumed to be composed of silicates with a low Mg/Si ratio, $Mg_{0.7}SiO_{2.7}$, following Rho et al. (2008) and Arendt et al. (2014) in order to model the emission peak at 21 μm. We ran different sets of SED models with varying dust composition ($MgSiO_3$, $Mg_{2.4}SiO_{4.4}$, $Mg_{0.7}SiO_{2.7}$, Al_2O_3, $CaAl_{12}O_{19}$ and various types of amorphous carbon) for the warm and cold SN dust components. We find that

(i) the best-fitting models suggest that 0.5 $M_\odot$ of $MgSiO_3$ grains or 0.3 $M_\odot$ of $Mg_{2.4}SiO_{4.4}$ grains are present in Cas A, with an average cold dust temperature $T_d \sim 30$ K;

(ii) strict lower limits of 0.1–0.2 $M_\odot$ on the cold SN dust mass are derived by assuming a higher scaling factor for the ISRF ($G = 1.0\, G_0$) heating the ISM dust;

(iii) the multiwavelength emission of Cas A can also be fitted by 0.5–0.6 $M_\odot$ of carbon grains, even though silicates are expected to dominate the dust composition in the O-rich remnant Cas A;

(iv) a total SN dust mass between 0.4 and 0.6 $M_\odot$ is required to reproduce the dust continuum observations assuming a mixture of 50 per cent of silicate-type grains and 50 per cent of carbonaceous grains;

(v) from the amounts required to match the observed SED, we can exclude $Mg_{0.7}SiO_{2.7}$, $CaAl_{12}O_{19}$ and Al_2O_3 as dominant dust species based on the elemental yields predicted for a CCSN with a 30 $M_\odot$ progenitor;

(vi) the cold SN dust component is mainly distributed interior to the reverse shock of Cas A, suggesting that some part of the newly formed dust has been destroyed by the reverse shock;

(vii) the drop in dust mass behind the reverse shock implies that $\sim$70 per cent by mass of the dust is destroyed as it passes through the reverse shock in Cas A;

(viii) the ISM model predicts an average interstellar extinction of $A_V = 6-8$ mag with maximum values of $A_V = 15$ mag towards Cas A.

Based on our revised dust mass of 0.3–0.5 $M_\odot$ for silicate-type dust in Cas A,[26] we conclude that, if produced by other remnants, this dust mass is sufficient to explain the large dust masses observed in dusty star-forming galaxies at high redshifts, if a non-negligible part of the initially condensed dust reservoir ($\geq$20–30 per cent) is capable of surviving the reverse shock.

REFERENCES

Anderson M. C., Rudnick L., 1996, ApJ, 456, 234
Andrews J. E. et al., 2016, MNRAS, 457, 3241

[26] The latter SN dust masses result from our SED modelling procedure using the latest ISM models and IR/submm dust emissivities derived from the most recent set of laboratory studies to date. The characterization of dust optical properties and ISM dust composition is a dynamic area of research and the SN dust masses published in this work may need to be updated to account for any changes in ISM and SN dust models in the foreseeable future.

Aniano G., Draine B. T., Gordon K. D., Sandstrom K., 2011, PASP, 123, 1218

Arendt R. G., 1989, ApJS, 70, 181

Arendt R. G., Dwek E., Moseley S. H., 1999, ApJ, 521, 234

Arendt R. G., Dwek E., Kober G., Rho J., Hwang U., 2014, ApJ, 786, 55

Balog Z. et al., 2014, Exp. Astron., 37, 129

Barlow M. J., 1978, MNRAS, 183, 367

Barlow M. J. et al., 2010, A&A, 518, L138

Begemann B., Dorschner J., Henning T., Mutschke H., Gürtler J., Kömpe C., Nass R., 1997, ApJ, 476, 199

Bendo G. J. et al., 2013, MNRAS, 433, 3062

Bersanelli M. et al., 2010, A&A, 520, A4

Bertoldi F., Carilli C. L., Cox P., Fan X., Strauss M. A., Beelen A., Omont A., Zylka R., 2003, A&A, 406, L55

Bevan A., Barlow M. J., 2016, MNRAS, 456, 1269

Bevan A., Barlow M. J., Milisavljevic D., 2016, preprint (arXiv:1611.05006)

Bianchi S., Schneider R., 2007, MNRAS, 378, 973

Biscaro C., Cherchneff I., 2016, A&A, 589, A132

Bocchio M., Marassi S., Schneider R., Bianchi S., Limongi M., Chieffi A., 2016a, A&A, 587, A157

Bocchio M., Bianchi S., Abergel A., 2016b, A&A, 591, A117

Braun R., 1987, A&A, 171, 233

Chevalier R. A., Kirshner R. P., 1979, ApJ, 233, 154

Chevalier R. A., Oishi J., 2003, ApJ, 593, L23

Compiègne M. et al., 2011, A&A, 525, A103

DeLaney T. et al., 2010, ApJ, 725, 2038

DeLaney T., Kassim N. E., Rudnick L., Perley R. A., 2014, ApJ, 785, 7

Docenko D., Sunyaev R. A., 2010, A&A, 509, A59

Dorschner J., Begemann B., Henning T., Jaeger C., Mutschke H., 1995, A&A, 300, 503

Douvion T., Lagage P. O., Pantin E., 2001, A&A, 369, 589

Draine B. T., 1978, ApJS, 36, 595

Draine B. T., Salpeter E. E., 1979a, ApJ, 231, 77

Draine B. T., Salpeter E. E., 1979b, ApJ, 231, 438

Dunne L., Eales S., Ivison R., Morgan H., Edmunds M., 2003, Nature, 424, 285

Dunne L. et al., 2009, MNRAS, 394, 1307

Dwek E., Hauser M. G., Dinerstein H. L., Gillett F. C., Rice W. L., 1987, ApJ, 315, 571

Dwek E., Galliano F., Jones A. P., 2007, ApJ, 662, 927

Engelbracht C. W. et al., 2007, PASP, 119, 994

Ennis J. A., Rudnick L., Reach W. T., Smith J. D., Rho J., DeLaney T., Gomez H., Kozasa T., 2006, ApJ, 652, 376

Eriksen K. A., Arnett D., McCarthy D. W., Young P., 2009, ApJ, 697, 29

Fabbri J. et al., 2011, MNRAS, 418, 1285

Fazio G. G. et al., 2004, ApJS, 154, 10

Fesen R. A., 2001, ApJS, 133, 161

Fesen R. A., Morse J. A., Chevalier R. A., Borkowski K. J., Gerardy C. L., Lawrence S. S., van den Bergh S., 2001, AJ, 122, 2644

Fesen R. A. et al., 2006, ApJ, 645, 283

Gall C. et al., 2014, Nature, 511, 326

Gomez H. L. et al., 2012, ApJ, 760, 96

Gotthelf E. V., Koralesky B., Rudnick L., Jones T. W., Hwang U., Petre R., 2001, ApJ, 552, L39

Griffin M. J. et al., 2010, A&A, 518, L3

Groenewegen M. A. T. et al., 2011, A&A, 526, A162

Habing H. J., 1968, Bull. Astron. Inst. Neth., 19, 421

Hammer N. J., Janka H.-T., Müller E., 2010, ApJ, 714, 1371

Hines D. C. et al., 2004, ApJS, 154, 290

Houck J. R. et al., 2004, in Mather J. C., ed., Proc. SPIEConf. Ser. Vol. 5487, Optical, Infrared, and Millimeter Space Telescopes. SPIE, Bellingham, p. 62

Hurford A. P., Fesen R. A., 1996, ApJ, 469, 246

Indebetouw R. et al., 2014, ApJ, 782, L2

Jäger C., Dorschner J., Mutschke H., Posch T., Henning T., 2003, A&A, 408, 193

Jarrett T. H. et al., 2013, AJ, 145, 6

Jones A. P., 2012a, A&A, 540, A1

Jones A. P., 2012b, A&A, 540, A2

Jones A. P., 2012c, A&A, 542, A98

Jones A. P., Fanciullo L., Köhler M., Verstraete L., Guillet V., Bocchio M., Ysard N., 2013, A&A, 558, A62

Kennicutt R. C., Jr, et al., 2003, PASP, 115, 928

Kifonidis K., Müller E., Plewa T., 2001, Nucl. Phys. A, 688, 168

Kilpatrick C. D., Bieging J. H., Rieke G. H., 2014, ApJ, 796, 144

Köhler M., Jones A., Ysard N., 2014, A&A, 565, L9

Kotak R. et al., 2009, ApJ, 704, 306

Kozasa T., Hasegawa H., Nomoto K., 1991, A&A, 249, 474

Krause O., Birkmann S. M., Rieke G. H., Lemke D., Klaas U., Hines D. C., Gordon Karl D., 2004, Nature, 432, 596

Krause O., Birkmann S. M., Usuda T., Hattori T., Goto M., Rieke G. H., Misselt K. A., 2008, Science, 320, 1195

Lamarre J.-M. et al., 2010, A&A, 520, A9

Laming J. M., Hwang U., 2003, ApJ, 597, 347

Makiwa G., Naylor D. A., Ferlet M., Salji C., Swinyard B., Polehampton E., van der Wiel M. H. D., 2013, Appl. Opt., 52, 3864

Mathis J. S., Rumpl W., Nordsieck K. H., 1977, ApJ, 217, 425

Mathis J. S., Mezger P. G., Panagia N., 1983, A&A, 128, 212

Matsuura M. et al., 2011, Science, 333, 1258

Matsuura M. et al., 2015, ApJ, 800, 50

Meikle W. P. S. et al., 2007, ApJ, 665, 608

Micelotta E. R., Dwek E., Slavin J. D., 2016, A&A, 590, A65

Mie G., 1908, Ann. Phys., Lpz., 330, 377

Milisavljevic D., Fesen R. A., 2015, Science, 347, 526

Mookerjea B., Kantharia N. G., Roshi D. A., Masur M., 2006, MNRAS, 371, 761

Morgan H. L., Edmunds M. G., 2003, MNRAS, 343, 427

Mutschke H., Posch T., Fabian D., Dorschner J., 2002, A&A, 392, 1047

Naylor D. A. et al., 2014, in Oschmann J. M., Jr, Clampin M., Fazio G. G., MacEwen H. A., eds, Proc. SPIEConf. Ser. Vol. 9143, Space Telescopes and Instrumentation 2014: Optical, Infrared, and Millimeter Wave. SPIE, Bellingham, p. 91432D

Nozawa T., Kozasa T., Habe A., 2006, ApJ, 648, 435

Nozawa T., Kozasa T., Tominaga N., Maeda K., Umeda H., Nomoto K., Krause O., 2010, ApJ, 713, 356

Onić D., Urošević D., 2015, ApJ, 805, 119

Orlando S., Miceli M., Pumo M. L., Bocchino F., 2016, ApJ, 822, 22

Ott S., 2010, in Mizumoto Y., Morita K.-I., Ohishi M, eds, ASP Conf. Ser. Vol. 434, Astronomical Data Analysis Software and Systems XIX. Astron. Soc. Pac., San Francisco, p. 139

Owen P. J., 2015, PhD thesis, University College London

Owen P. J., Barlow M. J., 2015, ApJ, 801, 141

Papadopoulos P. P., Thi W.-F., Viti S., 2004, MNRAS, 351, 147

Paradis D., Dobashi K., Shimoikura T., Kawamura A., Onishi T., Fukui Y., Bernard J.-P., 2012, A&A, 543, A103

Pavlov G. G., Zavlin V. E., Aschenbach B., Trümper J., Sanwal D., 2000, ApJ, 531, L53

Pérez-Rendón B., García-Segura G., Langer N., 2002, Rev. Mex. Astron. Astrofís., 12, 94

Pérez-Rendón B., García-Segura G., Langer N., 2009, A&A, 506, 1249

Pilbratt G. L. et al., 2010, A&A, 518, L1

Planck Collaboration I, 2011, A&A, 536, A1

Planck Collaboration XXVI, 2016, A&A, 594, A26

Planck Collaboration XXXI, 2016, A&A, 586, A134

Planck Collaboration XLIV, 2016, A&A, preprint (arXiv:1604.01029)

Poglitsch A. et al., 2010, A&A, 518, L2

Pound M. W., Wolfire M. G., 2008, in Argyle R. W., Bunclark P. S., Lewis J. R., eds, ASP Conf. Ser. Vol. 394, Astronomical Data Analysis Software and Systems XVII, Astron. Soc. Pac., San Francisco, p. 654

Priddey R. S., Isaak K. G., McMahon R. G., Robson E. I., Pearson C. P., 2003, MNRAS, 344, L74

Reed J. E., Hester J. J., Fabian A. C., Winkler P. F., 1995, ApJ, 440, 706

Reynoso E. M., Goss W. M., 2002, ApJ, 575, 871

Rho J., Reynolds S. P., Reach W. T., Jarrett T. H., Allen G. E., Wilson J. C., 2003, ApJ, 592, 299

Rho J. et al., 2008, ApJ, 673, 271

Rieke G. H. et al., 2004, ApJS, 154, 25

Rouleau F., Martin P. G., 1991, ApJ, 377, 526

Rowlands K., Gomez H. L., Dunne L., Aragón-Salamanca A., Dye S., Maddox S., da Cunha E., van der Werf P., 2014, MNRAS, 441, 1040

Sarangi A., Cherchneff I., 2013, ApJ, 776, 107

Sibthorpe B. et al., 2010, ApJ, 719, 1553

Silvia D. W., Smith B. D., Shull J. M., 2010, ApJ, 715, 1575

Slavin J. D., Jones A. P., Tielens A. G. G. M., 2004, ApJ, 614, 796

Smith J. D. T. et al., 2007, PASP, 119, 1133

Sugerman B. E. K. et al., 2006, Science, 313, 196

Swinyard B. M. et al., 2010, A&A, 518, L4

Swinyard B. M. et al., 2014, MNRAS, 440, 3658

Tielens A. G. G. M., 2005, The Physics and Chemistry of the Interstellar Medium. Cambridge Univ. Press, Cambridge

Tielens A. G. G. M., McKee C. F., Seab C. G., Hollenbach D. J., 1994, ApJ, 431, 321

Todini P., Ferrara A., 2001, MNRAS, 325, 726

Vinyaikin E. N., 2014, Astron. Rep., 58, 626

Wallström S. H. J. et al., 2013, A&A, 558, L2

Watson D., Christensen L., Knudsen K. K., Richard J., Gallazzi A., Michałowski M J., 2015, Nature, 519, 327

Werner M. W. et al., 2004, ApJS, 154, 1

Wesson R., Barlow M. J., Matsuura M., Ercolano B., 2015, MNRAS, 446, 2089

Willingale R., Bleeker J. A. M., van der Heyden K. J., Kaastra J. S., Vink J., 2002, A&A, 381, 1039

Willingale R., Bleeker J. A. M., van der Heyden K. J., Kaastra J. S., 2003, A&A, 398, 1021

Woosley S. E., Weaver T. A., 1995, ApJS, 101, 181

Wright M., Dickel J., Koralesky B., Rudnick L., 1999, ApJ, 518, 284

Wright E. L. et al., 2010, AJ, 140, 1868-1881

Young P. A. et al., 2006, ApJ, 640, 891

APPENDIX A: *Planck* FLUX MEASUREMENTS

In this section, we compare various *Planck* measurements and explain why we opted to use the customized aperture photometry results from Planck Collaboration XXXI (2016). The Second *Planck* Catalogue of Compact Sources (PCCS2; Planck Collaboration XXVI 2016) reports four different flux measurements for Cas A (see Table A1) based on different source extraction techniques. The DETFLUX relies on the assumption of a point-like source, and filters out any extended emission. The other flux measurements are determined from the all-sky maps at the known position of Cas A. The APERFLUX corresponds to the flux measurement within

a circular aperture centred at the position of the source, with radius equal to the FWHM of the effective beam at that frequency. The PSFFLUX is derived by fitting a PSF model to the flux observed at the source position. The GAUFLUX is obtained by fitting a two-dimensional Gaussian model with variable amplitude, size and shape to the emission at the source position. The PCCS2 catalogue reports the fluxes for the LFI filters, while the HFI fluxes are retrieved from the PCCS2E catalogue (Planck Collaboration XXVI 2016). The latter catalogue does not contain a flux measurement for Cas A at 857 GHz, which is not surprising given the high degree of confusion with ISM dust at that frequency.

While the different flux measurements for the low-frequency filters are compatible, we find huge variations between the different flux extraction techniques at higher frequencies ($\nu \geq 100$ GHz). The GAUFLUX measurement at 545 GHz is several times higher compared to the other flux measurements, which can be attributed to a larger estimated source size due to the dominant contribution of interstellar dust emission, which has a more extended morphology compared to Cas A at those wavelengths. The DETFLUX measurements underestimate the fluxes because of the better resolution in those bands which starts to resolve the emission of Cas A and, thus, misses some of the flux due to its point source assumption. Based on a comparison of the various *Planck* fluxes with published fluxes at 87 GHz (96.7 Jy, Wright et al. 1999), 353 GHz (50.8 Jy, Dunne et al. 2003) and our *Herschel* SPIRE 500 μm flux density (59.2 Jy, see Table 2), we conclude that the different flux measurements from the PCCS2 catalogue all underestimate the fluxes at higher frequencies, where Cas A starts to be resolved with respect to the *Planck* beam. We therefore use the customized flux measurements from Planck Collaboration XXXI (2016) where the source size and beam size were considered in order to optimize the extraction area for aperture photometry (see Table A1, last row). Their flux uncertainties only account for observational uncertainties, while the measurements are undoubtedly affected by the chosen aperture for source extraction and background measurement. After experimenting with different source apertures and background regions in the *Herschel* maps, we assume more conservative uncertainties on the *Planck* photometry measurements which are a factor of 2 higher than reported by Planck Collaboration XXXI (2016).

APPENDIX B: LINE EMISSION

Several of the continuum bands contain a substantial contribution from bright emission lines contributing to the radiative cooling

Table A1. Overview of the different flux measurements F_ν in units of Jy for Cas A from the Second *Planck* Catalogue of Compact Sources (PCCS2). The FWHM of the *Planck* beam in the different LFI and HFI filters is reported in the second row. The last row presents the fluxes reported by Planck Collaboration XXXI (2016), that were extracted within an aperture optimized to the intrinsic source size and *Planck* beam at every frequency. Planck Collaboration XXXI (2016) does not report any flux measurement at 545 GHz due to the high level of confusion with the ISM dust emission. The uncertainties are the original errors reported by Planck Collaboration XXXI (2016), while we assume uncertainties that are a factor of 2 larger due to the dependence of the flux measurement on the choice of the aperture for source extraction and background determination.

| Flux type	F_{545}	F_{353}	F_{217}	F_{143}	F_{100}	F_{70}	F_{44}	F_{30}
FWHM (arcmin)	5.0	5.0	5.5	7.1	10	14	24	33
DETFLUX	23.7 ± 1.8	25.2 ± 0.6	32.6 ± 0.4	48.2 ± 0.4	72.1 ± 0.6	100.0 ± 0.2	135.2 ± 0.4	182.2 ± 0.5
APERFLUX	50.6 ± 20.6	40.5 ± 6.1	46.7 ± 2.2	61.8 ± 0.8	81.0 ± 0.7	105.0 ± 0.6	141.5 ± 1.9	189.5 ± 2.1
PSFFLUX	55.3 ± 32.4	40.9 ± 10.7	42.7 ± 3.6	57.3 ± 1.5	77.7 ± 0.6	100.6 ± 1.1	138.3 ± 1.9	188.6 ± 2.3
GAUFLUX	129.0 ± 0.9	38.0 ± 4.9	45.4 ± 2.6	60.2 ± 2.5	79.1 ± 2.9	97.9 ± 0.3	133.6 ± 0.3	189.5 ± 0.4
Planck XXXI 2016	–	**52 ± 7**	**62 ± 4**	**73 ± 4**	**94 ± 5**	**109 ± 6**	**140 ± 7**	**228 ± 11**
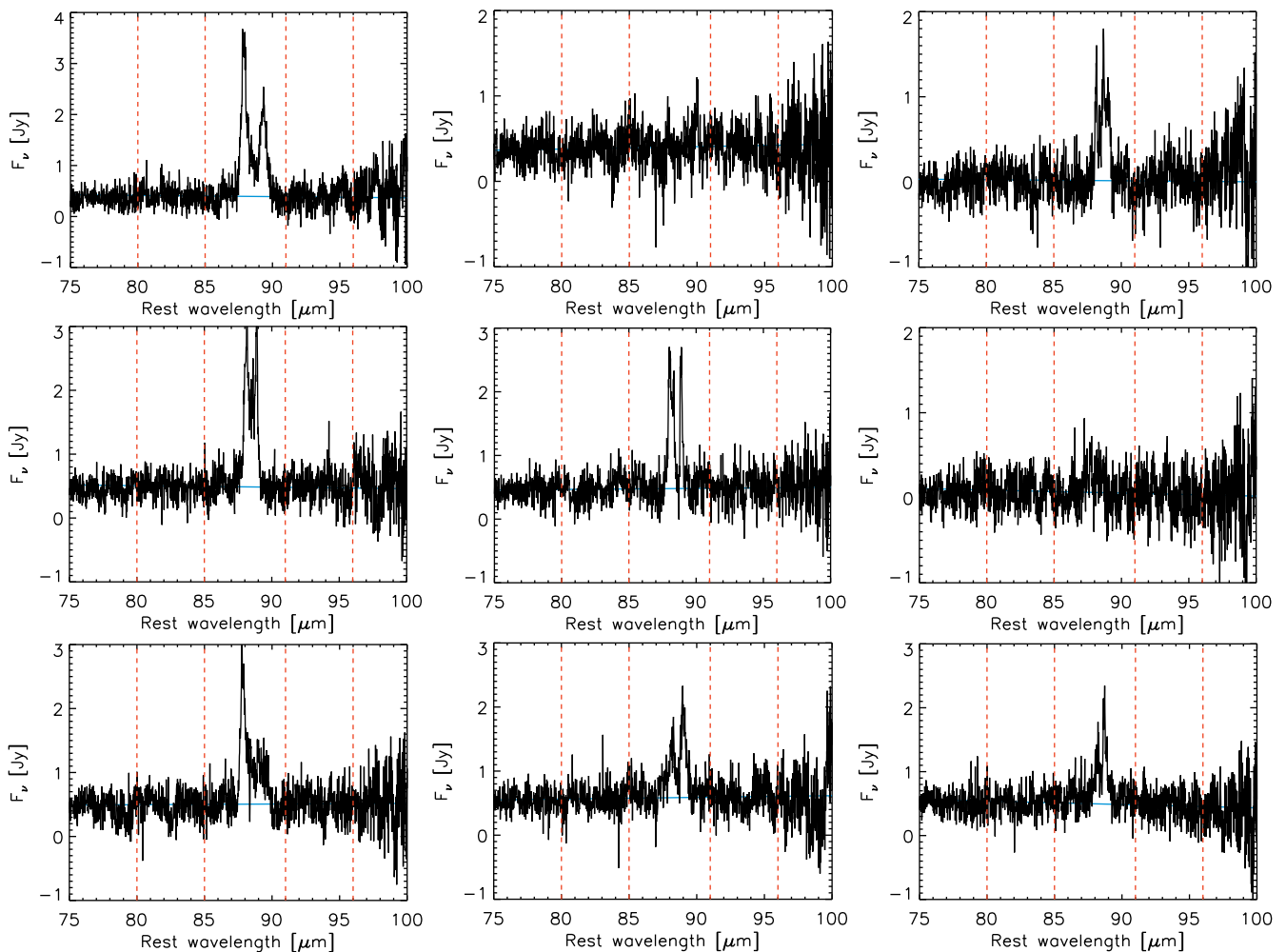
Figure B1. The [O III] 88 μm line spectra for the nine different pointings observed with the PACS IFU mode. The black line represents the observed spectrum, while the red dashed lines indicate the wavelength ranges on each side of the line profile that are used to fit the continuum. The solid blue lines represent the best fit to the continuum level.

budget of the SNR. We used the *Spitzer* IRS spectra, PACS IFU spectra and SPIRE FTS spectra to determine the contribution of line emission to the IRAC, *WISE*, PACS and SPIRE photometric wavebands.

In the IRAC 8 μm and *WISE* 12 μm bands, there are potential contributions from the [Ar II] 6.9 μm, [Ar III] 8.99 μm, [S IV] 10.51 μm, [Ne II] 12.81 μm and [Ne III] 15.56 μm nebular lines, while the *WISE* 22 μm and MIPS 24 μm bands include possible emission from the [S III] 18.71 μm, [Fe III] 22.93 μm, [O IV] 25.89 μm and [Fe II] 25.99 μm lines. The *Spitzer* IRS spectra were used to estimate the contribution of these nebular lines in Cas A. To derive line emission maps, we fitted the continuum with a first-order polynomial, subtracted it from each of the line channels and integrated over the continuum-subtracted SED to determine the line flux in every pixel. After fitting the line emission maps, we convolved the line maps from their original resolution to the SPIRE 500 μm FWHM resolution of ∼36.3 arcsec. Taking into account the transmission of the IRAC 8 μm, *WISE* 12 and 22 μm and MIPS 24 μm at the wavelengths of these lines, we derived non-negligible contributions from the [Ar II] and [Ar III] lines to the IRAC 8 μm image (41.6 per cent) and from the [S IV] and [Ne II] lines to the *WISE* 12 μm image (17.0 per cent). The latter values are consistent with the line con-

tributions of 28 per cent and 18 per cent to the 8.28 and 12 μm MSX bands estimated by Hines et al. (2004). The [O IV] 25.89 μm and [Fe II] 25.99 μm lines contribute 1.3 per cent and 22.1 per cent of the remnant's emission in the *WISE* 22 μm and MIPS 24 μm images, respectively.

The PACS IFU spectrometer observed the four wavelength ranges 51–72, 70–105, 102–146 and 140–210 μm at each of the nine targeted positions in Cas A (see Fig. 2). At each position, the four individual spectra were combined to a single spectrum by scaling them to match the fluxes in the overlapping wavelength ranges. To determine the [O I] 63 μm, [O III] 88 μm, [O I] 145 μm and [C II] 158 μm line fluxes, we fitted the continuum with a first degree polynomial, subtracted the continuum and summed the flux under the line profile. Fig. B1 shows the [O III] 88 μm line profiles for each of the nine targeted fields. We did not use Gaussian models to fit the line emission since the lines are often very irregular and separated into blueshifted and redshifted components. By comparing the line fluxes to the PACS broad-band fluxes within the same regions (taking into account the transmission of the PACS filters at the central wavelengths of these lines), we were able to derive the contribution of the different lines to the PACS broad-band maps. The contribution of the [O III] 88 μm line to the PACS 70 μm image is usually

1 per cent or lower, and so is within the limits of the photometric uncertainties in this waveband. Similarly, the contributions of the [O I] 63 μm and [C II] 158 μm lines to the PACS 70 and 160 μm wavebands, respectively, are less than 1 per cent and thus within the few per cent photometric uncertainty. The [O III] 88 μm line contribution to the PACS 100 μm waveband is more significant, with 2.7 per cent to 5.3 per cent of the PACS 100 μm emission attributable to line cooling from ionized gas. The largest contribution (5.3 per cent) comes from the central regions of Cas A, in the area internal to the reverse shock, with the second highest contributions (4–5 per cent) in the shocked ejecta in the south. Since we do not have a full map of the [O III] 88 μm line emission to correct the PACS 100 μm map for line contamination, we use the [Si II] 34.82 μm line map derived from the *Spitzer* IRS spectra. Even though the ionization potential (IP) of S^{++} (34.79 eV) more closely resembles the IP of O^+ (35.12 eV), the critical density (for collisions with electrons) of the [S IV] 10.51 μm line ($n_{crit} = 5 \times 10^4$ cm^{-3}) is two orders of magnitude higher compared to the critical density for [O III]. The [S IV] 10.51 μm line emission in Cas A is also significantly weaker than the [Si II] 34.82 μm line.

With an IP of 8.15 eV to produce Si^+, the [Si II] line can trace both the neutral and ionized gas phase. Because the gas in Cas A can be ionized due to shocks and/or the radiation field, we assume that most of the [Si II] emission comes from the ionized gas phase. The latter assumption is supported by the absence of any detected [O I] 63 or 145 μm line emission from Cas A (Docenko & Sunyaev 2010; Owen 2015). With a critical density of 10^3 cm^{-3} for collisions with electrons, and an excitation temperature for the upper level of 413 K, the [Si II] line is thought to trace a gas reservoir similar to the [O III] 88 μm line with a critical density $n_{crit} = 5 \times 10^2$ cm^{-3} and excitation temperature of 163 K. We scale the [Si II] map to the [O III] line contribution of 16 Jy at PACS 100 μm determined from the *ISO* LWS data for Cas A (covering most of the nebula) by Barlow et al. (2010), and subtracted it from the PACS 100 μm map. We do not apply any corrections to other wavebands because the [O I] 63 μm and [C II] 158 μm line contributions are small and within the photometric waveband uncertainties.

We inspected the SPIRE FTS spectra to see whether there is a possible contribution from the CO(10−9) 260.4 μm, CO(8−7) 325.5 μm and CO(5−4) 520.6 μm lines to the SPIRE 250, 350 and 500 μm wavebands, respectively, but do not find a line contribution that could be considered to be significant compared to the photometric uncertainties.

APPENDIX C: CHARACTERIZATION OF THE ISRF USING SUBMM EMISSION LINES

In Section 3.2, we have analysed the variation of the ISRF scaling factor, G, in regions that are dominated by ISM dust emission surrounding Cas A. Here, we present an alternative method to derive the strength of the UV radiation field along the line of sight to Cas A. Specifically, we relied on the observed submm line emission to constrain the parameters of suitable PDR models. Several submm lines are observed with the SPIRE FTS spectrometer, but we focus here on the CO(4−3), [C I] $^3P_2 \rightarrow {}^3P_1$ and [C I] $^3P_1 \rightarrow {}^3P_0$ lines at 461, 809 and 492 GHz, respectively, which are all tracers of the molecular gas in the ISM. Table C1 provides an overview of the line parameters (line frequency and detector FWHM, the energy of the upper level and its critical density). Due to the high critical density of the CO(4−3) line transition (see Table C1), the [C I] 492/CO(4−3) line ratio is a good tracer of the density of the interstellar gas (see Fig. C1, left-hand panel). With similar critical

Table C1. Characteristics of the lines used to constrain PDR parameters along the line of sight to Cas A. Columns 2 and 3 specify the line rest frequency and the FWHM of the SPIRE FTS bolometer beams at those frequencies. The energy of the upper state and their critical densities (as calculated by Papadopoulos, Thi & Viti 2004) are presented in columns 4 and 5.

Line	Frequency (GHz)	FWHM (arcsec)	E_{upper}/k (K)	n_{crit} (cm^{-3})
CO(4−3)	461.041	41.7	55	2×10^4
[C I] $^3P_2 \rightarrow {}^3P_1$	809.342	38.1	62.4	10^3
[C I] $^3P_1 \rightarrow {}^3P_0$	492.161	33.0	23.6	500

densities for both of the [C I] lines, the [C I] 809/[C I] 492 line ratio is a diagnostic of the ISRF scaling factor, via their temperature dependence at low values of G ($G < 10 \, G_0$, see Fig. C1, right-hand panel). We neglect higher CO transitions in our analysis due to the lower detection significance for higher transitions and the possible association of higher CO transitions to dense knots inside Cas A (see Wallström et al. 2013).

The three emission lines of interest were fit simultaneously, using a third-order polynomial for the continuum while the line profile is fit with a sinc function. We assume the line profiles have a width that corresponds to the spectral resolution of the instrument (ranging from 280 to 970 km s^{-1} towards longer wavelengths). Based on the typical line widths (≤ 6 km s^{-1}) for the [C I] 492 GHz, ^{12}CO(2−1) and ^{13}CO(2−1) line emission observed from interstellar clouds in the Perseus arm where Cas A is situated with ground-based telescopes (Mookerjea et al. 2006; Kilpatrick, Bieging & Rieke 2014), we are confident that this assumption holds. Even if line broadening occurred due to the interaction of the interstellar clouds with the expanding SNR, we do not expect to find line widths broader than a few 100 km s^{-1} (a careful check of the line widths in the SPIRE FTS spectra confirms this hypothesis).

To diagnose the ISM conditions based on these three lines, we compared the [C I] 492/CO(4−3) and [C I] 809/[C I] 492 line ratios to PDR models. More specifically, we used the online PDR toolbox (PDRT; Pound & Wolfire 2008) to determine the ISRF scaling factor, G, and the gas density, n_H, in the PDR. Even though the lines were extracted within different apertures due to varying beamsize with wavelength (Makiwa et al. 2013), the surface brightness units allow us to compare the line strength without applying any aperture corrections. The line ratios in the PDRT were calculated for a plane–parallel geometry with elemental abundances and grain properties similar to solar metallicity. While lower CO transitions might be optically thick, we assume that the CO(4−3) and the [C I] lines are optically thin and that we therefore do not need to apply any corrections for opacity to compare the observed line ratios with the PDR model predictions. A direct comparison of observed line ratios with the PDR models also relies on the presumption that UV radiation or collisions dominate the line excitation, and that excitation by shocks is negligible. Kilpatrick et al. (2014) found that towards regions in the south and west of Cas A, the interaction of the shock front and the interstellar clouds causes a broadening of CO lines (line widths of 8–10 km s^{-1} have been observed as compared to the 1–3 km s^{-1} line widths typical for Galactic molecular clouds), which suggests the importance of shock excitation in those regions. In the north, turbulence induced by an interaction with interstellar material results in a wide distribution of radial velocities for MIR fine-structure lines in the *Spitzer* IRS spectra (Kilpatrick et al. 2014). When modelling the fine-structure lines from the SPIRE FTS spectra, we should
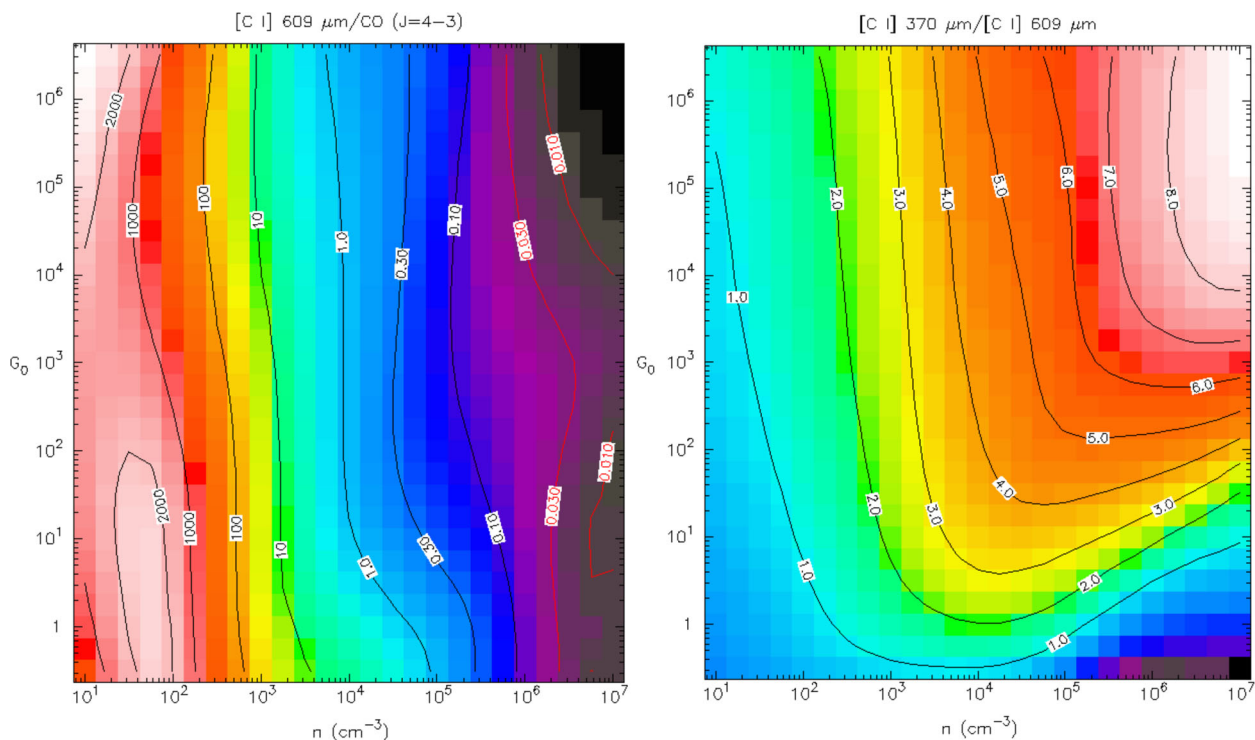
Figure C1. Diagnostic plots from the PDRT (Pound & Wolfire 2008) showing the variation of the line ratios [C I]1−0/CO(4−3) (left) and [C I]2−1/ [C I]1−0 (right) as a function of the radiation field, G and H-nucleus density, n_H.
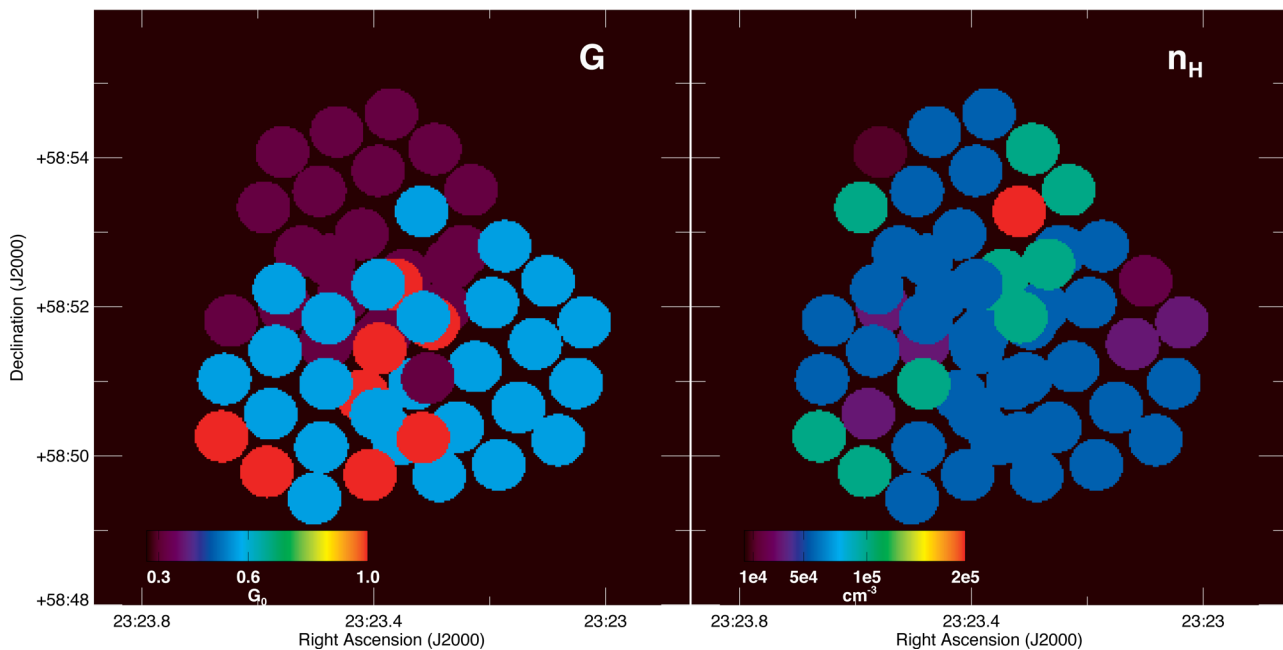
Figure C2. The best-fitting PDR parameters, G and n_H, derived based on the CO(4−3), [C I] 1−0 and [C I] 2−1 line emission measured by the SPIRE LWS bolometers.

therefore be cautious in interpreting line ratios beyond the forward shock front, which might be excited by shocks.

Fig. C2 gives an overview of the best-fitting parameters derived from our PDR modelling of the spectrum in every FTS bolometer. Only bolometers with line detections with a signal-to-noise level ≥2 for all three lines are modelled. The strength of the radiation field was found to range between $G = 0.3\ G_0$ and $1.0\ G_0$, with the majority of bolometers in the central and north-west pointings

yielding results consistent with $G = 0.6\ G_0$[27]. The latter scaling factor is consistent with the G values derived from the ISM dust

[27] Due to the restricted sampling of the radiation field and gas density in the PDR models, no intermediate values are allowed for gas densities between 1, 1.8, 3.2, 5.6 and 10×10^4 cm^{-3} and G values between $G = 0.3\ G_0$, $0.6\ G_0$ and $1.0\ G_0$.

Table D1. The results of the global SED fitting procedure for a variety of SN dust species. We present dust masses and temperatures for the hot (columns 2 and 3), warm (columns 4 and 5) and cold SN dust components (columns 6 and 7) for three different cases with ISRF scaling factors $G = 0.3$, 0.6 and 1.0 $G_{\odot}$, respectively. Columns 8 and 9 list the total dust mass (i.e. the sum of the hot, warm and cold dust masses) and the reduced χ^2 values that correspond to the best-fitting SED model. The uncertainties on the SN dust masses correspond to the 1σ errors computed from the covariance matrix during the SED fitting based on the observational uncertainties of the flux in every waveband. Columns 10 and 11 present the lower limits on the SN dust temperature and mass. The lower limit on the total SN dust mass was calculated by scaling the ISM dust model to the extreme value of the SPIRE 500 µm flux density (i.e. $F_{500} + \sigma_{500}$) to maximize the contribution from ISM dust emission to the global SED (i.e. leaving no room for an SN dust contribution at 500 µm). The dust temperature corresponds to the dust temperature of the coldest SN dust component obtained from this lower limit fit. The numbers in boldface correspond to the results from SED fitting for an ISM model with $G = 0.6 \, G_0$ and an SN dust model with silicate-type grains (MgSiO$_3$, Mg$_{2.4}$SiO$_{4.4}$), and are believed to be representative of the SN dust conditions in Cas A.

Dust species	Hot dust Best fit		Warm dust Best fit		Cold dust Best fit		Total dust Best fit		Total dust Lower limit	
	$T_{\rm d}$ (K)	$M_{\rm d}$ (10^{-3} M$_{\odot}$)	$T_{\rm d}$ (K)	$M_{\rm d}$ (10^{-2} M$_{\odot}$)	$T_{\rm d}$ (K)	$M_{\rm d}$ (M$_{\odot}$)	$M_{\rm d}$ (M$_{\odot}$)	χ^2	$T_{\rm d}$ (K)	$M_{\rm d}$ (lower) (M$_{\odot}$)
				$G = 0.3 \, G_0$						
MgSiO$_3$	120	0.6 ± 0.1	66	1.5 ± 0.2	24	2.2 ± 0.3	2.2 ± 0.3	0.18	30	0.6 ± 0.1
Mg$_{0.7}$SiO$_{2.7}$	190	0.04 ± 0.01	56	26.9 ± 1.8	25	13.7 ± 1.9	14.0 ± 1.9	0.81	26	8.3 ± 1.2
Mg$_{2.4}$SiO$_{4.4}$	130	0.3 ± 0.1	66	1.8 ± 0.2	26	1.2 ± 0.2	1.2 ± 0.2	0.55	30	0.6 ± 0.1
Al$_2$O$_3$ (porous)	115	0.7 ± 0.1	72	0.7 ± 0.1	24	0.6 ± 0.1	0.6 ± 0.1	0.19	33	0.12 ± 0.02
CaAl$_{12}$O$_{19}$	105	1.1 ± 0.1	74	1.0 ± 0.1	16	34.8 ± 5.2	34.8 ± 5.2	1.34	20	4.7 ± 0.6
Am. carbon 'AC1'	115	0.7 ± 0.1	85	0.8 ± 0.1	27	0.6 ± 0.1	0.6 ± 0.1	0.50	40	0.08 ± 0.02
a-C ($E_g = 0.1$ eV)	115	0.7 ± 0.1	77	1.0 ± 0.1	25	1.2 ± 0.1	1.2 ± 0.1	0.31	37	0.2 ± 0.1
				$G = 0.6 \, G_0$						
MgSiO$_3$	**120**	**0.6 ± 0.1**	**68**	**1.2 ± 0.2**	**28**	**0.6 ± 0.1**	**0.6 ± 0.2**	**0.20**	**38**	**0.13 ± 0.02**
Mg$_{0.7}$SiO$_{2.7}$	200	0.03 ± 0.01	55	33.8 ± 1.9	21	26.1 ± 8.4	26.4 ± 8.4	0.58	29	0.6 ± 0.8
Mg$_{2.4}$SiO$_{4.4}$	**130**	**0.3 ± 0.1**	**66**	**1.8 ± 0.2**	**29**	**0.4 ± 0.1**	**0.4 ± 0.1**	**0.47**	**38**	**0.10 ± 0.03**
Al$_2$O$_3$ (porous)	110	1.0 ± 0.1	72	0.7 ± 0.1	27	0.2 ± 0.1	0.2 ± 0.1	0.22	40	0.02 ± 0.01
CaAl$_{12}$O$_{19}$	100	1.6 ± 0.2	74	0.9 ± 0.1	17	12.8 ± 3.6	12.8 ± 3.6	1.26	24	0.7 ± 0.2
Am. carbon 'AC1'	115	0.7 ± 0.1	84	0.8 ± 0.1	29	0.3 ± 0.1	0.3 ± 0.1	0.29	79	0.013 ± 0.001
a-C ($E_g = 0.1$ eV)	115	0.7 ± 0.1	77	1.0 ± 0.1	27	0.5 ± 0.2	0.5 ± 0.1	0.24	40	0.03 ± 0.02
				$G = 1.0 \, G_0$						
MgSiO$_3$	115	0.7 ± 0.1	68	1.1 ± 0.2	39	0.06 ± 0.02	0.07 ± 0.02	0.34	63	0.021 ± 0.002
Mg$_{0.7}$SiO$_{2.7}$	185	0.04 ± 0.01	55	32.6 ± 2.2	30	0.3 ± 0.8	0.6 ± 0.8	0.61	56	0.28 ± 0.02
Mg$_{2.4}$SiO$_{4.4}$	125	0.4 ± 0.1	63	2.5 ± 0.2	33	0.01 ± 0.06	0.04 ± 0.06	0.45	64	0.022 ± 0.002
Al$_2$O$_3$ (porous)	110	1.0 ± 0.1	70	0.8 ± 0.1	12	1.0 ± 1.8	1.0 ± 1.8	0.28	74	0.007 ± 0.001
CaAl$_{12}$O$_{19}$	100	1.5 ± 0.2	75	0.8 ± 0.1	17	5.1 ± 4.3	5.1 ± 4.3	1.24	75	0.010 ± 0.001
Am. carbon 'AC1'	115	0.7 ± 0.1	82	1.0 ± 0.1	23	0.4 ± 0.7	0.4 ± 0.7	0.28	86	0.008 ± 0.001
a-C ($E_g = 0.1$ eV)	115	0.7 ± 0.1	75	1.2 ± 0.1	22	1.3 ± 0.1	1.3 ± 0.1	0.31	77	0.010 ± 0.001

SED modelling of the regions surrounding Cas A (see Fig. 8, top left panel). The hydrogen nucleus density was found to range between $n_{\rm H} = 3.2 \times 10^4$ and 10^5 cm^{-3}. For the northern pointing, the line spectra from the majority of bolometers were found to require values of $G = 0.3 \, G_0$ and an H-nucleus density $n_{\rm H} = 10^5$ cm^{-3}, while the dust SED modelling suggests lower gas densities and stronger radiation fields ($G \sim 1 \, G_0$) just north of Cas A. Possible shock excitation, caused by the interaction of the expanding shock front with interstellar clouds, could contribute to the line emission. Kilpatrick et al. (2014) have indeed identified high-velocity features in their MIR spectra due to turbulence governed by the interaction of the shock front with dense interstellar material. Alternatively, some of the line emission might be associated with dense clumps in the SNR.

Compared to the PDR analysis of Mookerjea et al. (2006), based on a [C I] 492 GHz map, who found gas densities $n_{\rm H}$ between 10^2 and 10^3 cm^{-3} under the assumption of an illuminating radiation field with $G = 1.0 \, G_0$, the gas densities derived from our PDR analysis are almost two orders of magnitude higher. Due to the different sets of tracers used by Mookerjea et al. (2006) ([C I] 492 GHz, ^{12}CO(2−1), ^{13}CO(2−1) and in this work ([C I] 492 and 809 GHz, ^{12}CO(4−3)), we might expect to probe regions deeper within the cloud, resulting in higher gas densities. The fixed radiation field of

$G = 1.0 \, G_0$ used by Mookerjea et al. (2006) furthermore implies that a lower column of material would be required to reproduce the line emission compared to radiation fields of 0.3 G_0 or 0.6 G_0, which could bias their PDR analysis towards low gas densities, while our analysis is biased to higher gas densities due to using a different set of tracers.

Fig. C2 indicates that the strength of the radiation field that illuminates the ISM material along the sightlines to Cas A does not vary strongly and is consistent with an average value of 0.6 G_0. We therefore adopt an ISRF scaling factor of 0.6 G_0 to model the ISM dust emission along the line of sight of Cas A (see Section 4). In Section E2, we explore the effects on the SN dust mass estimates of assuming lower (0.3 G_0) and higher (1.0 G_0) scaling factors. A radiation field $G = 0.6 \, G_0$ corresponds to an ISM dust temperature of $T_{\rm d} \sim 16.4$ K. This dust temperature is consistent with the ISM dust temperature near Cas A, $T_{\rm d} \sim 16.5$ K, derived by Sibthorpe et al. (2010).

APPENDIX D: GLOBAL SED FITTING

We use the global fluxes (see Table 2), after subtraction of synchrotron radiation and line contributions, to determine the total amount of emission from ISM dust projected on Cas A and SN

dust in Cas A. Similar to the spatially resolved SED fitting procedure in Section 4, the global emission spectrum is fitted with a four-component SED model with an ISM dust component and hot, warm and cold SN dust components. The ISM model is based on the THEMIS dust model from Jones et al. (2013) illuminated by a radiation field of $G = 0.6\,G_0$ scaled to the dust mass that is derived from the SPIRE 500 μm flux and the relations in equation (1). The hot SN dust component is assumed to have a fixed dust composition of silicates with a low Mg/Si ratio of 0.7 (i.e. $Mg_{0.7}SiO_{2.7}$) with dust temperatures in the range 100–200 K. The SED modelling procedure is repeated for the dust species listed in Table 3 under the assumption that it dominates the dust composition of the warm+cold SN dust components. We assume dust temperatures between 40–100 K and 10–40 K for the warm and cold SN dust components. Table D1 gives an overview of the best-fitting parameters derived from the global SED fitting.

Similarly to the resolved SED fitting procedure, the SED models with an $Mg_{0.7}SiO_{2.7}$, $CaAl_{12}O_{19}$ and Al_2O_3 dust composition for the warm and cold SN dust components result in SN dust masses that are unrealistically high given the constraints on metal production based on nucleosynthesis models for SN type II and type IIb events for a 30 and 18 $M_\odot$ progenitor, respectively. These grains can therefore be ruled out as the dominant dust species that form in Cas A[28]. For carbonaceous grains, the best fit would imply a dust mass of 0.3–0.5 $M_\odot$ with a lower limit of 0.01–0.03 $M_\odot$ of carbon grains. Besides 0.3–0.5 $M_\odot$ of carbon locked up in grains being considered unrealistic due to the lack of sufficient carbon production by the progenitor of Cas A, the ejecta of Cas A have been shown to be predominantly oxygen rich (Chevalier & Kirshner 1979; Docenko & Sunyaev 2010). Assuming that the newly formed grains are silicates ($MgSiO_3$ or $Mg_{2.4}SiO_{4.4}$), we would need 0.4–0.6 $M_\odot$ of these oxygen-rich grains, with a lower limit of 0.1 $M_\odot$, at a temperature of $T_d \sim 30$ K to reproduce the global emission spectrum of Cas A.

Fig. D1 shows the best-fitting global SED model assuming an ISM dust SED model with radiation fields $G = 0.3\,G_0$, $0.6\,G_0$ and $1.0\,G_0$. For these SED fits, we have assumed $Mg_{0.7}SiO_{2.7}$ dust for the hot SN dust component and $MgSiO_3$ dust for the warm and cold SN dust components. Even though the IRAC 8 μm and *WISE* 12 μm data points were not used to constrain the multicomponent ISM+SN model, the best-fitting model SED seems to reproduce the MIR emission in those wavebands within the error bars (with the exception of the *WISE* 12 μm data point for the $G = 0.3\,G_0$ model). The good agreement between model and observations seems to indicate that a combination of a warm SN dust component and the emission features originating from small hydrocarbons (or polycyclic aromatic hydrocarbons) in the diffuse ISM are able to account for the MIR emission observed towards Cas A. The SCUBA 850 μm data point is also omitted from the fitting procedure. We will discuss the SCUBA 850 μm observations in Appendix F2.

The SN dust masses derived from the spatially resolved SED fits (see Section 4) are in overall agreement with the dust masses derived from the global SED fits within the limits of observational uncertainties. Since the variation in the SN dust emission spectrum and ISM dust contribution within an aperture of radius 165 arcsec can introduce possible uncertainties in the global SED parameters (because local variations in ISM dust contribution and SN dust mass and temperature are averaged out in the global spectrum that includes all the emission within an $R = 165$ arcsec region), we
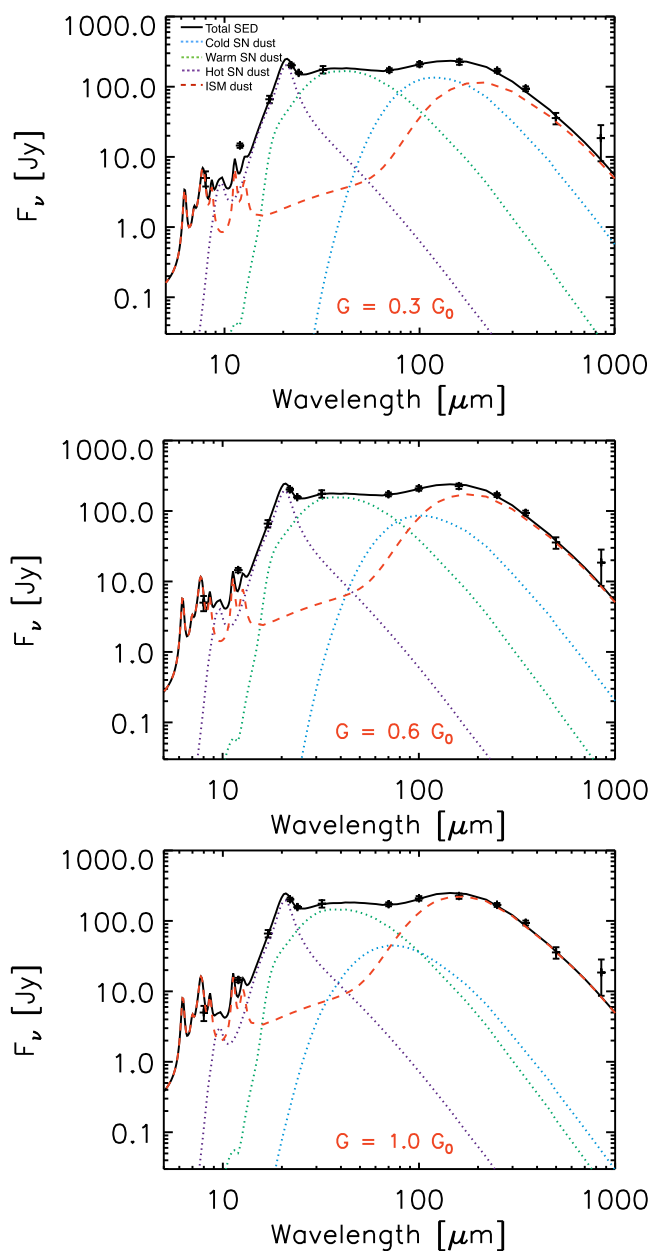

Figure D1. The best-fitting global SED models fit to the 17–500 μm photometry after subtraction of the contribution from line emission and synchrotron radiation, assuming a Galactic ISM dust model illuminated by a radiation field $G = 0.3\,G_0$ (top), $0.6\,G_0$ (middle) and $1.0\,G_0$ (bottom). The legend in the top panel explains the line formatting and colours associated with the various SN and ISM dust components.

attach more weight to the results of the spatially resolved SED fitting analysis.

APPENDIX E: MODEL VERIFICATION

E1 Comparison between model and observations

Here, we compare the modelled global dust SED and spatially resolved dust emission maps to observations to verify whether the multicomponent ISM+SN model is capable of reproducing the observed IR–submm SEDs. The global relative offsets between observed and modelled fluxes [i.e. $(F_{obs} - F_{model})/F_{obs}$] at various

---

[28] Note that we cannot rule out that some of these dust species formed within Cas A, but they will not dominate the mass fraction of freshly formed grains.
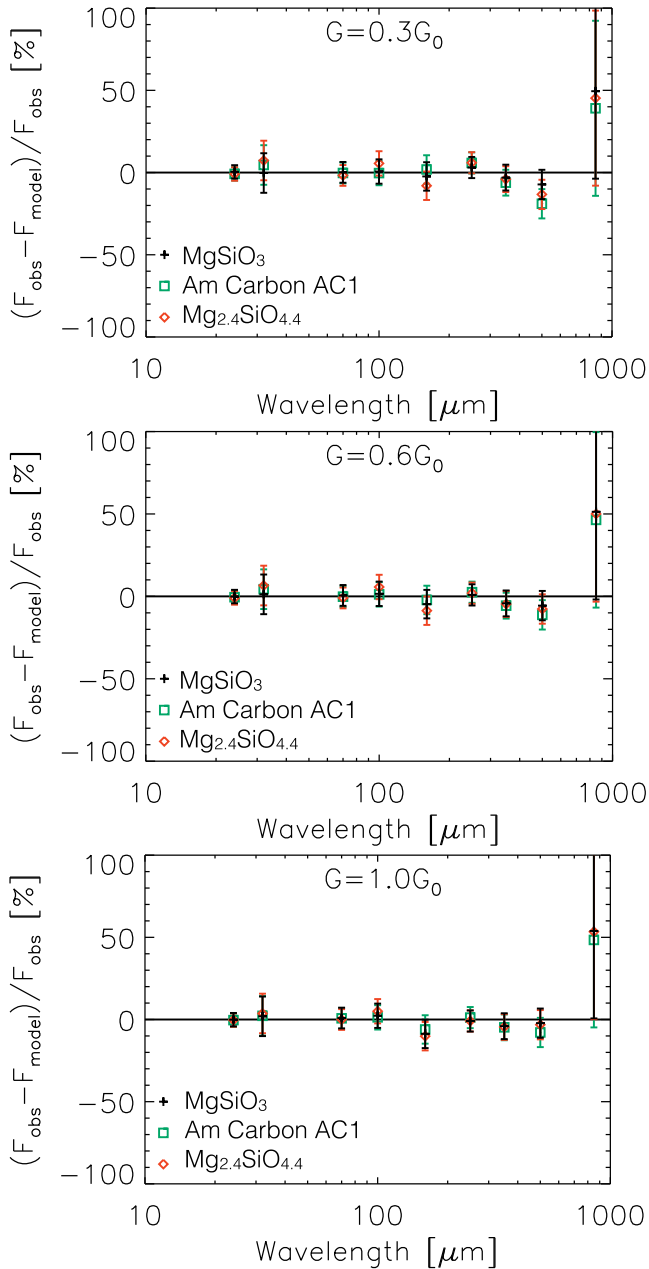
Figure E1. Percentage offsets from the observations, $(F_{obs} - F_{model})/F_{obs}$, for the global SED models. The top, middle and bottom panels show the model deviations for ISM dust models with $G = 0.3$, 0.6 and 1.0 $G_{\odot}$, respectively. The model offsets are shown for different SN dust compositions ($MgSiO_3$ in black, amorphous carbon in green and $Mg_{2.4}SiO_{4.4}$ in red) used for the warm and cold components. The rightmost data point corresponds to the SCUBA 850 µm flux reported by Dunne et al. (2009). Its offset from the best-fitting models is discussed in Section F2.

wavelengths are shown in Fig. E1 for models with the three different ISM dust models ($G = 0.3$, 0.6 and 1.0 $G_{\odot}$) and various SN dust species. All dust SED models show small residuals, independent of the assumed dust composition or strength of the illuminating ISRF, and reproduce the MIPS 24 µm, IRS 32 µm continuum, PACS 70, 100 and 160 µm and SPIRE 250, 350 and 500 µm data points within the error bars. While the SCUBA 850 µm is not used to constrain the SED fitting procedure, all models are at the low end of the observed SCUBA 850 µm data flux (see also Appendix F2).

To verify whether the multicomponent model reproduces the observed spectrum in every pixel, in Fig. E2 we compare the emission predicted by the SED model with observations. To highlight any model deviations from the observations, the residual images [i.e. observed flux − modelled flux)/observed flux] and histogram of residuals are shown in the third and fourth columns of Fig. E2, respectively. The residuals between the model and observations show random offsets centred around 0 at every wavelength rather than a systematic offset, which suggests that the multicomponent SN+ISM dust model is adequate to fit the IR/submm SED. At 500 µm, several pixels show an offset between observations and model up to −50 per cent. Given that the offset arises in regions where the ISM contribution is low, and the model overestimates the ISM dust emission in those regions, we do not believe that this discrepancy will affect the determination of the SN dust mass in Cas A.

E2 The effect of variations in the adopted radiation field

In this section, we analyse the effects of variations in the strength of the ISRF illuminating the ISM dust along the sightline of Cas A on the determination of the SN dust mass. For the multicomponent SED fitting procedures on resolved and global scales (see Section 4 and Appendix D, respectively), we have assumed a constant radiation field strength of $G = 0.6$ G_0. Based on local variations in G in the areas surrounding Cas A (see Fig. 8, left-hand panel), it is however likely that regional variations occur, which might have an effect on the SN dust temperatures and dust masses derived for Cas A. The three sets of SED models that were run for $G = 0.3$ G_0, 0.6 G_0 and 1.0 G_0 give an idea of the influence of the variation in radiation field illuminating the ISM material on the SN dust mass and temperature estimates. We have not considered the results of ISM models with a stronger ISRF (i.e. $G > 1.0$ G_0) due to an overestimation of IR–submm fluxes for Cas A upon scaling these ISM dust model SEDs to the SPIRE 500 µm flux (after subtraction of the synchrotron radiation). The best-fitting SN dust masses and temperatures derived for these three sets of SED models can be examined in Tables 4 and D1 for the spatially resolved and global SED fits, respectively.

Comparing the SED fitting results for different ISRFs, a general trend emerges that ISM models with lower dust temperatures (corresponding to lower G) yield larger SN dust masses, which trivially follows from the reduced IR/submm emission of ISM dust and is compensated for with an increase in the SN dust emission at those wavelengths. Fig. E3 demonstrates how the derived SN dust temperatures, and consequently the SN dust masses, are sensitive to the radiation field that is assumed to illuminate the ISM dust. The overall distribution of SN dust temperatures within Cas A is similar for the three models regardless of the ISRF scaling factor. But with cold SN dust temperatures ranging from 20 to 40 K (middle panels), the total dust mass can differ by factors of a few. More specifically, we derive dust masses of 1.4, 0.5 and 0.2 $M_{\odot}$ from the resolved SED maps assuming that the warm and cold SN dust is composed of $MgSiO_3$ grains with ISM dust illuminated by a radiation field $G = 0.3$ G_0, 0.6 G_0 and 1.0 G_0, respectively. Similarly, the resolved SED fitting procedure for an $Mg_{2.4}SiO_{4.4}$ dust composition results in dust masses of 0.9, 0.3 and 0.1 $M_{\odot}$ for different ISRFs, respectively. The SN dust masses derived for a $G = 0.3$ G_0 ISM model exceed the maximum dust masses (0.4–1.4 $M_{\odot}$ and 0.3–0.9 $M_{\odot}$ for $MgSiO_3$ and $Mg_{2.4}SiO_{4.4}$ dust) derived from the metal production predicted by nucleosynthesis models (under the assumption that all the metals are locked in dust grains), and are therefore considered unrealistic.
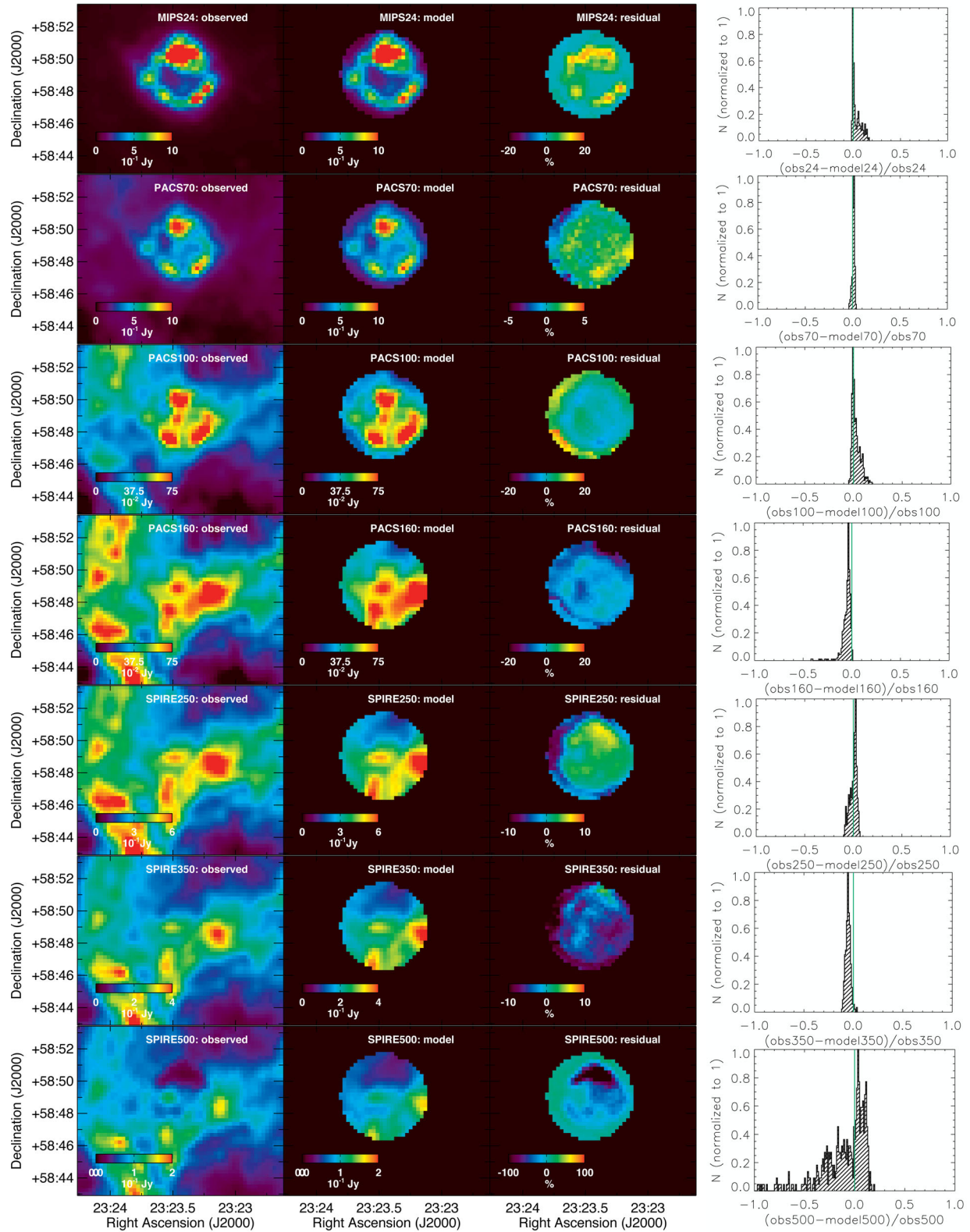
Figure E2. The observed (left column) and modelled (second column) MIPS 24 μm, PACS 70, 100 and 160 μm and SPIRE 250, 350 and 500 μm images. The observed maps correspond to the *Spitzer* and *Herschel* maps after subtraction of the synchrotron radiation and line emission components (leaving a combination of ISM and SN dust emission). The modelled images result from a multicomponent SED fit in each individual pixel. The third column shows the residual image, $(F_{obs} - F_{model})/F_{obs}$, as percentage deviations to highlight deviations of the model from the observations. The scale of the residual images has been adjusted to cover the entire range of residuals. In the right-hand column, the histogram of residuals is shown for every waveband.
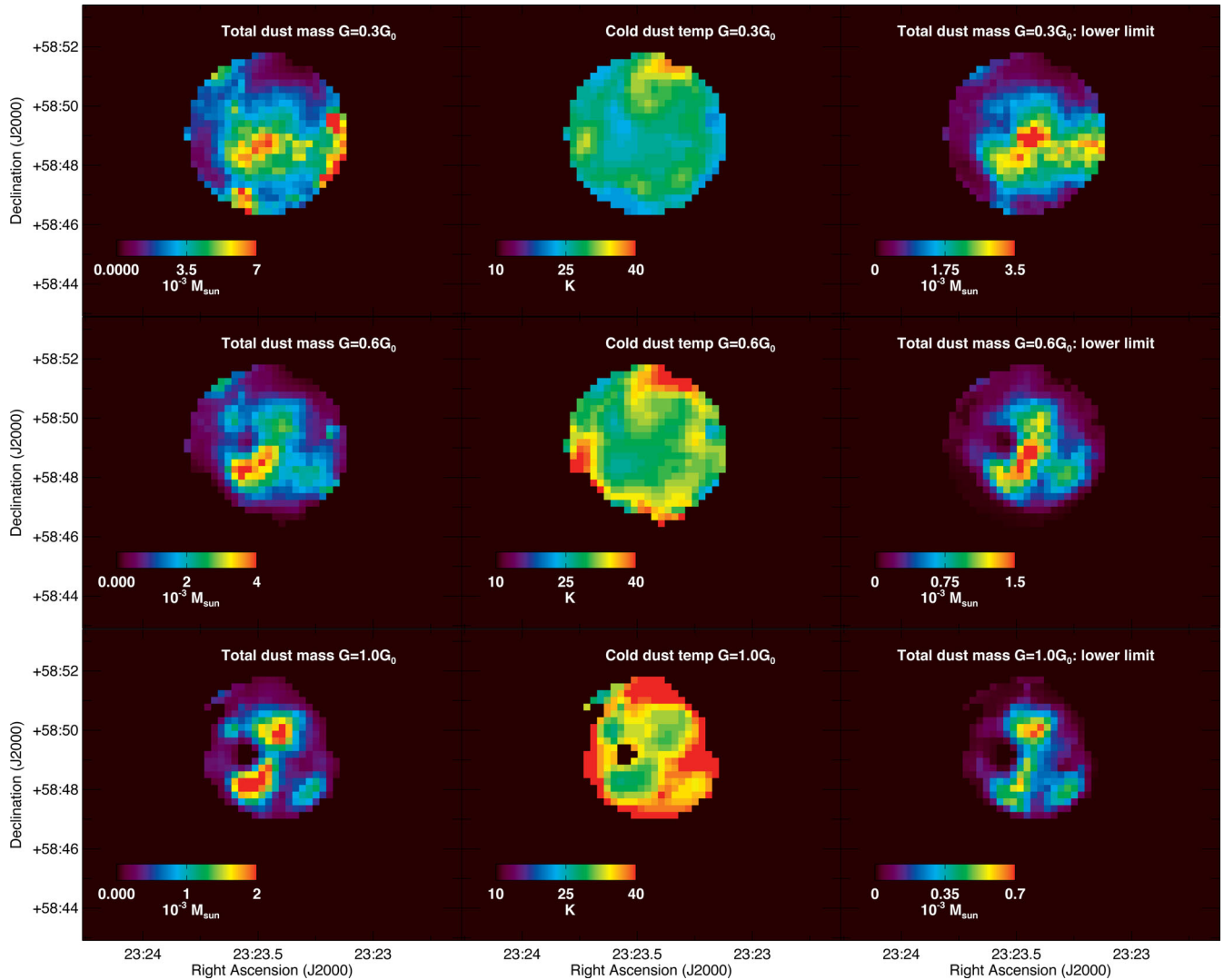
Figure E3. Total SN dust mass maps (first column) and cold SN dust temperature maps (second column) derived from spatially resolved SED fitting with an Mg$_{0.7}$SiO$_{2.7}$+MgSiO$_3$ SN dust composition and ISM dust models with radiation fields of $G = 0.3\ G_0$, $0.6\ G_0$ and $1.0\ G_0$ (see top, middle and bottom row, respectively). The last column shows the lower limit to the total SN dust mass, derived by fixing the normalization of the ISM dust model to reproduce the $F_{500}+\sigma_{500}$ flux density.

Given the uncertainties on the nucleosynthesis models (Woosley & Weaver 1995) and the mass of the progenitor, we argue that the condensation of 0.3–0.5 M$_\odot$ (for a 0.6 G_0 ISM model) or 0.1–0.2 M$_\odot$ (for a 1.0 G_0 ISM model) of dust in Cas A is reasonable.

Based on a total ejecta mass estimate of 2–4 M$_\odot$ derived both from X-ray observations of Cas A (Willingale et al. 2002) and kinetic arguments to determine the mass and explosion energy from optical observations (Chevalier & Oishi 2003; Laming & Hwang 2003), these dust masses imply that the condensation of elements has been extremely efficient. Given that the progenitor has been predicted to have had a mass of 23–30 M$_\odot$ (Kifonidis et al. 2001; Pérez-Rendón et al. 2002; Young et al. 2006; Pérez-Rendón et al. 2009), the total ejecta mass could be larger than 4 M$_\odot$, with the missing gas mass in the form of clumped neutral gas, which might also harbour the detected cold dust in the ejecta. Alternatively, most of the initial stellar mass might have been lost by the progenitor prior to explosion with estimated values

of the swept-up mass of ∼8 M$_\odot$ up to possibly 20 M$_\odot$ (Willingale et al. 2003).

We have shown that the ISM dust model with $G = 0.6\ G_0$ most closely resembles the ISRF along the sightline of Cas A (based on SED fitting in the surrounding regions of Cas A, and a PDR analysis of submm emission lines; see Figs 8 and C2, respectively). We therefore attach more weight to the SN dust masses of 0.5 M$_\odot$ (MgSiO$_3$), 0.3 M$_\odot$ (Mg$_{2.4}$SiO$_{4.4}$) and 0.5–0.6 M$_\odot$ (carbonaceous grains) derived from SED models with $G = 0.6\ G_0$ ISM dust models. Due to possible variations in the ISRF along the line of sight, we cannot rule out that the local radiation field near Cas A is closer to the solar ISRF which would imply SN dust masses of 0.1–0.2 M$_\odot$. Being conservative, we can conclude that the mass of dust produced in Cas A is between 0.1 and 0.6 M$_\odot$ and likely consists of a combination of mostly silicate-type (MgSiO$_3$ or Mg$_{2.4}$SiO$_{4.4}$) grains and some form of carbonaceous dust.
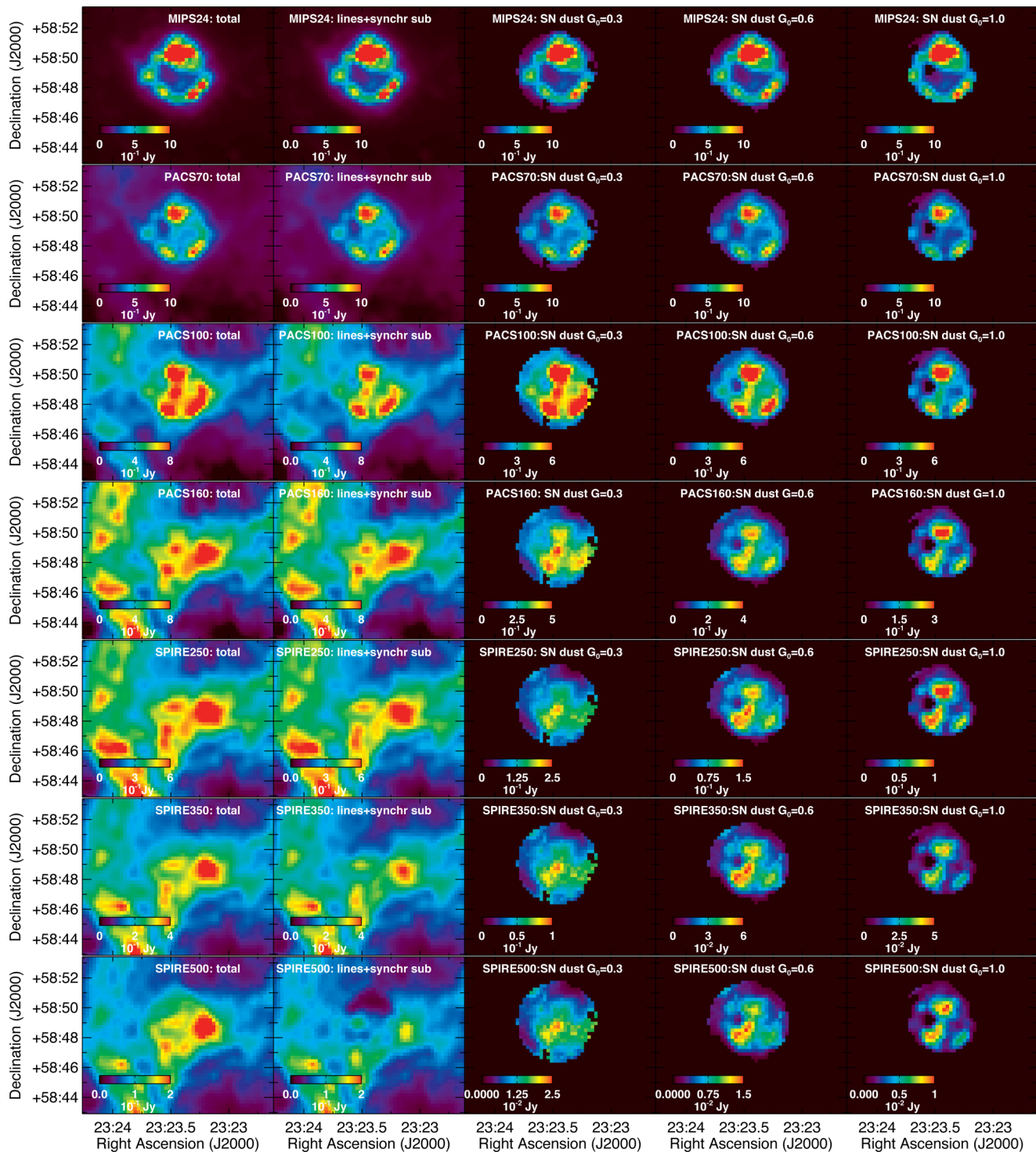
Figure F1. Infrared and submm images of Cas A for different emission components. From top to bottom, MIPS 24 μm, PACS 70, 100 and 160 μm and SPIRE 250, 350 and 500 μm images are shown. The first column shows total emission maps, the second column shows the same maps after correcting for synchrotron radiation and line emission. The third, fourth and fifth columns show the dust emission intrinsic to the SNR derived after subtracting best-fitting models for ISM dust illuminated by radiation fields of $G = 0.3\,G_0$, $0.6\,G_0$ and $1.0\,G_0$, respectively.

APPENDIX F: MODEL PREDICTIONS

F1 Cas A: various IR–submm components

Based on the models constructed for each of the emission components, we can determine the relative contribution of various con-

taminants at every wavelength. Fig. 13 gives a schematic overview of the relative contributions at IR and submm wavelengths. Based on our models for line emission, synchrotron radiation and ISM dust emission, we can furthermore construct residual images with the remaining SN dust emission. The images in Fig. F1 (first column) provide an overview of the total emission in the MIPS 24 μm,

PACS 70, 100 and 160 μm, and SPIRE 250, 350 and 500 μm wavebands. The second column shows the same maps after subtraction of the contributions from line emission and synchrotron radiation, while the third, fourth and fifth columns show the emission intrinsic to the SNR derived from modelling the residual SED with a multicomponent SN+ISM dust model for ISRF scaling factors of $0.3\,G_0$, $0.6\,G_0$ and $1.0\,G_0$, respectively.

At MIR wavelengths, the largest contributor to the broad-band emission is from warm dust in the SNR, with contributions of 92 per cent, 97 per cent, 75 per cent and 94 per cent in the IRS 17 μm, *WISE* 22 μm, MIPS 24 μm and IRS 32 μm wavebands, respectively. In the PACS 70 μm waveband, the emission is still dominated by warm SN dust emission (84 per cent), while the PACS 100 μm waveband has a non-negligible contribution from ISM dust emission (34 per cent) in addition to a large SN dust contribution (54 per cent). With the emission of ISM dust peaking just longwards of 100 μm (see Fig. 6), the contribution from SN dust emission drops significantly in the PACS 160 μm and SPIRE wavebands. For ISM dust illuminated by a radiation field with $G = 0.6\,G_0$, the emission of dust intrinsic to Cas A contributes 30 per cent, 15 per cent, 10 per cent and 4 per cent of the total emission in the PACS 160 μm and SPIRE 250, 350 and 500 μm maps, respectively. In the PACS 100 and 160 μm maps, we can identify an emission peak in the inner regions of the remnant in addition to the three peaks of SN dust emission in the reverse shock regions. In the SPIRE wavebands, this central peak becomes more prominent compared to the reverse shock region. This SN dust component in the inner regions was already identified by Barlow et al. (2010) and Arendt et al. (2014). The same emission pattern identified in the PACS wavebands (i.e. one central peak and three secondary peaks in the reverse shock) is prominently present in the SN dust emission maps derived for an ISRF field $G = 0.6\,G_0$. We argue that this supports the assumption that the $G = 0.6\,G_0$ ISM model best represents the ISM conditions towards Cas A.

Barlow et al. (2010) performed a similar decomposition of the different emission components to the *Herschel* PACS and SPIRE wavebands, using an earlier version of the HIPE pipeline to reduce the *Herschel* data. Although their assumptions when modelling the synchrotron, line and interstellar dust emission were different,[29] the contributions of the different emission sources at various wavelengths are similar. We find a contribution from synchrotron radiation of 3.6 per cent, 3.5 per cent, 4.7 per cent, 7.9 per cent, 16.3 per cent and 39.7 per cent in the PACS 70, 100 and 160 μm and SPIRE 250, 350 and 500 μm bands, while Barlow et al. (2010) reported contributions of 3.7 per cent, 4.2 per cent, 6.8 per cent, 9.2 per cent, 21.1 per cent and 47.9 per cent in those wavebands, respectively. While our adopted spectral index (-0.644) is even shallower compared to their value of -0.70, their somewhat higher synchrotron contribution most likely arises from their extrapolation of the emission at 6 cm. The normalization of our synchrotron component is based on the recent *Planck* measurements, which are closer in wavelength to the *Herschel* data points. The ISM dust contributions of 10.7 per cent, 39.6 per cent, 74.1 per cent, 83.9 per cent, 75.0 per cent and 52.9 per cent in those wavebands estimated by

Barlow et al. (2010) are consistent within 5–10 per cent to our estimated ISM contributions for a radiation field with scaling factor $G = 0.6\,G_0$ (12.2 per cent, 34.4 per cent, 70.2 per cent, 76.4 per cent, 77.6 per cent and 59.3 per cent at 70, 100, 160, 250, 350 and 500 μm, respectively). The contributions estimated by Barlow et al. (2010) for the SN dust emission[30] at 70 μm (85.8 per cent), 100 μm (47.9 per cent) and 160 μm (19.3 per cent), and at 250 μm (6.9 per cent), 350 μm (3.9 per cent) and 500 μm (0 per cent) are within the range of percentages derived here from our spatially resolved decomposition analysis (83.6, 53.9, 29.6, 14.9, 9.7 and 4.4 per cent, respectively). Our SN dust contributions are consistently higher by 4–10 per cent in the PACS 100 and 160 μm and SPIRE 250, 350 and 500 μm wavebands, due to our lower estimates for the synchrotron and ISM dust emission at submm wavelengths.

F2 A simulated 850 μm map

By extrapolating the best-fitting multicomponent SED model to longer wavelengths and convolving the model with the SCUBA 850 μm filter response curve, we are able to produce a modelled image of the ISM and SN dust emission at 850 μm. To this image, we add the modelled synchrotron radiation (using the coefficients derived in Section 3.1) to simulate a predicted total 850 μm image based on the models derived in this paper. Fig. F2 presents the modelled synchrotron radiation, ISM and SN dust emission at 850 μm (top row). The bottom left panel shows the sum of all model contributions at 850 μm, and can directly be compared to the observed SCUBA 850 μm image (bottom right panel). Given that our model resolution of 36 arcsec is coarser compared to the resolution of the SCUBA 850 μm image (15 arcsec), our model is not sensitive to all the structures detected in the SCUBA 850 μm image. The overall emission features in our simulated SCUBA 850 μm map compare well to the observed SCUBA 850 μm map, with both showing a clear emission peak in the west and secondary peaks in the northwest and south-east.

Although the modelled and observed SCUBA 850 μm images show a great resemblance, our global model flux at 850 μm (measured within an aperture with radius of 165 arcsec), $F_{\text{model, 850}} = 41.3 \pm 9.9$ Jy[31] is lower compared to the SCUBA 850 μm flux measurement $F_{\text{obs, 850}} = 50.8 \pm 5.6$ Jy (Dunne et al. 2003), but still consistent within the large error bars due to the uncertainty on the exact synchrotron contribution at 850 μm. Our estimated contribution of synchrotron radiation (32.3 ± 8.1 Jy) is similar to the values used by Dunne et al. (2003, 34.9 Jy) and Dunne et al. (2009, 30.7 Jy). Our current model predicts that the ISM dust emission contributes about 8.6 ± 5.7 Jy, with only 0.4 ± 0.1 Jy originating from SN dust. The latter ISM and SN dust contributions are incompatible with the lower limit of 6.0 Jy for the SN dust emission from Cas A (and thus upper limit for the 850 μm ISM dust flux of 14.1 Jy) derived by Dunne et al. (2009) based on submm polarimetry. The high level of polarization (30 per cent) of SN dust found by Dunne et al. (2009) seems hard to explain in the framework of our model with an SN dust flux of only 0.4 Jy. If the polarized emission would instead come from ISM dust, it surpasses the average intrinsic dust polarization

---

[29] Barlow et al. (2010) modelled the synchrotron emission based on a VLA 6 cm image and a spectral index of -0.70. The ISM dust emission is estimated based on average PACS 100/160 and PACS 70/160 colours in bright regions of the ISM and used to scale the PACS 160 μm image to subtract the ISM dust contribution at 70 μm, 100 μm and submm wavelengths.

[30] We summed the flux from the warm and cool SN dust components of Barlow et al. (2010) to derive their total SN dust emission for Cas A at each wavelength.

[31] The estimated uncertainty on the total modelled 850 μm emission is derived from the combined uncertainty on the synchrotron model flux and the errors on the relative contribution of ISM and SN dust emission at 850 μm.
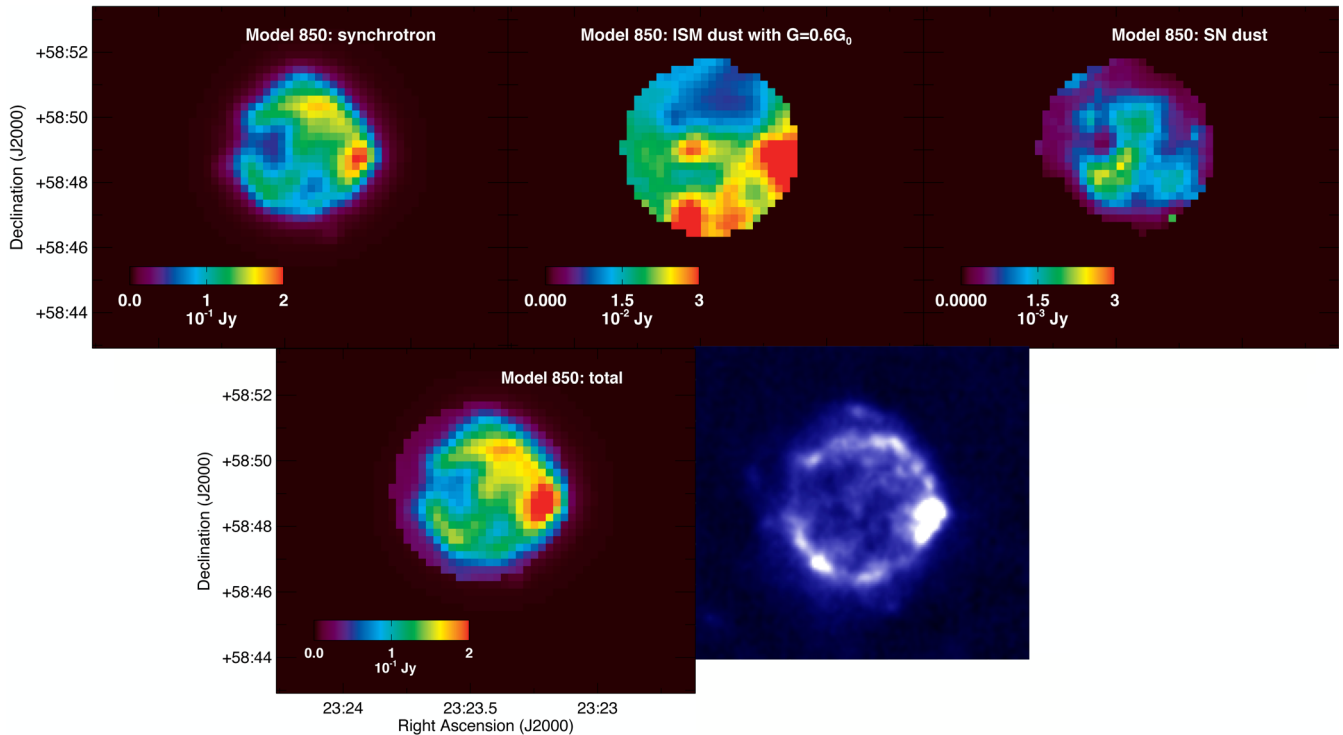
Figure F2. Top panels, from left to right: the modelled synchrotron radiation, the ISM emission and the SN dust emission at 850 μm, based on our best-fitting SED model for an ISM dust model illuminated by a radiation field $G = 0.6\,G_0$ and an SN dust composition of $Mg_{0.7}SiO_{2.7}$ (hot component) $+ MgSiO_3$ (warm and cold components). The bottom panels show the total model emission at 850 μm (left), compared to the SCUBA 850 μm image published by Dunne et al. (2003, see their fig. 1).

of 12 per cent measured by Planck Collaboration XLIV (2016). The alignment of dust grains in the ISM surrounding Cas A might be stronger than usually found in the diffuse ISM, which might provide a possible explanation for the high degree of polarization. The extrapolation of our model is consistent with the conclusion from Krause et al. (2004) that most of the emission at 850 μm arises from ISM dust emission after subtraction of the synchrotron component.

Our current model for synchrotron+ISM+SN dust emission at 850 μm does show a 9.5 Jy deficit compared to the SCUBA 850 μm flux (50.8 ± 5.6 Jy, Dunne et al. 2003) and *Planck* 850 μm flux (52 ± 7 Jy, Planck Collaboration XXXI 2016). Given that we already derive a large SN dust mass (0.4–0.7 M$_\odot$) making a 0.4 Jy flux contribution at 850 μm, it seems highly unlikely that the model SN dust flux could be increased without invoking unrealistically high SN dust masses. We furthermore reject a scenario in which the offset at 850 μm is caused by model deviations from the Galactic ISM dust emission, given that the small relative offsets between the best-fitting ISM dust models and the observed PACS 100 and 160 μm and SPIRE 250, 350 and 500 μm data points are within the observational uncertainties. We thus argue that the missing emission at 850 μm most likely arises from synchrotron radiation. Using a power-law index of −0.54 determined based only on *Planck* data (see Section 3.1) would be sufficient to increase the synchrotron radiation at 850 μm to 37.6 Jy. The updated model for an MgSiO$_3$ warm+cold SN dust composition and ISM model with $G = 0.6\,G_0$ predicts 850 μm contributions of 7.9 and 0.5 Jy from ISM and SN dust emission, which would result in a total modelled flux at 850 μm of 46 Jy, consistent with the observed SCUBA 850 μm (50.6 ± 5.6 Jy) and *Planck* 850 μm (52 ± 7 Jy) fluxes. A small change in spectral index thus enables one to account for the 850 μm deficit without affecting the main results of the paper.

F3 An interstellar extinction map

Based on the maps of the total SN dust mass and ISM dust mass obtained from the spatially resolved SED fitting in Section 4, we can infer the spatial variation in optical extinction towards Cas A. For a foreground dust screen model, the v-band attenuation is calculated based on the average extinction to gas column-density ratio in the solar neighbourhood, $A_V/N_H = 6.53 \times 10^{-22}$ mag cm^2 (Paradis et al. 2012), and a dust-to-hydrogen ratio $\Sigma M_d/(N_H m_H) = 0.0056$ (derived from the Jones et al. 2013 ISM dust model), which results in

$$A_V = 1.46 \frac{\Sigma M_d}{10^5\,M_\odot\,kpc^{-2}}\ \text{mag.} \tag{F1}$$

Fig. F3 presents the A_V maps for interstellar and SN dust extinction. The position of the point-like X-ray source identified by Pavlov et al. (2000) is indicated with a black cross in the right-hand panel. The interstellar visual extinction varies from $A_V = 3$ mag in the north-west of Cas A, where the extinction is lowest, to peaks of $A_V = 15$ mag in the south-east and west, with an average A_V between 6 and 8 mag. These values are consistent with the visual extinctions derived by Hurford & Fesen (1996, $A_V \sim 4$–6 mag) and Reynoso & Goss (2002, A_V up to 8 mag) based on optical and near-infrared spectra and H$_2$CO absorption, respectively. While the H$_2$CO-derived extinction maps have a resolution of 6 arcsec (i.e. six times better compared to the SPIRE 500 μm resolution with FWHM ∼ 36 arcsec), our interstellar extinction map shows the same peaks in A_V towards the west, south-east and near the centre of Cas A. We are therefore confident that the ISM dust emission was modelled accurately, and the remaining dust emission can be attributed to SN dust emission. Based on our A_V maps for the ISM
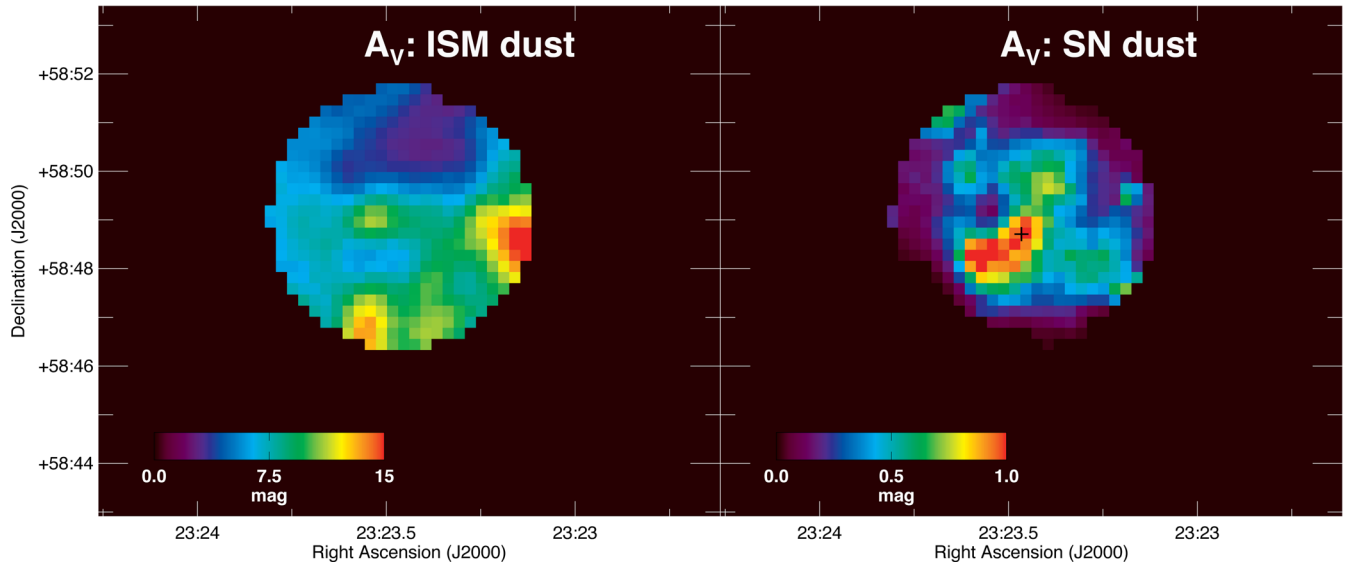
Figure F3. Map of the visual extinction, A_V, for the ISM dust projected against Cas A (left) and for SN dust (right), derived from the multicomponent SED modelling presented in Section 4. The black cross in the right-hand panel indicates the position of the remnant of the SN.
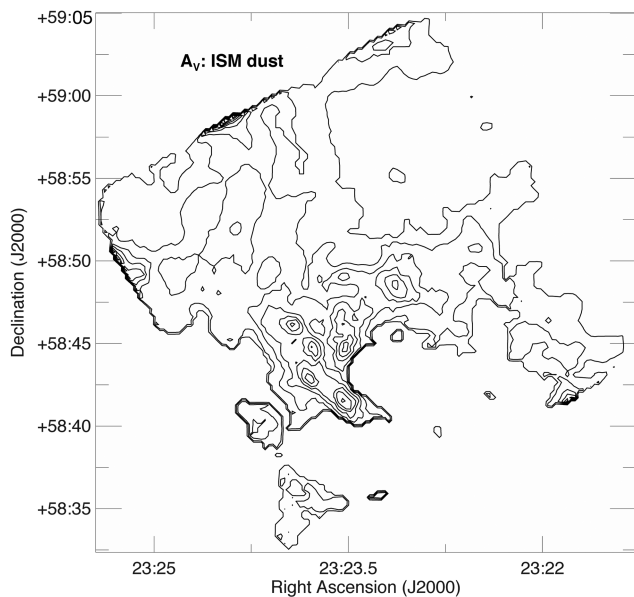

Figure F4. Contour map of the visual extinction, A_V, due to ISM dust for the entire field observed with *Herschel* PACS and SPIRE instruments, as derived from the SED modelling of the ISM dust emission presented in Section 3.2 and the multicomponent SED modelling presented in Section 4. The contour levels start at $A_V = 2.5$ increasing in steps of 2.5 up to $A_V = 20$.

and SN dust, we can estimate the probability to detect a possible binary companion which was argued to be responsible for the stripping of hydrogen gas from the progenitor of Cas A during the evolved stellar phase (Young et al. 2006). The high levels of visual extinction ($A_V \sim 8$–10 mag) towards the central regions make it very difficult to detect the SNR or the presence of a binary star at ultraviolet and optical wavelengths but near-IR imaging could be more effective.

Fig. F4 presents a contour map of the visual extinction derived for the entire field of Cas A observed with *Herschel*, where the results of the multicomponent SED fitting along the line of sight of Cas A (see Section 3.2) have been combined with the SED modelling of the ISM emission in the field of Cas A (see Appendix 3.2). The regions without any A_V contours correspond to regions with insufficient signal-to-noise detections in the *Herschel* images, which prevented us from modelling the ISM dust emission spectrum. Across the mapped area of $0°.5$, we identify regions with visual extinctions ranging from $A_V = 2$ to 20 mag (the lower values are limited by the sensitivity of our *Herschel* observations). The latter A_V variations correspond to column density variations up to a factor of 18, showing that the amount of material that is positioned along different lines of sight can vary significantly on scales of a few pc. We observe a peak in A_V across the Perseus arm which is positioned just south-east of Cas A.

This paper has been typeset from a TEX/LATEX file prepared by the author.